

FUNDAMENTAL STUDY ON THE REMOVAL OF
CALCIUM ALUMINATE INCLUSIONS BY
METALLURGICAL SLAGS

FUNDAMENTAL STUDY ON THE REMOVAL OF
CALCIUM ALUMINATE INCLUSIONS BY
METALLURGICAL SLAGS

By

GUANG WANG, B. ENG., M. SC.

A Thesis Submitted to Graduate Studies in Partial
Fulfilment of the Requirements for the Degree Doctor of
Philosophy

McMaster University

© Copyright by Guang Wang, April 2025

Abstract

Solid calcium aluminate non-metallic inclusions ($\text{CaO}\cdot 2\text{Al}_2\text{O}_3$ (CA2) and $\text{CaO}\cdot 6\text{Al}_2\text{O}_3$ (CA6)) usually form due to inadequate calcium additions during calcium treatment, and/or interactions among refractories, slag and steel. These inclusions negatively affect steel cleanliness and production efficiency by causing submerged entry nozzle clogging. Most non-metallic inclusions (NMIs) are removed through flotation to the steel – slag interface and dissolved into the molten slag. Therefore, it is critical to better understand the dissolution behaviors of CA2 and CA6 inclusions in metallurgic slags. This study focuses the dissolution kinetics and mechanisms of CA2 and CA6 particles in metallurgical slags using high-temperature confocal laser scanning microscopy (HT-CLSM). The role of intermediate solid products in the dissolution process is also examined via HT-CLSM combined with post-analysis techniques.

Dissolution kinetics of CA2 and CA6 particles in the synthetic $\text{CaO}\text{-Al}_2\text{O}_3\text{-SiO}_2\text{-(MgO)}$ steelmaking slags were examined under varying temperatures, $\text{CaO}/\text{Al}_2\text{O}_3$ (C/A) ratios, and SiO_2 and MgO contents of slag, along with the time dependency of the projection area of the particle during the dissolution process. The results indicate that the dissolution rates of CA2 and CA6 particles increase with higher temperature, increased MgO content of slag, or lower SiO_2 content of slag. At 1550°C , the dissolution rates of CA2 and CA6 particles increased with an increase in slag C/A ratio from 0.9 to 1.8 but declined at 3.8. However, at 1600°C , a higher C/A ratio led to an increased dissolution rate of CA2 particles. Additionally, the particles' motion, dissociation, and interaction with gas bubbles were observed during the experiments, with the first two accelerating dissolution while gas bubbles hindered it.

The impact of porosity (φ) and velocity (v) on the dissolution process of CA2 particles in $\text{CaO}\text{-SiO}_2\text{-Al}_2\text{O}_3$ steelmaking slag was in-situ investigated at 1550°C . Increasing the porosity from 0.08 to 0.20 raised the average dissolution rate (total dissolution time/initial radius of the particle) from 0.35 to 0.59 $\mu\text{m/s}$. Moreover, particle motion was also observed, highlighting its importance in modeling. A novel mathematical model, incorporating both the motion and porosity of particles, was developed and validated against the current experimental and literature data. The model predictions demonstrated that the total dissolution kinetics of CA2 particles was enhanced by an increase in φ , v and driving force (ΔC), and a decrease in slag viscosity (μ). The parameter

sensitivity analysis found that the order of parameter influence is for $0.25 \leq X_i/X_{r(i)} \leq 2$, $\Delta C > \varphi > \nu > \mu$, and for $2 < X_i/X_{r(i)} \leq 4$, $\varphi > \Delta C > \mu > \nu$.

Interrupted dissolution experiments were carried out at 1550°C for CA2 particles in slags with C/A of 1.8 and 3.8, and CA6 particles in slag with C/A of 3.8 and slag with 8 wt.% MgO, respectively. Post analysis using scanning electron microscopy equipped with energy dispersive X-ray spectroscopy (SEM-EDS) combined with thermodynamic calculations revealed their dissolution paths and the impacts of the intermediate solid products on their dissolution kinetics and mechanisms. It was found that intermediate solid layer formed around the undissolved CA2 and CA6 particles in slag with a C/A ratio at 3.8 was melilite, reducing their dissolution rates. Conversely, the formation of randomly dispersed fine solid particles around and within the undissolved CA6 particle in slag with 8 wt.% MgO did not impede their dissolution. No intermediate solid products were observed for the CA2 particle in slag with a C/A ratio of 1.8, consistent with the thermodynamic predictions.

Based on experimental findings and thermodynamic predictions, the dissolution behaviors of the CA2 and CA6 particles in molten steelmaking slags are categorized into two types: (1) direct dissolution: without formation of intermediate solid products or formation of randomly dispersed intermediate solid products, but they do not affect ΔC and do not retard the dissolution kinetics. (2) indirect dissolution: an intermediate solid layer forms around the particle, inhibiting the transport of species and reducing ΔC .

The current work provides a comprehensive understanding of the removal of solid calcium aluminate inclusions, including the dissolution kinetics and mechanisms of CA2 and CA6 particles, by CaO-Al₂O₃-SiO₂-(MgO) metallurgical slags at steelmaking temperature. The findings offer valuable insights for optimizing slag composition in clean steel production, particularly during calcium treatment in secondary steelmaking.

Acknowledgements

First and foremost, I would like to express my sincere gratitude to my supervisors Dr. Dogan and Dr. Phillion for giving me the opportunity to conduct my Ph.D. studies under their guidance. Their invaluable support, constructive discussions, continuous encouragement, and insightful feedback have been pivotal to my academic growth and the timely completion of this work. Also, I extend my sincere thanks to Dr. Leili Tafaghodi, a member of my supervisory committee, whose useful suggestions and encouragement have kept me on the right track. I also wish to acknowledge Dr. Wangzhong Mu for helpful discussion and valuable insights.

I am grateful to the staff members of the Materials Science and Engineering Department. I would like to thank Xiaogang Li, Doug Cully, and Ed McCaffery for their help and for providing the training on various lab equipment involved in this work, which made sample preparation and analysis smooth and efficient. I also want to thank Alisha Digba and Samantha Kandilas for their administrative support and handling paperwork. I am also grateful to the Natural Science Engineering Research Council and McMaster University for their final support, which made this research possible.

My heartfelt gratitude goes to Dr. Qiang Chen, who generously allowed me to use their lab equipment and assisted me in preparing and analyzing samples despite his busy schedule.

I was very fortunate to work alongside amazing people in the McMaster Process Metallurgy group and SIM3P group throughout my Ph.D. journey. I deeply appreciate the help of Dr. Muhammad Nabeel, who supported me from the first day to the last day of this program. His training on HT-CLSM, guidance sample preparation, experimental design and results discussions, and assistance in journal writing were indispensable to my research. I am extremely thankful to Dr. Kezhuan Gu, Dr. Keyan Miao, Dr. Hao He, and Kai Kang for their help and support in research and daily life whenever I needed it.

My Ph.D. journey would have been incomplete in those four years without the beautiful friendships I formed; I am grateful to Richard, Jolin, Michelle, Big Tao, Peter, Tao, and Ruby for their companionship. Special thanks to my friends Sunnio Zeng, Changwei Li, Chengfeng Sun, Jiaxin Zhao, Shiyuan Liu, Shuang Luo, Tiantian Wang, Xiaoyu Wang, Wenjing Deng, and Zepeng Lv, whose moral support and friendship helped me overcome the mental fatigue of my Ph.D. life.

It would be unfair not to acknowledge the contribution of two professors in my life, Prof. Hao Liu and Prof. Jiang. Diao, whose teachings and life wisdom on various topics during my undergraduate and Master's studies deeply influenced me. Their generous support and encouragement were instrumental in my pursuit of a Ph.D. abroad.

Last but not least, I want to express my deepest gratitude to my family—my parents Fuping Wang and Junjun Qiu, and my brother Qiu Wang for their endless support and love, and understanding that have sustained me throughout my life.

Table of Contents

ABSTRACT	III
ACKNOWLEDGEMENTS	V
TABLE OF CONTENTS.....	VII
LIST OF FIGURES	X
LIST OF TABLES	XIII
LIST OF ABBREVIATIONS AND SYMBOLS	XIV
CHAPTER 1.....	1
INTRODUCTION	1
1.1 RESEARCH BACKGROUND.....	1
1.2 OBJECTIVES OF THIS STUDY.....	4
1.3 OUTLINE OF THESIS	4
1.4 REFERENCES.....	6
CHAPTER 2.....	8
LITERATURE REVIEW	8
2.1 SECONDARY STEELMAKING.....	8
2.2 NON-METALLIC INCLUSION CLASSIFICATION, FORMATION AND IMPACT	10
2.2.1 <i>Formation of Non-metallic Inclusions</i>	10
2.2.2 <i>Classification of Non-metallic Inclusions</i>	12
2.2.3 <i>Impacts of Non-metallic Inclusions</i>	12
2.3 NON-METALLIC INCLUSION MODIFICATION	14
2.3.1 <i>Calcium Treatment</i>	14
2.3.2 <i>Rare Earth Element Treatment</i>	15
2.3.3 <i>Top Slag Refining</i>	16
2.4 NON-METALLIC INCLUSION REMOVAL.....	17
2.4.1 <i>Flotation of Non-Metallic Inclusions</i>	18
2.4.2 <i>Separation of Non-Metallic Inclusions</i>	20
2.4.3 <i>Dissolution of Non-Metallic Inclusion</i>	27
2.5 THEORIES, STRUCTURE, AND PROPERTIES OF SLAG.....	43
2.5.1 <i>Theories of Slag</i>	43
2.5.2 <i>Slag Structure</i>	44
2.5.3 <i>Slag Properties</i>	44
2.6 SUMMARY	45
2.7 REFERENCES.....	46
CHAPTER 3.....	55
3.1 INTRODUCTION.....	57
3.2 METHODOLOGY	59
3.2.1 <i>Materials</i>	59
3.2.1.1 <i>CA2 particle preparation</i>	59
3.2.1.2 <i>Slag preparation</i>	60

3.2.2 <i>In-situ observation experiments</i>	61
3.3 RESULTS AND DISCUSSION	63
3.3.1 <i>In-situ observations experiments</i>	63
3.3.2 <i>Effect of temperature on dissolution time of CA2 particle</i>	66
3.3.3 <i>Effect of slag viscosity on dissolution time of CA2 particle</i>	68
3.3.4 <i>Effect of C/A ratio on dissolution time of CA2 particles</i>	70
3.3.5 <i>Determination of dissolution path</i>	72
3.3.6 <i>Comparison with literature data and practical consideration</i>	75
3.4 CONCLUSIONS	77
ACKNOWLEDGMENTS	77
STATEMENTS AND DECLARATIONS	77
REFERENCE	78
CHAPTER 4	80
4.1 INTRODUCTION	82
4.2 METHODOLOGY	89
4.2.1 <i>Experiments</i>	89
4.2.2 <i>Model development</i>	91
4.3 RESULTS AND DISCUSSION	94
4.3.1 <i>Characterization of calcium aluminates</i>	94
4.3.2 <i>Effect of CA2 particle behaviors on the dissolution kinetics</i>	96
4.3.3 <i>Effect of CA2 particle porosity on the dissolution kinetics</i>	99
4.4 VALIDATION AND APPLICATION OF MMDM	100
4.4.1 <i>MMDM validation</i>	100
4.4.2 <i>MMDM application</i>	102
4.5 CONCLUSIONS	106
NOMENCLATURES	107
ACKNOWLEDGMENTS	108
STATEMENTS AND DECLARATIONS	108
REFERENCE	108
CHAPTER 5	112
5.1. INTRODUCTION	114
5.2. METHODOLOGY	116
5.2.1 <i>Material</i>	116
5.2.2 <i>Experimental Procedure</i>	118
5.3. RESULTS AND DISCUSSIONS	120
5.3.1 <i>Thermodynamics analysis</i>	120
5.3.2 <i>Dissolution kinetics parametric study</i>	123
5.3.3 <i>Determination of dissolution path</i>	127
5.3.4 <i>Dissolution mechanisms of particles in molten slags</i>	136
5.4. CONCLUSIONS	139
ACKNOWLEDGMENTS	139
STATEMENTS AND DECLARATIONS	140
REFERENCE	140
CHAPTER 6	143
CONCLUDING REMARKS	143
6.1 KEY FINDINGS AND CONTRIBUTIONS	143

<i>6.1.1 General Overview</i>	143
<i>6.1.2 Specific Findings</i>	145
6.2 FUTURE WORKS	147

List of Figures

Figure 2.1 The overview of the modern steelmaking process [5].....	8
Figure 2.2 Schematic of a argon-stirred ladle furnace equipped with lid and electrodes [10]	10
Figure 2.3 Schematic of the NMI removal process	18
Figure 2.4 Schematic diagram of subprocesses of NMI flotation by gas bubbles [113]	19
Figure 2.5 Schematic representation of a) NMI separation through the steel – slag interface with the formation of steel liquid film and b) NMI separation through the steel – slag interface without the formation of steel liquid film [115].....	21
Figure 2.6 A schematic illustration of the inclusion separation behaviors a) pass the steel – slag interface, b) oscillate at the steel – slag interface, and c) remain at the steel – slag interface.....	22
Figure 2.7 Schematic of forces acting on inclusions [123].....	23
Figure 2.8 The schematic of the experimental setup to study the particle separation from water to oil using the water modeling technique [125].....	25
Figure 2.9 The schematic for the crucible test [149]	28
Figure 2.10 The schematic apparatus of the dip test [150]	29
Figure 2.11 (a) The schematical illustration for the single hot thermocouple technique, and (b) a real-time image during the dissolution process [167].....	30
Figure 2.12 The schematical illustration of HT-CLSM [169].....	31
Figure 2.13 (a) the image of the HT-CLSM setup, and (b) the schematical illustration of the sample setup.....	32
Figure 2.14 Schematic illustration of particle dissolution based on the shrinking core model under mechanisms of (a) Chemical reaction-controlled dissolution (CR), (b) Boundary layer diffusion-controlled dissolution (BLD), and (c) shell layer diffusion-controlled dissolution (SLD)	34
Figure 2.15 Schematic illustration of the particle dissolution using the diffusion distance-controlled dissolution model [176]	35
Figure 2.16 Potential particle behavior during dissolution: (a) motion, (b) rotation, and (c) dissociation	40
Figure 3.1 XRD patterns of CA2 prepared by sintering at 1600°C for 24 h	60
Figure 3.2 Sample holder assembly used in high temperature furnace	62
Figure 3.3 Thermal cycle for dissolution and interrupted experiments	63
Figure 3.4 A sequence of images showing dissolution process of CA2. (a) In slag C/A_1 at 1500, 1550 and 1600°C; (b) in slag with different viscosities at 1550°C; (c) in slag with different C/A ratios at 1600°C. s—Dissolution time of particle; μm —equivalent radius of particle	65
Figure 3.5 Dissociation of a particle during dissolution in slag C/A_1 at 1550°C. (a) 846 s; (b) 876 s; (c) 897 s; (d) 917 s	66

Figure 3.6 Evolution in normalized area of a CA2 particle with time in slag C/A_1 as a function of temperature. Star symbol—Moment when particle dissociation happened, and data after that point is not collected	68
Figure 3.7 Evolution in normalized area of a CA2 particle with time at 1550 °C in slags with different SiO ₂ contents and different viscosities	70
Figure 3.8 Evolution of normalized area of a CA2 particle with time as a function of slag C/A ratio at 1600 (a) and 1550°C (b). Star symbol—Moment when particle dissociation happened, and data after that point is not collected	71
Figure 3.9 Prediction of phase stability of CA2 particle-slag system with FactSage 8.0 [34] at 1550°C	72
Figure 3.10 SEM back scattered electron image and EDS line scan analysis of CA2 particle - CA_2 slag interface after 90 s dissolution at 1550°C	74
Figure 3.11 SEM back scattered electron image and EDS line scan analysis of CA2 particle, CA_4 slag interface after 70 s dissolution	75
Figure 3.12 Dissolution paths of CA2 in slag C/A_2 and slag C/A_4 at 1550°C. Circle—EDS line scan results; triangle dash line—thermodynamic calculation results	75
Figure 3.13 Average area reduction rate of different types of particles as a function of $(\Delta CA/2O_3)/\mu$	77
Figure 4.1. Potential NMI behavior during dissolution: (a) motion, (b) rotation, and (c) dissociation	85
Figure 4.2 X-ray Computed Tomography images of one d-CA2 particle prepared by arc melting (a) presents the original CA2 particles, and (b) present corresponding cropped spheres (radius 150 μm). Color maps indicate equivalent spherical diameters (a) and pore volumes (b).....	91
Figure 4.3 XRD patterns of d-CA2 (blue line), p-CA2 (red line), and standard CA2 (black line)	95
Figure 4.4 XCT-determined specific surface area $f(\varphi)$ as a function of porosity, φ , along with a best-fit exponential curve through the data points.....	96
Figure 4.5 Evolution of normalized radius changes of CA2 particles as a function of time in slag at 1550°C, illustrating different CA2 particle behaviors observed during the dissolution process: (a-e) motion and dissociation in the slag of d1-CA2, (f-h) motion and transparency transition of p2-CA2, and (i-k) motion and interaction with a gas bubble of p-CA2.	99
Figure 4.6 Normalized dissolution curves for spherical Al ₂ O ₃ particle[15] in molten slag at 1550°C compared with different dissolution rate-controlling models.....	101
Figure 4.7 (a) variation of k_m as a function of t/τ for BLD and MMDM. (b) Variation of D/k_m as a function of t/τ for BLD and MMDM.	102
Figure 4.8 (a) Comparison of normalized dissolution curves for p1-CA2 particles and four models, (b) Comparison of CA2 particle's radius change as a function of time between experiments and MMDM prediction in slag at 1550°C.....	104
Figure 4.9 Prediction of the total dissolution time of CA2 particles in CaO-Al ₂ O ₃ -SiO ₂ slag at 1550°C a) variation of v and φ , b) variation of μ and ΔC . (the color bar is nonuniform)	105

Figure 4.10 Effects of parameters variation (v , ΔC , ϕ and μ) on the total dissolution time in percentage	106
Figure 5.1 XRD patterns of the CA6 pellets sintered at 1600°C under argon atmosphere for 24 h	116
Figure 5.2 Schematic illustration of a) sample setup and b) the heating profiles used in dissolution and interrupted experiments	119
Figure 5.3 Prediction of phase stability of the CA2 and CA6 particles – CaO-Al ₂ O ₃ -SiO ₂ based slag systems at 1550°C, (a) slag without MgO, (b) slag with 4wt.%MgO, and (c) slag with 8 wt% MgO. Dash and solid arrows represent the dissolution path of CA6 and CA2 particles, respectively. (C: CaO, A: Al ₂ O ₃ , S: SiO ₂ , M: MgO).....	122
Figure 5.4 Normalized area changes of CA6 particles as a function dissolution time at 1550°C in slags with different viscosities	124
Figure 5.5 Normalized area changes of CA6 particles as a function of time at 1550°C in slags with different C/A ratios	125
Figure 5.6 The normalized area changes of CA2 particles as a function dissolution time at 1550°C in slags S4-S6 with different MgO contents but same C/A ratio, slags S4 and S8 with different MgO contents but similar $\Delta C_{Al_2O_3}$	126
Figure 5.7 The normalized area changes of CA6 particles as a function dissolution time at 1550°C in slags with different MgO contents.....	126
Figure 5.8 Images showing the formation of distinct phases during CA6 particle dissolution in slag S3 at 1550°C after 600 s. (a) in-situ image, and (b-c) SEM back scattered electron images	129
Figure 5.9 SEM backscattered electron image and EDS line scan analysis of CA6 particle – S3 slag interface after (a) 60 s and (b) 600 s dissolution, respectively, at 1550°C. Mixture 1 contains CA6 + CA2 + melilite + slag S3.....	133
Figure 5.10 SEM back scattered electron image and EDS line scan analysis of CA6 particle – slag S6 interface after 10 s dissolution at 1550°C. Mixture 2 contains CA6 + CA2 + MA + slag S6	134
Figure 5.11 SEM back scattered electron image and EDS line scan analysis of CA6 particle – slag S6 interface after 10 s dissolution at 1550°C. Mixture 2 contains CA6 + CA2 + MA + slag S6	135

List of Tables

Table 3.1 Slag composition and experimental temperatures.....	61
Table 3.2 Elemental composition of CA2 particle, slag C/A_2, slag CA_4 and melilite at 1550°C (wt.%)......	74
Table 4.1 Summary of literature on the dissolution of NMIs in various slag systems using HT-CLSM.....	86
Table 4.2 Summary of physical parameters of cropped CA2 particles.....	95
Table 4.3 Summary of CA2 particle dissolution time and rate at 1550°C.....	100
Table 4.4 Parameters used in the models	101
Table 5.1 List of slag composition used in the experiments	118
Table 5.2 A list of potential chemical reactions for the formation of intermediate solid products during CA2 and CA6 particles' dissolution process in molten slags. These reactions are calculated using Reaction module of FactSage 8.0 with FToxid database [22]	128
Table 5.3 Elemental composition of CA6 particle, slags, and relevant intermediate solid products	131
Table 5.4 SEM-EDS point scan results along CA6 – slag S3 interface in Fig. 5.8(c)	130
Table 5.5 SEM-EDS point scan results along CA6 particle – slag S6 interface in Fig. 5.10(c) .	136

List of Abbreviations and Symbols

NMI	Non-metallic inclusion
SEN	Submerged entry nozzle
HT-CLSM	High-temperature confocal scanning microscopy
BOF	Basic oxygen furnace
EAF	Electric arc furnace
LF	Ladle furnace
DH	Dortmund Hoerder-Hüttenunion
RH	Ruhrstahl Heraeus
VOD	Vacuum oxygen decarburization
AOD	Argon oxygen decarburization
VD	Vacuum degassing
VAD	Vacuum arc degassing
RE	Rare earth element
CFD	Computational fluid dynamics
TPC	Three-phase contact
SCM	Shrinking core model
CR	Chemical reaction-controlled dissolution
BLD	Boundary layer diffusion-controlled dissolution
SLD	Shell layer diffusion-controlled dissolution
DS	Diffusion in the stagnant fluid model
DDD	Diffusion Distance-controlled dissolution
A	Al_2O_3
C	CaO
S	SiO_2
M	MgO
[O]	Dissolved oxygen in the liquid steel (ppm)
[Me]	Metal element in liquid steel (%)
T.O	Total oxygen in the liquid steel (ppm)
d_p	Diameter of particle (μm)
d_b	Diameter of bubble (mm)
Re	Reynolds number
CE	Capture efficiency (%)
d_{NMI}	Diameter of non-metallic inclusion (μm)
k_g	Rate constant of NMI removal by bubble flotation
v_b	Bubble rising velocity (m/s)

C_b	Bubble number density (n/m^3)
F_r	Rebound force (N)
F_b	Buoyancy force (N)
F_d	Drag force (N)
F_f	Fluid added mass force (N)
θ_{IMS}	Three phases NMI, steel, and slag contact angle ($^\circ$)
r	Radius of NMI (μm)
U	Steel flow-out velocity (m/s)
Z	NMI displacement (m)
S	Thickness of steel film (mm)
S_c	Rupture thickness of steel film (mm)
ρ_i	Density of NMI (kg/m^3)
μ	Viscosity of NMI (Pa·s)
σ_i	Surface tension (N/m) for inclusion, slag, and steel
σ_{m-n}	Interfacial tension (N/m) between steel and slag, slag and NMI, and steel and NMI
t	time (s)
d_k	Equivalent spherical diameter of the NMI (μm)
g	Gravitational acceleration (m/s^2)
r_0	Initial radius of NMI (μm)
ΔC	Concentration difference of the dissolved species between the bulk slag and saturation content (kg/m^3)
ρ_s	Density of slag (kg/m^3)
D	Diffusion coefficient of the dissolving species in the molten slag (m^2/s)
τ	Total dissolution time of the particle (s)
φ	Diffusion distance parameter
a	Dimensionless saturation
C_{sat}	Component content at saturation (wt.%)
C_0	Component content in the slag (wt.%)
C_p	Component content in the particle (wt.%)
f	Fitting parameter
J	Molar flux of the particle per unit area (mol/m^2)
k_0	Reaction constant
D_0	Diffusion constant
E_{ai}	Activation energies (kJ/mol)
DR	Dissolution rate ($\mu m^3/s$)
NBO	Number of non-bridge oxygen atoms
X_T	Number of tetragonally-coordinated atoms

X_i	Molar ratio of component
Q	Polymerization degree of the molten slag
HT-CLSM	High-temperature confocal laser scanning microscopy

Chapter 1

Introduction

1.1 Research Background

Steel cleanliness is a critical determinant of the properties and performance of steel products, and strongly depends on the size, number, shape, and composition of non-metallic inclusions (NMIs). [1] In the production of Al-killed low carbon steel subjected to calcium treatment, undesired Al_2O_3 , $\text{CaO}\cdot 2\text{Al}_2\text{O}_3$ (CA2) and $\text{CaO}\cdot 6\text{Al}_2\text{O}_3$ (CA6) NMIs could form, and their presence pose significant engineering challenges, notably the clogging of the submerged entry nozzle (SEN) during continuous casting. This issue, particularly severe with solid NMIs, adversely affects production efficiency and product quality. [2] Therefore, minimizing the presence of NMIs in the steel matrix is crucial to achieve high steel cleanliness.

Some approaches have been developed and applied in industries to control and remove NMIs during secondary steelmaking, either by removing the NMIs from liquid steel to the top molten slag or/and modifying their compositions and morphologies to less harmful even beneficial forms in the steel matrix. A well-known NMI modification example is the calcium treatment for aluminum-killed steel, which modifies the solid alumina NMIs to liquid calcium aluminates, and irregular shape to a spherical shape. These modifications significantly reduce the risk of SEN clogging and product defects. [3-5] However, inadequate calcium addition can result in incomplete alteration of alumina NMIs, creating undesired solid NMIs like CA2 and CA6. Once these compounds form, there is an enhanced risk of blockages within the SEN during continuous casting. An alternative approach to removing NMIs from liquid steel involves three steps: 1) flotation of NMIs to the molten steel – slag interface, 2) separation of NMIs through the interface, and 3) dissolution of NMIs in the molten slag. This process can take place in the ladle, tundish, or continuous caster. In the final step, rapid dissolution of NMIs is crucial. If dissolution kinetics are insufficient, NMIs may agglomerate, [6, 7] and oscillate [8, 9] at the interface, increasing the risk of re-entrainment into the molten steel.

Over the past few decades, different approaches have been applied to investigate the dissolution behaviors of NMIs in steelmaking slags. [10-12] The most common approach has been the so-called rotating finger test or named rotating cylinder test. While this method has offered much

insight into NMI dissolution, a significant limitation is the substantial difference in size between the immersed oxide cylinder used in the experiment and NMIs that occur during the industrial process. Potentially, the difference raises doubts regarding the applicability of data obtained from centimeter-sized samples to dissolution kinetics at micro-scale dimensions.

High-temperature confocal laser scanning microscopy (HT-CLSM) is a robust metallurgical testing instrument that has been developed over the past two decades and provides an in-situ real-time observation capability for investigating the behavior of micro-size NMIs under conditions relevant to the steelmaking process. Over this time, NMI dissolution studies using HT-CLSM have been primarily directed toward the elucidation of the dissolution mechanisms and kinetics of single-phase NMIs, employing models such as the shrinking core model and diffusion in the stagnant fluid model. These efforts have included Al_2O_3 [13-15], MgO [16, 17], and SiO_2 [18, 19], as well as the complex NMIs, $\text{MgO}\cdot\text{Al}_2\text{O}_3$ [16, 20] and $\text{TiO}_2\cdot\text{Al}_2\text{O}_3$ [21, 22] in the steelmaking slag systems, e.g., $\text{CaO}\text{-Al}_2\text{O}_3\text{-SiO}_2$ with or without MgO at high temperatures as further explored in the literature review.

However, the dissolution kinetics and mechanisms of solid calcium aluminate NMIs, e.g., CA2 [5, 23] and CA6, remain insufficiently explored, particularly regarding the reaction mechanisms at the NMI – slag interface, despite they negatively affect steel cleanliness and production efficiency by causing submerged entry nozzle clogging. Miao et al. [5] found that higher temperature and lower SiO_2 content in the slag increased the dissolution rate of CA2 particles. Guo et al. [23] observed that an increase in MgO content in slag decreased the dissolution time of CA2 particles. Apart from those findings to the best of the current authors' knowledge, no studies have reported the dissolution kinetics and mechanisms of CA6 particles in $\text{CaO}\text{-Al}_2\text{O}_3\text{-SiO}_2\text{-(MgO)}$ slag system in the open literature. The lack of study into solid calcium aluminate NMIs has occurred for two reasons.

First, previous studies have often selected slag systems designed to avoid the formation of intermediate solid product layers during the dissolution process. [5, 23] Notably, Park et al. [24] found that the formation of solid products, such as CA2 and CA6 during the dissolution of Al_2O_3 in the $\text{CaO}\text{-Al}_2\text{O}_3\text{-SiO}_2$ type slags did not retard its dissolution rate. In contrast, forming a ring-like layer of $\text{MgO}\cdot\text{Al}_2\text{O}_3$ and $2\text{CaO}\cdot\text{SiO}_2$ around a MgO particle slowed the dissolution rate in $\text{CaO}\text{-Al}_2\text{O}_3\text{-SiO}_2$ type slags at 1550°C . Similarly, Guo et al. [25] reported the formation of additional layer ($2\text{CaO}\cdot\text{SiO}_2$) decelerated the dissolution rate of the CaO particle in $\text{CaO}\text{-Al}_2\text{O}_3\text{-}$

SiO₂-(MgO) type slags. These findings highlight the role of intermediate solid product types and morphologies in affecting NMI dissolution kinetics.

Second, the shrinking core model and diffusion in the stagnant fluid model have been applied to determine the limiting step during CA₂ particles' dissolution. They assume that the fluid flow of the molten slag is a Stokes flow, neglect the effect of convection on the dissolution kinetics, and simplify the dissolution to a static dissolution. [5, 23] However, the motion of CA₂ particles during the dissolution process has been observed in their studies, suggesting the impact of convection should be considered in the model. Additionally, to the best of the author's knowledge, only a few studies in the open literature have reported the influence of inclusion porosity on dissolution kinetics [26], despite its critical role in modifying the contact area between the inclusion and slag. For example, Deng et al. [26] reported that the dissolution rate of a lime rod in FeO-CaO-SiO₂ slags was enhanced by the pores of the lime rod, increasing the contact area between the lime rod – slag. This may account for the difference in the lime dissolution behavior at the initial and later stages.

Therefore, further research is needed to explicitly address the dissolution behavior and mechanisms of complex NMIs, such as CA₂ and CA₆, concerning temperature, slag composition, NMI porosity, and velocity. A deeper understanding of these factors is crucial for optimizing clean steel production during secondary steelmaking. The dissolution characteristics of these NMIs directly influence steel cleanliness, mechanical properties, and overall process efficiency. Failure to effectively manage their dissolution can result in defects, reduced product performance, and increased production costs.

Achieving a comprehensive understanding of NMI dissolution requires a multi-faceted approach, incorporating experimental investigations, thermodynamic modeling, and industrial validation. Such insights will enable the development of tailored slag compositions and process conditions that enhance NMI removal while minimizing steel contamination.

The key outcomes of this thesis are expected to address the following critical needs of steelmakers:

1. How do the physical properties of NMIs (e.g., porosity) and process parameters (e.g., slag composition and temperature), affect their dissolution behavior in steelmaking slags?
2. Can a predictive model be developed that estimates the dissolution time of NMIs by incorporating particle velocity and porosity during the dissolution process?

3. What is the rate-limiting step in NMI dissolution after the formation of intermediate solid layers or reaction products? How do these intermediate layers affect inclusion dissolution kinetics and dissolution mechanisms?

1.2 Objectives of This Study

This research aims to develop a comprehensive understanding of the dissolution kinetics and mechanisms of solid calcium aluminate NMIs, namely CA₂ and CA₆, and examine the influence of both process parameters and intrinsic particle properties on dissolution behaviors. The key objectives of this study are:

1. To identify the effect of temperature and slag composition on the dissolution pathways of CA₂ and CA₆ particles via thermodynamic simulations using FactSage 8.0.
2. To conduct a comprehensive experimental study using HT-CLSM to evaluate the effects of NMI properties, temperature, and slag composition on the dissolution kinetics of CA₂ and CA₆ particles.
3. To develop a predictive model for estimating the dissolution time of NMIs by incorporating factors such as velocity and porosity, and to conduct a sensitivity analysis to evaluate the impact of key parameters governing the dissolution process.
4. To identify the rate-limiting step during the NMI dissolution by examining via metallographic analysis the formation of intermediate solid products at the NMI – slag interface.

1.3 Outline of Thesis

Chapter 1 provides a general introduction to this research, describes the motivation of this study, defines the detailed research objectives, and presents an outline of this thesis.

Chapter 2 reviews the pertinent up-to-date literature related to an overview of secondary steelmaking, NMIs formation and impact, and NMI modification. It gives a critical analysis of NMI removal by molten slag, especially the studies focusing on MNI dissolution using HT-CLSM. It presents a brief description of slag structure and properties.

Chapter 3, titled “In-situ confocal microscopy study on the dissolution kinetics of calcium aluminate inclusions in CaO-Al₂O₃-SiO₂ type steelmaking slags”, presents experimental data on the dissolution kinetics of CA₂ particles under various slag compositions and temperatures. The chapter provides a detailed analysis of the evolution of the CA₂ particle size during the dissolution process. The effect of slag C/A ratio, slag viscosity, and temperature on the dissolution kinetics of CA₂ particles are examined. Further, the dissolution path of CA₂ particles in slag with a high C/A ratio and the effect of the intermediate solid layer in this slag are discussed. This chapter has been published in the *Journal of Iron and Steel Research International* (DOI: 10.1007/s42243-024-01397-x).

Chapter 4, titled “Impact of porosity and velocity on the dissolution behaviors of calcium aluminate inclusion in CaO-Al₂O₃-SiO₂ type metallurgic slags: in-situ observation and model advancements”, presents an experimental investigation of the effect of particle porosity on its dissolution kinetics. Various dissolution behaviors are analyzed and compared to assess their influence on the dissolution rate. From these observations, a new mathematical model is then developed to predict the dissolution time of particles by incorporating their porosity and velocity. A sensitivity analysis is carried out to identify the relative influence of different parameters on the total dissolution time. This chapter has been published in the *Journal of Metallurgical and Materials Transactions B* (DOI: 10.1007/s11663-025-03556-1).

Chapter 5, titled “In-situ study on the dissolution kinetics and mechanisms of calcium aluminate inclusions in CaO-Al₂O₃-SiO₂-MgO type steelmaking slags”, presents a comprehensive summary of laboratory experiments conducted to investigate the dissolution kinetics and mechanisms of CA₂ and CA₆ particles at 1550°C under varying slag compositions. The dissolution pathways of CA₆ particles in different slags are experimentally determined, and the potential reactions occurring at the particle-slag interface are examined in detail. Based on these findings, three dissolution mechanisms are proposed. Further, this chapter explores the correlation between the dissolution mechanism and kinetics, providing deeper insights into the dissolution process. This chapter has been submitted to *Ceramics International*, manuscript number: CERI-D-25-04226.

Chapter 6 brings together the key findings from the previous chapters, demonstrating how each contributes to achieving the research objectives. General conclusions are presented, along with an outline of the potential scope for future work.

1.4 References

1. Z.Y. Deng and M.Y. Zhu: *ISIJ Int.* 2013, vol. 53, pp. 450-58.
2. S. K.Michellic and C. Bernhard: *Steel Res. Int.* 2022, vol. 93.
3. W. Yang, L. Zhang, X. Wang, Y. Ren, X. Liu, and Q. Shan: *ISIJ Int.* 2013, vol. 53, pp. 1401-10.
4. Y. Liu L. Zhang, Y. Zhang, W. Yang, W. Chen: *Metall. Mater. Trans. B* 2018, vol. 49, pp. 1841-59.
5. K. Y. Miao, A. Haas, M. Sharma, W. Z. Mu, and N. Dogan: *Metall. Mater. Trans. B* 2018, vol. 49, pp. 1612-23.
6. J. Wikström, K. Nakajima, H. Shibata, A. Tilliander, and P. Jönsson: *Mater. Sci. Eng.: A* 2008, vol. 495, pp. 316-19.
7. J. Wikström, K. Nakajima, H. Shibata, A. Tilliander, and P. Jönsson: *Ironmaking Steelmaking* 2013, vol. 35, pp. 589-99.
8. C.J. Xuan, E.S. Persson, R. Sevastopolev, and M. Nzotta: *Metall. Mater. Trans. B* 2019, vol. 50, pp. 1957-73.
9. G. Shannon, L. White, and S. Sridhar: *Mater. Sci. Eng.: A* 2008, vol. 495, pp. 310-15.
10. P.T. Jones M. Guo, S. Parada, E. Boydens, J.V. Dyck, B. Blanpain, P. Wollants,: *J. Eur. Ceram. Soc.* 2006, vol. 26, pp. 3831-43.
11. A.G.Martinez M.A. Braulio, A.P.Luz, C. Liebske, V.C. Pandolfelli: *Ceram. Int.* 2011, vol. 37, pp. 1935-45.
12. Y. Kashiwaya, C.E. Cicutti, A.W. Cramb, and K. Ishii: *ISIJ Int.* 1998, vol. 38, pp. 348-56.
13. S. Sridhar and A.W. Cramb: *Metall. Mater. Trans. B* 2000, vol. 31, pp. 406-10.
14. K.W. Yi, C. Tse, J.H. Park, M. Valdez, A.W. Cramb, and S. Sridhar: *Scand. J. Metall.* 2003, vol. 32, pp. 177-84.
15. J. Liu, M. Guo, P.T. Jones, F. Verhaeghe, B. Blanpain, and P. Wollants: *J. Am. Ceram. Soc.* 2007, vol. 90, pp. 3818-24.
16. M. Valdez, K. Prapakorn, A.W. Cramb, and S. Sridhar: *Steel Res. Int.* 2001, vol. 72, pp. 291-97.
17. J. Liu, M. Guo, P.T. Jones, F. Verhaeghe, B. Blanpain, and P. Wollants: *J. Eur. Ceram. Soc.* 2007, vol. 27, pp. 1961-72.
18. S. Feichtinger, S.K. Michellic, Y.B. Kang, and C. Bernhard: *J. Am. Ceram. Soc.* 2014, vol. 97, pp. 316-25.
19. Y. Ren, P. Zhu, C. Ren, N. Liu, and L. Zhang: *Metall.Mater.Trans. B* 2022, vol. 53, pp. 682-92.
20. B.J. Monaghan and L. Chen: *Ironmaking steelmaking* 2006, vol. 33, pp. 323-30.
21. H.A. Dabkowska M. Sharma, N. Dogan *Steel Res. Int.* 2019, vol. 90, p. 1800367.
22. M. Sharma and N. Dogan: *Metall. Mater.Trans. B* 2020, vol. 51, pp. 570-80.
23. B. Guo, J.J. Wang, and L.F. Zhang: *Metall. and Mater. Trans. B* 2024.
24. J.H. Park, I.H. Jung, and H.G. Lee: *ISIJ int.* 2006, vol. 46, pp. 1626-34.
25. X.L. Guo, J.V. Dyck, M.X. Guo, and B. Blanpain: *AIChE J.* 2013, vol. 59, pp. 2907-16.

26. T.F. Deng, J. Gran, and S.C.Du: *Steel Res. Int.* 2010, vol. 81, pp. 347-55.

Chapter 2

Literature Review

2.1 Secondary Steelmaking

Steelmaking has undergone transformative advancements since Henry Bessemer invented the converter process in the 1850s, evolving through diverse operational practices and continuous technological updates. [1, 2] The introduction of continuous casting by Henry Besser and Siegfried Junghans marked a pivotal milestone, driving improvements in process efficiency and enabling enhanced cleanliness and property control. [3, 4] These advancements have positioned modern steelmaking as a highly refined operation capable of producing high-performance steel products tailored for demanding applications.

Modern steelmaking processes can be broadly classified into primary and secondary stages. In primary steelmaking, molten steel is produced either by refining hot metal in a basic oxygen furnace (BOF) or by melting scrap and direct-reduced iron pellets in an electric arc furnace (EAF), as illustrated in **Fig. 2.1**. [5] This stage is primarily focused on reducing impurities and achieving the initial composition of molten steel.

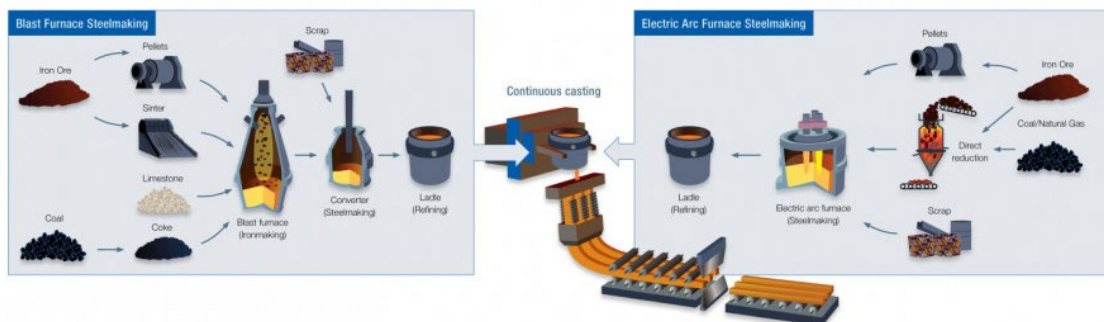


Figure 2.1 The overview of the modern steelmaking process [5] (Reprinted with permission)

Secondary steelmaking encompasses any post-steelmaking process performed at a separate station or reactor prior to casting. It plays a critical role in refining molten steel further to meet the final product specifications. This stage involves processes such as inert gas purging, ladle furnace refining, vacuum degassing, and injection metallurgy at different units. These units collectively achieve objectives such as decarburization, dephosphorization, deoxidation, desulfurization, degassing, alloying, inclusion control, homogenization of steel composition and temperature, and adjustment of teeming temperature. [6, 7] Since no single unit can accomplish all these tasks alone,

specialized vessels have been developed for different refining processes, including the ladle furnace (LF), Dortmund Hoerder-Hüttenunion (DH), Ruhrstahl Heraeus (RH), vacuum oxygen decarburization (VOD), argon oxygen decarburization (AOD), vacuum degassing (VD), and vacuum arc degassing (VAD). [8] The thermodynamics and kinetics aspects of these processes have been extensively detailed by Dutta et al., [7] Holappa et al. [6] and González et al. [9].

The ladle furnace (LF), illustrated in **Fig. 2.2**, [10] is the most commonly used vessel for steel refining due to its multifunctional capabilities, including: [7]

- 1) Removal of dissolved oxygen through the addition of deoxidizers.
- 2) Modification and removal of inclusions.
- 3) Bulk chemical composition control via alloy additions.
- 4) Removal of dissolved gases, such as hydrogen and nitrogen.
- 5) Facilitation of desulfurization.
- 6) Temperature control to maintain process consistency.

Ladle refining typically begins with the addition of deoxidizers and synthetic slag formers. The steel received from primary processes, such as the BOF or EAF, contains 500 – 900 ppm [11, 12] of dissolved oxygen [O], which has negligible solubility in the solid steel. If not removed, the [O] would be rejected by the steel during the continuous casting and solidification processes, leading to issues such as blowholes, alloying inefficiencies, and casting defects. [13] Deoxidation reduces the dissolved oxygen content to acceptable levels, while synthetic slags absorb deoxidation products (non-metallic inclusions, NMIs), preventing reoxidation and minimizing heat loss of steel. [14] Subsequent operations include argon stirring, alloy addition, slag modification, and arc heating. [15] The ladle system involves interactions among six distinct phases: steel, slag, inclusions, gas bubbles, refractory, and ferroalloys. These interactions collectively drive steel refining, ensuring high cleanliness and precise control of its physical and mechanical properties. [16]

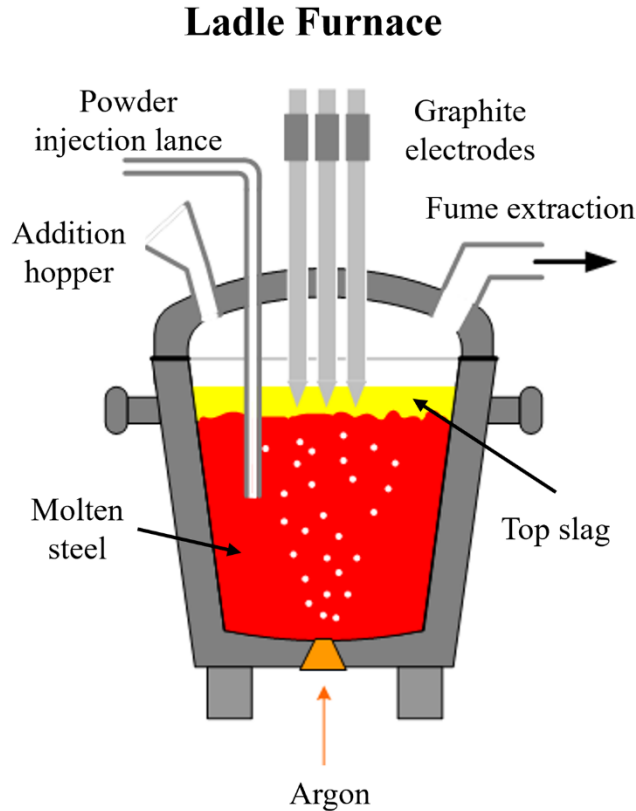


Figure 2.2 Schematic of a argon-stirred ladle furnace equipped with lid and electrodes [10]
(Reprinted with permission)

2.2 Non-metallic Inclusion Classification, Formation and Impact

NMIs are discrete, non-metallic chemical compounds that form within a steel matrix due to chemical reactions, contaminations, and precipitations during refining and solidification processes. [7] Steel cleanliness, a key determinant of steel quality, highly depends on the size, number, shape, and composition of NMIs. [17] This subsection briefly reviews the formation, classification, and impacts of NMIs on the processing and final products.

2.2.1 Formation of Non-metallic Inclusions

The formation of NMIs is a complex process influenced by thermodynamic, kinetic, and operational factors as summarized in previous studies. [6, 7, 18] The primary formation mechanisms include:

1) Deoxidation Reactions

Deoxidation is a key step to remove excess [O] from molten steel during secondary steelmaking. Deoxidizers with a higher affinity for oxygen than iron, like aluminum, silicon, and silicon-manganese, collectively referred to as (Me), are added to the liquid steel to react with the [O] as shown in Reaction 2.1, forming stable NMIs, e.g., Al₂O₃, SiO₂, Mn-SiO₂. [19]



The type of deoxidizer depends on the steel grade and customers' requirements. For example, Si-Mn alloy is commonly used in spring steel and tire cord steel to avoid the formation of high-melting point Al₂O₃-riched NMIs—instead low melting point SiO₂-MnO-rich NMIs form. [20, 21] Once the added deoxidizer starts reacting with the dissolved oxygen, intensive nucleation of small NMIs will occur. After nucleation through deoxidization reactions, NMIs grow via diffusion, coalescence, and collision before rising to the steel-slag interface due to density differences, assisted by gas stirring, then dissolve in the top slag. [17, 22] These NMIs are usually micro-scale in size, with a diameter ranging from a few to fifty micrometers. [23]

2) Precipitation During the Solidification Process

The presence of solute elements within the steel, such as oxygen, sulfur, nitrogen, aluminum, titanium, calcium, and magnesium, segregate during continuous casting (solidification), forming oxides, sulfides, nitrides, and complex NMIs. [24] These NMIs are usually small, with a diameter that is usually less than 10 μm.

3) Reoxidation Reactions

Liquid steel can re-oxidize through contact with atmospheric oxygen [25, 26], slag [27, 28], or refractory phases [29, 30] during secondary refining, as well as during the transfer of liquid steel via the tundish and mold. As a result, a wide range of NMIs form, leading to nozzle clogging issues and product defects. [31-33] Park et al. [34] provided a detailed review regarding the reoxidation phenomena of liquid steel in secondary steelmaking and continuous casting processes. These NMIs are usually less than 50 μm in diameter.

4) Refractory Erosion/Corrosion

Refractory materials used in the ladle undergo erosion and corrosion due to high temperatures, chemical interactions with molten slag and steel, mechanical wear, and thermal shock. [7, 8] All these actions lead to the formation of refractory fragments that act as NMIs in molten steel. [35] The diameter of these NMIs is, generally, larger than 100 μm. [9]

Solid calcium aluminates can be formed after deoxidization, especially when alumina-containing deoxidizers are used and calcium treatment is employed, via interactions among deoxidization products (Al_2O_3 NMIs), slag, steel, and refractories.

2.2.2 Classification of Non-metallic Inclusions

NMIs can be classified into different types. According to their origins, NMIs can be divided into two types: 1) endogenous NMIs, which form within the steel during deoxidation and precipitation processes; and 2) exogenous NMIs, which originate from external sources such as reoxidation, slag entrapment, or refractory erosion/corrosion. Endogenous NMIs are typically small, numerous, and uniformly distributed, while exogenous NMIs are larger, less frequent, and randomly dispersed.

[8] According to chemical composition, NMIs can be categorized as [7]:

- Oxides: Formed from reactions with oxygen (e.g., Al_2O_3 , SiO_2 , CaO , $\text{CaO}\cdot 2\text{Al}_2\text{O}_3$).
- Sulfides: Result from sulfur interactions (e.g., MnS , CaS , $\text{MnS}\cdot\text{MnO}$).
- Nitrides: Formed from reactions with nitrogen (e.g., TiN , AlN , $\text{V}(\text{C}, \text{N})$).
- Phosphides: Result from phosphorus interactions (e.g., Fe_3P , Fe_2P).

Finally, NMIs are sometimes classified as *primary*, meaning that they form before the start of molten steel solidification, and *secondary*, meaning that they were generated during the solidification process. [36]

2.2.3 Impacts of Non-metallic Inclusions

1) Efficiency of production

NMIs play a critical role in the continuous casting of steel, particularly in the context of submerged entry nozzle (SEN) clogging, a phenomenon that significantly impacts production efficiency and steel quality. [37] During the casting process, NMIs can accumulate in the SEN, leading to flow restrictions, uneven steel flow, and even operational shutdowns. [38]

The clogging phenomenon is primarily driven by the adhesion and aggregation of solid NMIs on the refractory surfaces of the nozzle, which is influenced by steel composition, NMI characteristics, and casting conditions. [39] One example is the production of Ti-stabilized ultra-low carbon steels, which are widely used in automotive body parts. In this process, titanium is added to the molten steel as a stabilizer for residual carbon and nitrogen just before casting. [40] However, the addition of titanium caused a decrease in the wettability between steel and NMIs,

promoting NMIs agglomeration and increasing the clogging risk by NMIs containing titanium. [40-42] Another example concerns the behavior of refractory castables, which often contain solid calcium aluminates ($\text{CaO}\cdot 2\text{Al}_2\text{O}_3$ (CA2) and $\text{CaO}\cdot 6\text{Al}_2\text{O}_3$ (CA6)) to enhance thermal shock resistance and extend service life. Salomão et al. [43-45] reported that when molten slag and steel encounter these refractories, erosion and corrosion can occur, generating refractory fragments that may act as exogenous NMIs in the molten steel, and increasing the clogging risk due to CA2 and CA6 NMIs. The mechanisms and influencing factors of clogging, including thermodynamic and interfacial aspects, have been extensively reviewed by Michelic and Christian. [37]

2) Properties of Steel

Fracture Toughness

Fracture toughness, which is the ability of steel to absorb energy and deform plastically before fracturing, is significantly influenced by the presence of NMIs. [46] For example, an appreciable increase in sulfur content (from 10 to 60 ppm) can improve the fracture toughness of high-speed wheel steel by promoting the formation of complexed $\text{MnS}\text{-Al}_2\text{O}_3$ NMIs and effectively reducing the interfacial stress between $\text{MnS}\text{-Al}_2\text{O}_3$ NMIs and steel matrix. [48, 49] Moreover, having a reduced number density of NMIs positively impacts the fracture toughness of steel. [50]

Plasticity

Plasticity, the ability of steel to deform without fracture, is closely related to the type, content, shape, and size of NMIs. [51] Larger NMIs often lead to brittle failure, reducing the ductility of steel. Certain types of NMIs, particularly sulfides, have been shown to correlate with decreased plasticity, especially in high-strength low-ductility alloys. [52] For example, stringer-type NMIs aligned along rolling directions can lead to delamination or splitting in sheet metal applications, reducing structural integrity. [53] However, some nano-scale NMIs might enhance ductility by promoting finer microstructures. [54]

Strength

NMIs impact the strength of steel in a complex manner. [55] Research indicates that smaller NMIs can enhance strength by acting as barriers to dislocation movement, thereby improving the yield strength of the cord steel. [56] In contrast, larger NMIs tend to weaken steel, as they serve as stress risers where cracks can initiate under load. For instance, it was found that alumina NMIs larger than 1 μm in high-silicon steel can significantly decrease yield and tensile strength due to their ability to concentrate stress at their interfaces. [57]

Fatigue

Fatigue, critical for steel subjected to cyclic loading, is significantly influenced by NMIs, as they often serve as initiation sites for cracks. [58] The role of NMIs in fatigue failure is contingent on their type, size, shape, and distribution within the steel matrix. [59] For instance, Al_2O_3 and TiN were often found as the source of fatigue cracks during hot rolling due to their low deformation ratio. [59] Large inclusions can lead to accelerated crack propagation under cyclical loading, while small and well-distributed NMIs can improve fatigue life by refining grain structures. Zhang et al. [60] reported that for clean 54SiCr6 steel in which the size of NMIs is smaller than $1\ \mu\text{m}$, the fatigue cracks were not initiated from NMIs or NMI clusters but from the region enriched with carbon.

2.3 Non-metallic Inclusion Modification

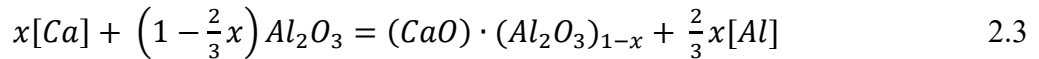
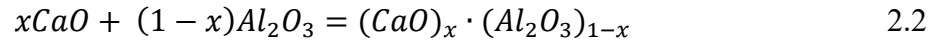
As mentioned in the above sections, most NMIs, especially solid ones, negatively impact production efficiency and final product properties. Effective control of NMIs is, therefore, critical for achieving high efficiency and quality steel production. One widely applied approach is to modify these NMIs to less detrimental forms, even positive ones. Generally, three main techniques are employed in industrial practice.

2.3.1 Calcium Treatment

Calcium treatment primarily aims to modify irregularly shaped solid alumina-based NMIs into full liquid or semi-liquid calcium aluminates with a more spherical morphology. This process involves adding calcium or calcium alloy (e.g., CaSi) to the liquid steel, typically in the form of wire, at the final stage of secondary steelmaking. [61] However, the calcium yield is relatively low (12 – 35 wt.%) due to its low melting point and high reactivity, even with various addition methods developed to improve efficiency. [62]

The dissolved calcium reacts with the pre-existing alumina NMIs in liquid steel, initiating complex reactions and phase transformations. The effectiveness of calcium treatment depends on precise control of the calcium addition. Insufficient or excessive calcium in the liquid steel can lead to the formation of undesired NMIs like CA_2 , CA_6 , and CaS , contributing to SEN clogging issues and deteriorating steel quality. [63, 64] For instance, Faulting et al. reported that $[\text{Ca}]/[\text{Al}]$ ratio (wt.%) exceeding 0.15 promotes the formation of liquid $\text{CaO}\cdot\text{Al}_2\text{O}_3$ NMIs while eliminating

solid CA6 NMIs. As a result, the mass of liquid steel cast before SEN clogging increased fourfold in pilot-scale tests compared to a lower [Ca]/[Al] ratio. [65] Studies have investigated complex reaction pathways and phase transformations involved in calcium treatment to reveal the formation mechanisms of different calcium aluminate phases (e.g., $12\text{CaO}\cdot 7\text{Al}_2\text{O}_3$ (C12A7), $3\text{CaO}\cdot \text{Al}_2\text{O}_3$ (C3A), CA2, CA6). [61, 66-69] The following Reactions (2.2) and (2.3) have been proposed to describe the modification of alumina NMIs. [69, 70] Here, square brackets indicate elements dissolved in liquid steel, while parentheses denote inclusion phases.



The effectiveness of calcium treatment is significantly influenced by factors like calcium feeding rate, holding time, temperature, addition methods, and steel composition. [62] Choudhary et al. [64] suggested that higher temperatures facilitate successful calcium treatment by promoting the formation of liquid calcium aluminates. However, Kor et al. [71] reported that increasing temperature from 1540 to 1590°C, initially enhanced the calcium effectiveness due to the increased solubility of calcium in molten steel, but subsequently decreased it due to the reduced rigidity of calcium alloy wire.

In addition to modifying alumina NMIs, calcium treatment is also widely applied to prevent MnS formation by forming CaS-MnS complexes or CaS NMIs. This approach is particularly beneficial in re-sulfurized steels, where CaS-MnS inclusions are expected to adopt spherical or spindle-like morphologies, [72, 73] This treatment improves the fracture toughness, [74] and mechanical property [75], as well as resistance to hydrogen-induced cracking (HIC) [76] of the steel products. For example, it was reported that the steel with a Ca/S ratio higher than 1.25 effectively prevented HIC in API pipeline steel containing 1 – 16 wt.% [Mn] and 8 – 26 ppm [S]. [76]

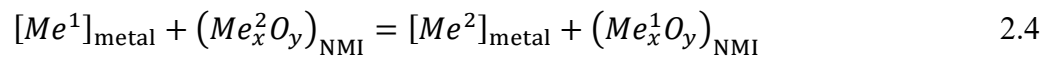
2.3.2 Rare Earth Element Treatment

Rare earth elements (REs), such as cerium (Ce), lanthanum (La), and yttrium (Y), have emerged as effective agents for solid NMIs modification due to their strong affinity for oxygen and sulfur. [77] The addition of REs transforms irregular and large NMIs into fine, RE-based sulfides and oxides with spherical morphology. This modification improves steel properties, such as corrosion resistance, while mitigating the detrimental effects of original NMIs. [78-80]

Shi et al. [81] investigated the Y addition on the corrosion resistance of 304 stainless steel and found that the optical pitting corrosion resistance was achieved at a 190 ppm Y addition, facilitating the formation of fine, spherical Y₂O₃ NMIs. Several studies have also examined the effect of different RE addition sequences on NMI modification, including combinations of multiple REs or REs with non-RE elements. [82-84] For example, when Mg and Ce were added to high-nitrogen stainless-bearing steel, the NMIs evolution pathway depended on the order of addition. If Mg was added first, the transformation followed: Al₂O₃ → MgO + MnS → MgS + Ce-O-S. However, if Ce was added first, the evolution process changed to Al₂O₃ → Ce-O-S + MnS → MgS + Ce-O-S. This suggests that the addition order of Ce and Mg can affect the deoxidation and desulfurization ability. [85] Wang et al. [86] summarized the general evolution of NMI after adding a single type RE element (Ce, La, Y) as follows: NMI → NMI + RE-Al-O → RE-Al-O + RE₂O₂S + RE-S or RE₂O₂S + RE-O. Additionally, REs contribute to the purification of liquid steel [87] and facilitate micro-alloying [52]. However, the cost of steel production would increase with applying REs treatment. [88]

2.3.3 Top Slag Refining

Top slag refining is a widely adopted technique for modifying NMIs to produce specific steel grades, including high-carbon hard wire steel and high-strength alloyed steel. [83, 89] This method regulates the concentrations of strong deoxidizing elements in liquid steel, such as aluminum, calcium, silicon, and magnesium, through interactions at the steel – slag interface. These elements subsequently influence the NMI composition via chemical reactions between the liquid steel, slag, and NMI, as described by Reaction 2.4. [90]



Suito et al. [90] explored NMI composition control in ultra-low carbon steel from the thermodynamic perspective. They found that the concentrations of [Si], [O], [Al] and [Ca] in an ultra-low carbon sheet steel were directly influenced by the top slag composition via the interactions among top slag components (e.g., MnO, SiO₂, Fe_xO and CaO), steel components (e.g., Al, Ca, Si and S) and NMIs (e.g., SiO₂, Al₂O₃, CaS) at slag – steel interface and within the liquid steel. For instance, it was shown that (SiO₂) can be reduced by [Al], and form Al₂O₃ NMI, leading to an increase in [Si] and a decrease in [O]. Additionally, the higher-than-expected [O] content observed in practice was attributed to the effect of Fe_xO in the top slag. Zhang et al. [89] conducted

laboratory steel – slag equilibrium experiments to study the effect of CaO/SiO₂ and CaO/Al₂O₃ ratios of CaO-SiO₂-Al₂O₃-MgO slag system on the MnO-SiO₂ type NMIs. In this work, 430 stainless steel was deoxidized by Si-Mn alloy. They found that increasing the CaO/SiO₂ ratio of slag from 1 to 5 reduced the total oxygen (T.O) and [O] in the steel from 0.0070 to 0.0038 wt.% and 0.0013 to 0.0008 wt.%, respectively. Furthermore, the number density of NMIs decreased from 16.0 to 6.8 per mm². However, increasing the CaO/Al₂O₃ ratio of slag from 0.75 to 2.5, the [O] decreased in steel, while T.O, NMI number density, and equivalent diameter remained largely unchanged. Moreover, the concentration of Al₂O₃ NMI content in the liquid steel can be expressed as linear function of the activity ratio of slag components, suggesting the content of Al₂O₃ (wt. %) in NMIs can be controlled by optimizing the top slag composition.. [89] Chen et al. [91] reported that for the tire cord steel deoxidized by Si-Mn alloy in industrial practice, the composition evolution of NMIs as follows: MnO-Al₂O₃-SiO₂ → CaO-Al₂O₃-SiO₂ → MnO-Al₂O₃-SiO₂, indicating their composition and corresponding shapes were under good control. Furthermore, the plasticization of NMIs can be achieved by maintaining the CaO/SiO₂ ratio of slag around 1.0 and limiting the Al₂O₃ content below 10 wt.%. [91] However, the application of slag refining technique is limited for broader steel production due to the slow reaction kinetics at the steel – slag interface and low efficiency. [7]

2.4 Non-metallic Inclusion Removal

Continuous efforts have been made to enhance the removal of NMIs from liquid steel during secondary steelmaking to improve the quality of steel products and reduce the likelihood of SEN clogging. [92, 93] The removal of inclusions consists of three stages: 1) floatation of inclusions to the molten steel-slag interface (**Fig. 2.3**, position *a* to position *b*), 2) separation of inclusions across the molten steel-slag interface (**Fig. 2.3**, position *b* to position *c*), and 3) dissolution of inclusions in the slag (**Fig. 2.3**, position *c* to position *d*). [92, 94] These stages are summarized in the following sections.

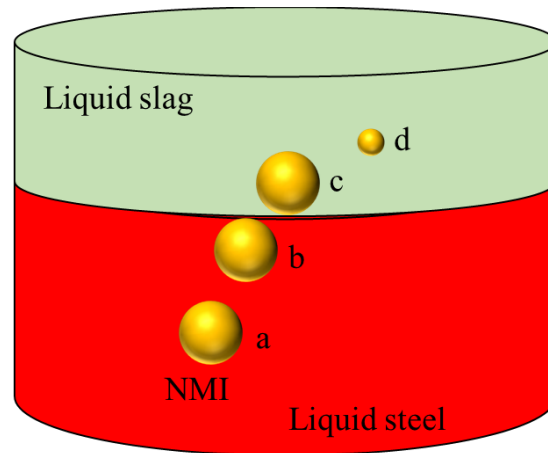


Figure 2.3 Schematic of the NMI removal process

2.4.1 Flotation of Non-Metallic Inclusions

NMIs tend to float out from the molten steel due to their lower densities than that of steel. Moreover, most NMIs (solid) are not wet by liquid steel. [95] The flotation of NMIs from the molten steel was enhanced by attachment to gas bubbles generated from the bottom plugs or tuyeres of the reactor. [40, 95] Various factors, including the velocity of liquid, the properties of NMI, and molten steel, bubble size have investigated the mechanism of NMI – bubble interaction, thin-film generation, and rupture between NMI and bubble, time for collision and film drainage, probabilities for sliding, collision, and adhesion with the help of the mathematical model, water model, and computational fluid dynamics (CFD) model. [92, 95-112]

The following subprocesses can describe the overall process of the NMI flotation by the gas bubbles [105, 113], as illustrated in **Fig. 2.4**. [113]

- i) The approach of NMI to bubbles,
- ii) Formation of a thin liquid film between the NMI and the bubble,
- iii) Oscillation and/or sliding of the inclusion on the bubble surface,
- iv) Drainage and rupture of the film with the formation of a dynamic three-phase contact (TPC),
- v) Stabilization of bubble – NMI aggregates against external stress,
- vi) Flotation of the bubble – NMI aggregates.

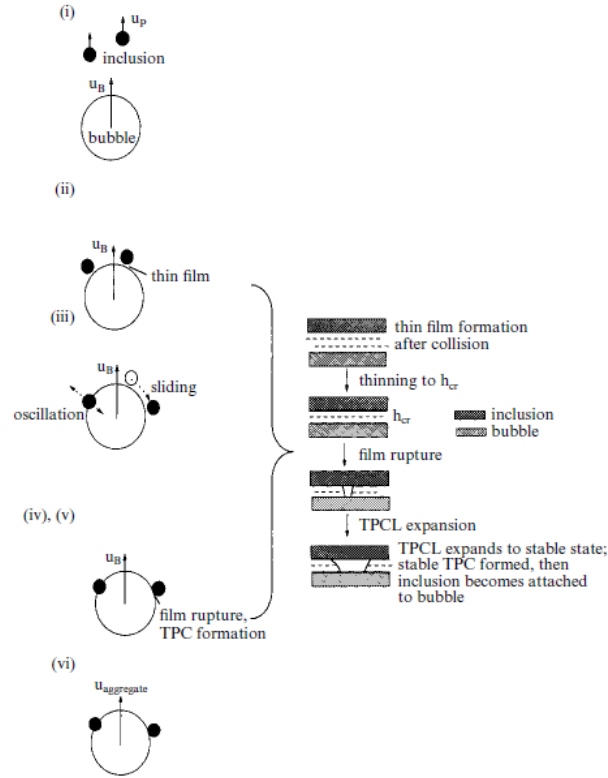


Figure 2.4 Schematic diagram of subprocesses of NMI flotation by gas bubbles [113] (reprinted by permission of Informa UK Limited, trading as Taylor & Francis Group)

Some mathematical models have been developed aiming to suggest the optimum gas bubble size for enhancing the efficiency of NMIs flotation. Wang et al. [105] explored the effect of bubbles and NMIs size on the NMI flotation via a mathematical model. They found that the optimum bubble size for removing small alumina NMIs ($< 50 \mu\text{m}$ in diameter) from molten steel was between 0.5 – 2.0 mm in diameter. Zhang et al. [113] also suggested that the optimum bubble diameter for silica NMI removal by flotation was 1 – 5 mm. Söder et al. [106] claimed that NMIs with a diameter larger than $25 \mu\text{m}$ were mainly removed from the liquid steel to the steel – slag interface by Stokes flotation, whereas smaller NMIs were primarily removed by spherical-cap bubble flotation. Similar results were reported by Wang et al. [107]. They found that NMI removal by Stokes flotation was the main contributor for larger NMIs with a diameter of $50 \mu\text{m}$, and the removal efficiency of tiny bubbles (2 mm) on NMIs was higher than that of larger bubbles (10 mm). [107] However, none of the above-mentioned models have been validated with experimental data.

Xu et al. [99] [100] employed a CFD model to study the influence of bubble size on NMIs flotation, which was validated against the water model experiments by comparing the movement of a single particle due to a single gas bubble. They found that bigger-size NMIs could be more easily removed than smaller ones by bubble flotation due to the buoyancy force and attachment probability. Moreover, the removal percent per bubble was increased from 2.3 to 18.9 by increasing the bubble diameter from 5 to 16 mm. Liu et al. [114] developed a CFD model coupled with phase-field and flow-solid interaction to simulate the flotation of a solid NMI and interaction with the steel – slag interface. The model was validated using a water model experiment by comparing the velocity of a single particle obtained from the two models, and an acceptable agreement was reached. They found that the flow of small NMIs satisfies Stokes flow while the flow of larger NMIs satisfies turbulent flow. [114]

In addition to mathematical and CFD models, the water model has been applied to study the flotation of NMI. Shimasaki et al. [95] found that the capture efficiency of the gas bubble was proportional to the ratio of the NMI and the bubble size (d_p : 3 – 30 μm , d_b : 2.76 – 4.14 mm) at different bubble Reynolds numbers, as shown in equation 2.5. [95] Further, Zhang et al. [98] [112] found that a high gas flow rate ($29.33 \times 10^{-6} \text{ m}^3 \text{ s}^{-1}$), high stirring speed by an impeller (800 rev min^{-1}), small bubble size ($< 3.5 \text{ mm}$), and larger particle size ($> 32.5 \mu\text{m}$) were favorable for particle removal by bubble flotation in their study conditions.

$$CE = \frac{k_g}{v_b * D_b} * \frac{4}{\pi(d_{\text{NMI}} + d_b)^2} \quad 2.5$$

where CE is the capture efficiency, k_g is the rate constant of NMI removal by bubble flotation, v_b is the bubble rising velocity (m/s), D_b is the bubble number density (n/m^3), d_{NMI} and d_b are the diameters of the NMI (μm), and gas bubble (mm), respectively.

The general conclusions reached by mathematical models, CFD models, and water models are 1) tiny gas bubbles are beneficial for removing NMIs during the floatation process, and 2) large NMIs are easier to remove. Unfortunately, none of the above studies explored the floatation behaviors of CA2 and CA6 NMIs.

2.4.2 Separation of Non-Metallic Inclusions

Nakajima and Okamura [115] first proposed a mathematical model to investigate and theoretically analyze the hydrodynamic mechanism of NMI separation from liquid steel to slag through the steel – slag interface based on dynamic force balance and assumptions. In this model,

it was postulated that NMI separation occurred via four steps: 1) a preliminary approach of an NMI to the molten steel – slag interface, 2) a steel film drainage (thinning), 3) a steel film rupture, and 4) a contact with slag as shown in **Fig. 2.5**. [115] They also claimed that the steel film formation depended on the Reynolds number (Re) of NMI. If $Re \geq 1$, steel film would form (**Fig. 2.5 (a)**), otherwise not (**Fig. 2.5 (b)**). The authors proposed four forces, rebound force (F_r), buoyancy force (F_b), drag force (F_d), and fluid-added mass force (F_f), acting on the inclusion during the separation process. The forces balance is shown in equation 2.6.

$$\frac{4}{3} \pi r_i^3 \cdot \rho_i \cdot \frac{d^2 Z}{dt^2} = F_b + F_r + F_d + F_f \quad 2.6$$

where r_i is the radius of NMI (μm), Z is NMI displacement (m), t is the separation time (s).

The forces acting on the inclusion in the two cases are different, and the literature provides more details about how the force is calculated. [115] Their numerical results have been validated by comparing them with Krupman’s high-temperature experimental results using slag and alumina NMIs. [116, 117] Three different behaviors of NMIs during the separation process were found, as illustrated in **Fig. 2.6**: separation (**Fig. 2.6 (a)**), oscillation (**Fig. 2.6(b)**), and remaining at the molten steel-slag interface (**Fig. 2.6(c)**). In their study, the critical conditions for NMI separation through the steel – slag interface are that the slag viscosity is less than 0.1 Pa·s, the diameter of NMIs is greater than 50 μm , or $\cos\theta_{\text{IMS}}$ is larger than zero (θ_{IMS} is the three phases NMI, steel, and slag contact angle). [115]

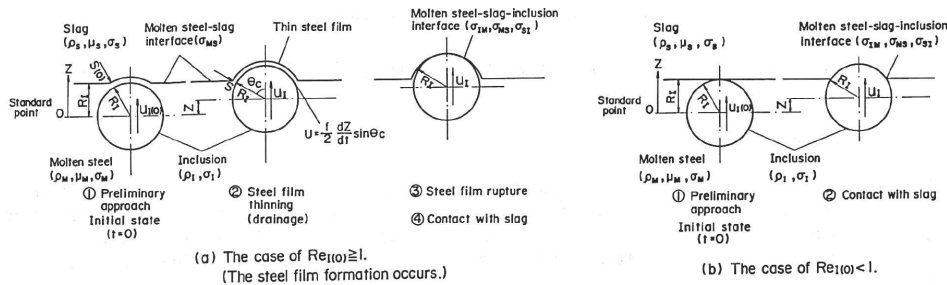


Figure 2.5 Schematic representation of a) NMI separation through the steel – slag interface with the formation of steel liquid film and b) NMI separation through the steel – slag interface without the formation of steel liquid film [115] (Reprinted with permission)

where U is the steel flow-out velocity (m/s), S is the thickness of steel film (mm), S_c is the rupture thickness of steel film (mm), ρ_i , μ_i , and σ_i are density (kg/m^3), viscosity (Pa·s), and surface tension (N/m) for inclusion, slag, and steel, respectively, σ_{m-n} is the interfacial tension (N/m) between steel and slag, slag and NMI, and steel and NMI. t is time (s).

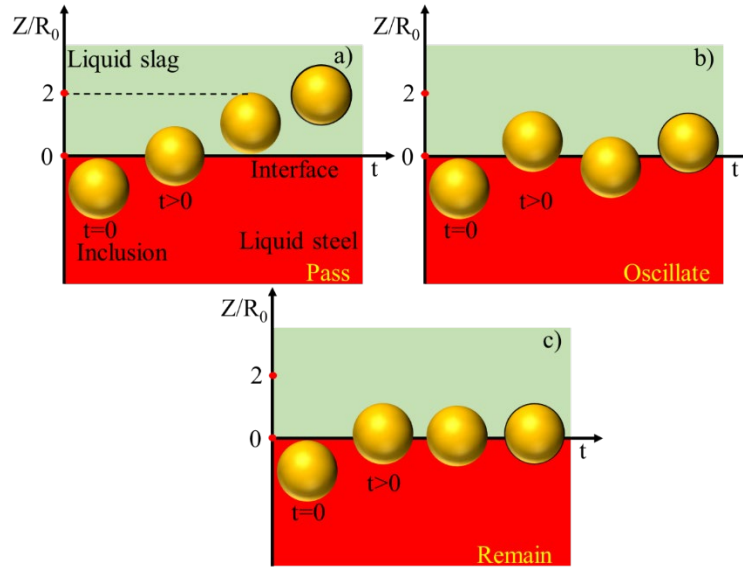


Figure 2.6 A schematic illustration of the inclusion separation behaviors a) pass the steel – slag interface, b) oscillate at the steel – slag interface, and c) remain at the steel – slag interface

Many researchers further modified and extended the mathematical model proposed by Nakajima and Okamura for different purposes. Bouris et al. [118] extended the model by incorporating NMI, slag and steel properties, and NMI velocity at the steel – slag interface. Smaller NMIs (diameter < 50 μm) were found to be trapped in the interface, while the lift forces more easily removed the larger ones (200 μm) due to turbulent shear stress. Valdez et al. [119] applied the model modified by Bouris et al. [118] to study the separation of alumina NMIs with size 2.5 – 200 μm by changing the terminal velocity from 0 to 0.3 m/s. They found that the interfacial energy between slag and NMIs was the most pertinent property that could hinder the interfacial separation of NMIs. The separation process was rapid enough to be ignored unless the slag surface tension was higher than 0.80 N/m for the ladle and mold slags and 0.41 N/m for tundish slag. [119] Strandh et al. [120, 121] studied the separation behavior of liquid NMIs (50CaO-50Al₂O₃, wt.%), and they suggested that the interfacial tension between steel, slag, and liquid NMIs phases and the slag viscosity are most critical for separating liquid inclusion through the liquid steel – slag interface. Shannon et al. [122] extended the model modified by Bouris et al. [118] by incorporating the dissolution and shape (sphere, octahedron, and plate) of NMIs to study Al₂O₃ NMIs separation time across ladle, tundish, and mold steel – slag interfaces. It was found that the interfacial capillary force plays an important role in the separation process of NMIs. Note that this was the

first study to consider the shape of NMIs, as previous studies simplified the shape of NMIs to be a sphere.

In Yang et al.'s study [123], two limitations in previously proposed models were identified. The first was that previous models ignored differences in forces around the steel and slag phases but instead only considered interfacial particle forces. The second was that the model assumptions of a Reynolds number for NMIs being less than one and Stokes flow for NMIs moving around the interface do not match the facts. Therefore, they further developed a mathematical model based on force balance analysis for inclusion at different stages (shown in **Fig. 2.7** [123]). Different equations based on the range of Reynolds number were employed to calculate the terminal velocity for NMIs, as shown in equations 2.7 – 2.9. [123] They found that a small steel – slag interfacial tension, and steel – NMI interfacial tension, or large NMI – slag interfacial tension promotes particle separation through the interface and enters the slag phase. Another interesting phenomenon observed in their study was that the final particle position was only related to the particle wettability and displacement. [123]

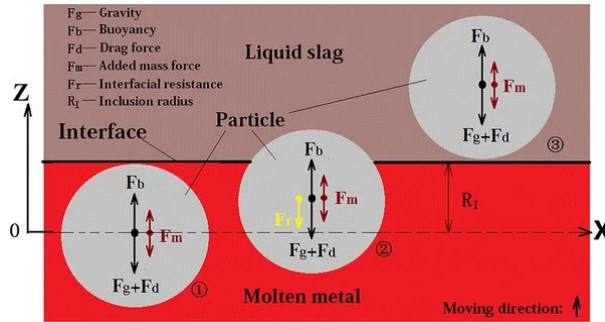


Figure 2.7 Schematic of forces acting on inclusions [123] (Reprinted with permission)

$$U = \frac{(\rho_l - \rho_p) * g * d_k^2}{18\mu}, \quad Re \leq 1 \quad 2.7$$

$$U = \left(\frac{4(\rho_l - \rho_p)^2 * g^2}{225\mu * \rho_l} \right)^{1/3} * d_k, \quad 1 < Re \leq 500 \quad 2.8$$

$$U = \left(\frac{3.03g * (\rho_l - \rho_p) * d_k}{\rho_l} \right)^{1/2}, \quad Re > 500 \quad 2.9$$

where U is the terminal floating velocity of inclusion (m/s), ρ_p and ρ_l are the densities of the NMI and molten steel (kg/m^3), d_k is the equivalent spherical diameter of the NMI (μm), g is the gravitational acceleration (m/s^2), μ is the viscosity of molten steel ($\text{Pa}\cdot\text{s}$).

Liu et al. [124, 125] further developed Yang et al.'s [123] modified model by incorporating the effect of fluid flow containing NMIs with different Reynolds numbers on the drag force to study

the motion behavior of NMIs at the molten steel – slag interface. It is important to note that a water model experiment was conducted to validate their mathematical model, and experimental results of the particle velocity crossing steel – slag interface agreed well with those predicted by the model. They found that the interfacial tension between slag and steel depressed the separation of NMIs, and small NMIs (diameter < 10 μm) cannot permeate into the slag layer and ultimately reside at the interface. Furthermore, the displacement of NMIs after entering the slag layer decreased with increased slag viscosity. [124, 125] More recently, Xuan et al. [126] developed a force balance-based mathematical model that incorporates the pressure force to study the motion and detachment behaviors of NMIs at the molten steel – slag interface. Their assumption of film formation was not included in previous mathematical models. They also introduced a parameter, the critical displacement Z_{cri} , to determine whether the film drains or remains. For example, if the displacement of the NMI exceeds Z_{cri} , the film drains, leading to detachment. Otherwise, the NMIs rebound into the steel. The value of Z_{cri} depends on the surface tension of slag and steel, and interfacial tension between them. All the parameters required in this model calculation were derived from an industry vacuum degassing trial. This model was validated by comparing predicted and experimental size distribution and number density (per mm^3) of NMIs in the steel sample at 0, 20, and 50 min vacuum treatment, showing a reasonable agreement. They found that the film drainage was the main stage of the NMI separation, and the capillary force was the main driving force of the NMI rebounding at the drainage stage. Overall, this mathematical model results showed that the separation time of NMIs is in micro-second once the separation occurred. [120-126]

The water model has also been used to explore the separation behaviors of NMIs at the molten steel – slag interface. Generally, water, oil, and paraffin wax/hollow particles have been employed to simulate liquid steel, liquid slag, and solid NMI, respectively. The schematic of the experimental setup is shown in **Fig. 2.8**. [125] NMIs particles were placed at the bottom of the container, secured by a net baffle. The container was filled with water and oil. During the experiment, the switch was opened to remove the net baffle, allowing particles to rise toward the oil. A high-speed camera captured the separation behavior of the particles at the oil – water interface. Magnelöv et al. [127] conducted water model experiments to simulate the separation behaviors of liquid NMIs at the steel – slag interface, where two types of oils (AK50 and OD40) were used as liquid NMIs. They observed that the rest time for AK50 liquid NMIs was more than 1 min in some cases due to the

formation of liquid film around the liquid NMI, and further that a higher viscosity of slag would increase the resistance to the liquid NMIs entering the top slag. Moreover, they compared NMI velocities from water model experiments with Stokes terminal velocities calculated using the same experimental parameters. The differences between the two velocities reached 22.6% for AK50 and 14.9% for OD40 liquid NMIs, suggesting that the discrepancy in NMI separation behaviors between the mathematical models and water model experiments was caused by using Stokes terminal velocity. [127] Zhou et al. [128] found that the variation of surface free energy helped particles enter the slag phase, whereas the decreases in the slag viscosity shortened the separation time. However, the deformation of the steel – slag interface could rise to the resistance, which would resist particles passing through the interface. A liquid film was observed to form on the top of the particle as it passed through the steel – slag interface in physical modeling experiments. This liquid film was only observed for spherical particles, not octahedral and plate-like ones. In addition, the separation time of NMIs depends on the properties of slag, steel, and NMIs, ranging from 0.5 to 30 s. This indicates that the separation process of NMIs crossing the molten steel – slag interface is observable. [128]

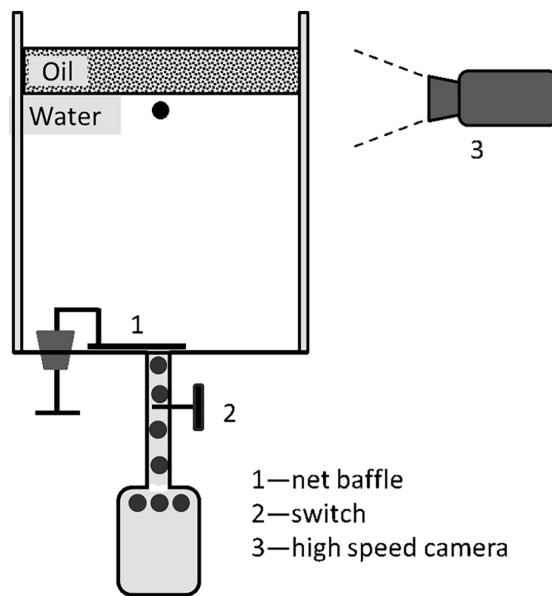


Figure 2.8 The schematic of the experimental setup to study the particle separation from water to oil using the water modeling technique [125] (Reprinted with permission)

Mathematical models suggest that NMIs' separation through the molten steel-slag interface is too fast to observe, while water models indicate it is observable. To investigate this further, lab experiments using a high-temperature confocal laser scanning microscopy (HT-CLSM) have been synchronously carried out to investigate the separation behaviors of NMIs at the molten steel – slag interface at temperatures ranging from 1470 to 1600°C. [129-133] This technique requires the slag used during the experiments to be transparent or at least semi-transparent, for observing the liquid steel – slag interface through the molten slag.

Misra et al. [129] were the first group to study separation behaviors of the NMIs at liquid steel – slag interface using HT-CLSM in the open literature. They found that once the NMIs emerged from the bulk metal, NMIs could remain at the interface for 3 – 5 s before either separating into slag or being re-emulsified to the steel. After that, few studies [130-132] have been carried to explore the separation behaviors of NMIs at steel – slag interface with a variation of steel, slag and NMI types by applying the same type of experimental technique. For example, Shannon et al. [131] and Coletti et al. [130] found that the separated NMIs had irregular shapes compared to the original spherical shapes and enriched in SiO₂ but depleted in CaO due to reactions with the slag phase based on the post SEM-EDS analysis on the composition of NMIs. Vantilt et al. [132] observed a remarkable type of star-like NMIs was only observed at the steel – slag interface when a SiO₂-containing slag was used. They suggested that it was due to the interaction between molten slag and NMIs. Coletti et al. [130] observed that NMIs clustered at specific locations of the steel – slag interface, which is unlike capillary depression-driven clustering observed at the molten steel surface. Wikströms et al. [133] conducted experiments to study the separation behaviors of Al₂O₃-CaO NMIs at the steel – slag interface at temperatures ranging from 1539 to 1569°C. However, they did not observe the separation of the Al₂O₃-CaO NMIs crossing the interface during the entire experiment. Instead, they identified two types of collisions: ‘free’ collisions, where NMIs moved independently without external forces, and ‘forced’ collisions, which occurred near solid corners of the liquid metal bath due to increased temperature or slag flow. However, none of them directly observed the separation of NMI into the slag, and they argued that the separation process takes less than one second. The mathematical model [118, 131] predicted that it is a microsecond process. The formation of a solid layer on the surface of the NMI through the chemical reaction between the NMI and slag was another claimed reason for not observing the separation process [130].

Mathematical and water model studies highlight the wettability of NMIs, the interfacial tension between slag and steel, slag and NMI, and NMI and steel, slag viscosity, and inclusion size as key factors in NMI separation. No high-temperature experiments directly observe NMIs separation at the molten steel – slag interface. However, the agglomeration of NMIs was observed at the molten steel – slag interface, suggesting partial separation into slag. This might be due to the fast separation time of NMIs (for both liquid and solid) on a microsecond scale, as modeling studies suggested. Another reason could be an experimental limitation of capturing the steel – slag interface precisely using confocal microscopy. Additionally, the formation of a liquid film during NMI separation at steelmaking temperatures remains unclear.

2.4.3 Dissolution of Non-Metallic Inclusion

When an NMI enters into liquid slag, it reacts with and potentially dissolves into the slag. Various methods have been employed to study NMI dissolution kinetics and mechanisms in molten slags at high temperatures, including the crucible test, dip test, and in-situ observation using a single hot thermocouple test and HT-CLSM.

This subsection critically reviews literature related to HT-CLSM, as all dissolution experiments in the present work were conducted using HT-CLSM. At the same time, studies on other experimental techniques and modeling approaches are briefly summarized.

2.4.3.1 Techniques

1) Crucible Test

The crucible test (cup test) is performed in an oxide crucible containing target slag, as shown in **Fig. 2.9**. [134] At high temperatures, the crucible reacts with the slag, and the dissolution of oxides is assessed by measuring the area or depth of the corroded region. This method is widely used to investigate the dissolution and corrosion of refractories, including Al_2MgO_4 , Al_2O_3 , MgO , MgO-C , $\text{Al}_2\text{O}_3\text{-SiC}$ in molten slags. [135-143] The primary advantage of the crucible test is its operational simplicity. However, a key limitation is that the corrosion rate is generally lower than in industrial conditions due to the absence of stirring, which significantly affects mass transfer. [134]

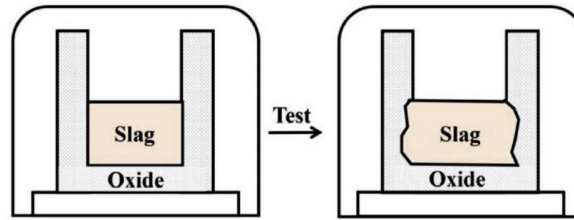


Figure 2.9 The schematic for the crucible test [134] (Reprinted with permission)

2) Dip test

The dip test is a corrosion/dissolution test in which a centimeter-size oxide rod is partially immersed into liquid slag at high temperatures for some time, removed, and then analyzed for slag corrosion and/or penetration by measuring microstructures, morphology, composition, and phase changes. The schematic apparatus is shown in **Fig. 2.10**. [144] The dip test can be classified as either a rotating or static test, depending on the experimental conditions, and is widely used to study refractory corrosion. It has also been extensively applied to investigate the dissolution of NMIs in molten slags at high temperatures. [35, 145-150] The setup could be modified to accommodate multiple samples simultaneously. [151, 152] Key advantages of the dip test include its simplicity, reliability, and flexibility in varying experimental parameters such as rotation speed, temperature, slag composition, substrate shape, and reaction atmosphere. [153] However, a limitation of the dip test in measuring the dissolution kinetics of NMIs is that the size of the immersed substrate is several magnitudes larger than the oxide particle, so it is questionable whether the data generated from the centimeter-sized NMIs can be applied to the kinetics and mechanisms at micro-size particle dissolution.

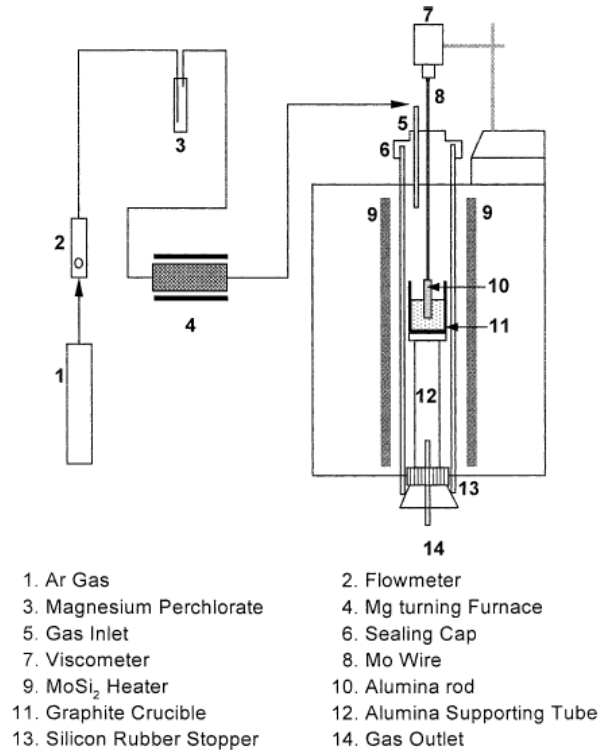


Figure 2.10 The schematic apparatus of the dip test [144] (Reprinted with permission)

3) Single hot thermocouple technique

The single hot thermocouple technique, originally developed to determine the microstructural change of a superconducting oxide [154], is also applied to study the dissolution behaviors of NMI particles in slag [155], as shown in **Fig. 2.11**. [156] In this method, slag powder is adhered to thermocouple wire using alcohol, and the oxide particle is introduced after reaching the target temperature. A camera records the dissolution process in real-time. The use of a platinum-rhodium thermocouple wire enables the system to achieve a maximum temperature of 1800°C, with heating and cooling rates of 9000°C/min and -1200°C/min, respectively. [155, 157, 158]

This technique has been widely applied to investigate the dissolution behaviors of Al₂O₃ and MgO particles in CaO-SiO₂-Al₂O₃-based slags. [156, 159-161] Its key advantages include rapid heating and cooling rates, minimal temperature difference between the sample and thermocouple, and the ability to introduce particles at experimental temperature, preventing pre-dissolution during heating. However, the technique has some limitations, including 1) a temperature drop occurs when introducing the sample, 2) the recorded images have limited resolution, and 3) temperature gradients can cause variations in slag composition.

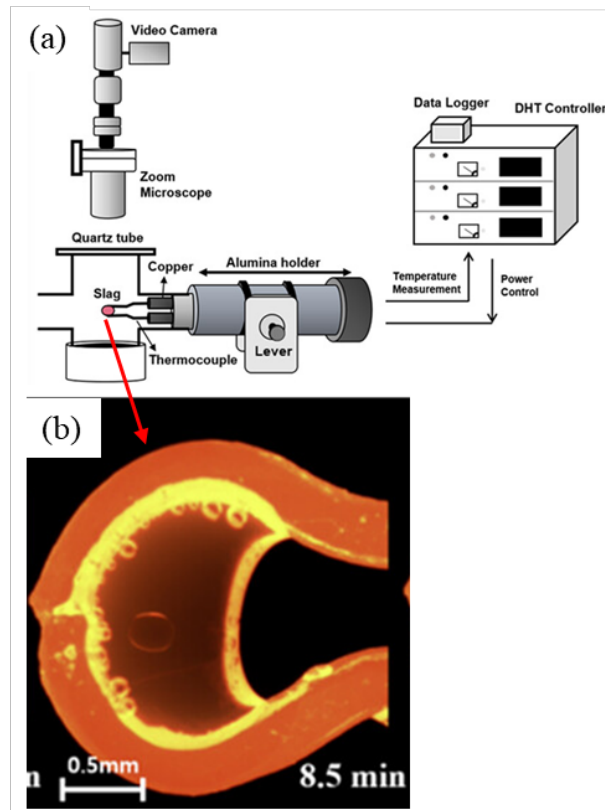


Figure 2.11 (a) The schematical illustration for the single hot thermocouple technique, and (b) a real-time image during the dissolution process [156] (Reprinted with permission)

4) High temperature-confocal laser scanning microscopy technique

Conventional fluorescence microscopy collects stray light, reducing image resolution. To address this, Marvin Minsky proposed the CLSM in 1956, incorporating a pinhole aperture to block stray light and enhance clarity. [162] His early design, a double-focusing stage scanning microscopy, used a stationary optical system with a moving stage. The setup focused a light beam through an objective lens onto the specimen, with transmitted or reflected light magnified before detection. Modern CLSMs improve stability and precision by using a moving light source instead of a moving stage.

HT-CLSM (high temperature CLSM), schematically illustrated in **Fig. 2.12**, [163] integrates an infrared gold-coated imaging furnace and a laser-based confocal optical system for real-time, high-temperature observations. A $\sim 0.5 \mu\text{m}$ focused laser beam is directed onto the specimen via a polarizing plate, a long-focus objective lens, and a quartz-covered viewport. Reflected light passes through a polarizing beam splitter and lens before being focused onto a CCD camera behind a pinhole, ensuring only focused light is collected. The paraboloid-shaped furnace houses a 1.5 kW

halogen lamp at one focus and the sample holder at the other, with high-purity argon controlling the atmosphere. The sample is heated by a halogen lamp light, reflected by the furnace onto a single point on the sample holder. [164] The main limitation of HT-CLSM is that the color of the slag needs to be transparent or at least semi-transparent for a clear observation of NMI dissolution, indicating the transition oxides, e.g., FeO and CrO_x should be avoided in the slag.

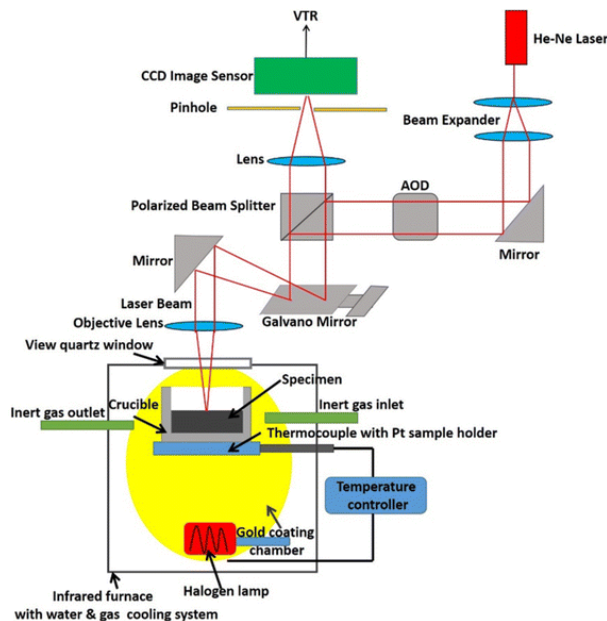


Figure 2.12 The schematical illustration of HT-CLSM [163] (Reprinted with permission)

The HT-CLSM (VL2000DX-SVF17SP, Yonekura) used in this study consists of the VL2000DX system, and SVF17SP system, as shown in **Fig. 2.13(a)**. The VL2000DX system includes a high-resolution, high-contrast VL2000 digital laser camera equipped with a 408 nm semiconductor laser as the light source, an MC1000A temperature controller, and VL2000DX basic software for temperature regulation and image/video recording. The SVF17SP system features an ultra-high temperature infrared gold-coated imaging furnace, optical microscopy, and cooling units. This HT-CLSM offers magnifications up to 3000X, with sample stage movement along the X and Y axis, and the laser camera adjustment along the Z axis. The theoretical highest depth (Z) and lateral resolutions of this HT-CLSM are 0.01 and 0.15 μm , respectively. The maximum heating and cooling rates are 50°C/s and 100°C/s, respectively.

Fig. 2.13(b) illustrates the sample setup. An NMI particle and platinum crucible containing pre-melted slag were placed in an alumina crucible positioned on a sample holder. A B-type thermocouple at the base monitors the temperature. The heating profile was pre-set in the PID-

regulated system to maintain the desired temperature. Hereafter, the term *particle* is used in HT-CLSM dissolution experiments instead of *NMI* to reflect the size difference. While NMIs typically have a radius of less than 50 μm in practice, the particles used in these experiments range from 50 to 500 μm .

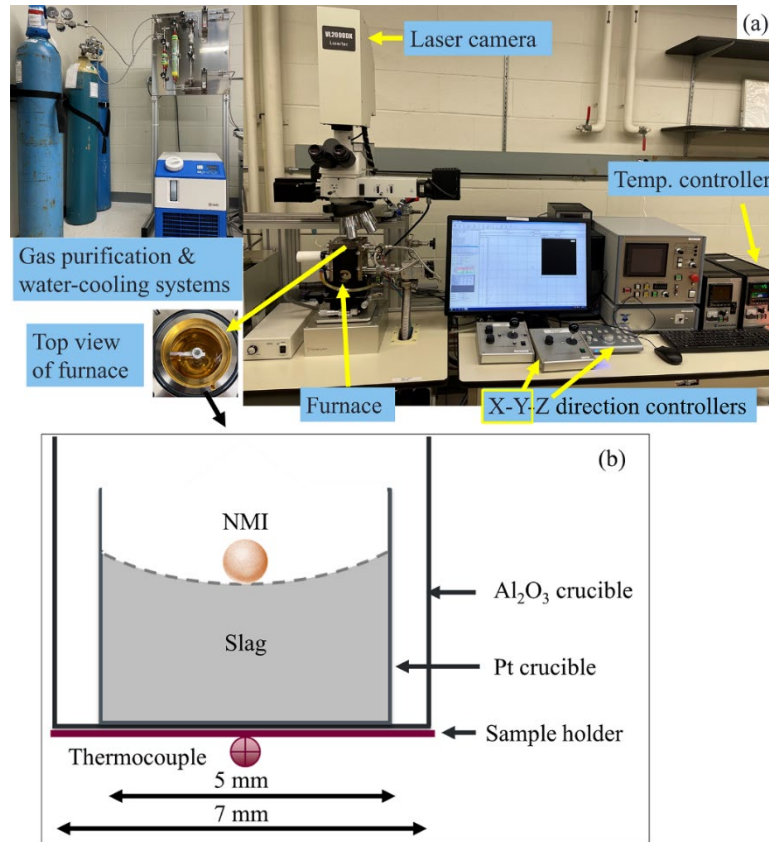


Figure 2.13 (a) the image of the HT-CLSM setup, and (b) the schematical illustration of the sample setup.

Over the past two decades, HT-CLSM has been developed and extensively used to investigate the dissolution behaviors of different types of particles in the steelmaking slag, as it enables continuous in situ observation of the behaviors of the particles under conditions relevant to the steelmaking process. Moreover, the particle's dissolution process is recorded as videos/images. The evolution of the apparent particle size is obtained as a function of time through image analysis. The dissolution mechanism and rate-limiting step of the particle can be revealed by comparing the experimental results with theoretical results predicted through the kinetic models, such as the shrinking core model and diffusion in the stagnant fluid model. These models are briefly explained below.

2.4.3.2 Determination of dissolution mechanisms

1) Shrinking core model

The shrinking core model (SCM) is used to describe and analyze the reaction kinetics of solid particles in which solid particles are consumed either by mass transport and/or chemical reactions, and, as a result, the amount of the material being consumed is shrinking in a fluid-solid system. It is important to mention that this model assumes that the particle is spherical. Many researchers have employed SCM to describe the dissolution mechanisms. [165-170] After dimensionless treatment of experimental data on particle size change with time [165-169, 171] The best fit between SCM prediction and experimental data usually offers the dissolution mechanism. These mechanisms are explained below.

Chemical reaction-controlled dissolution (CR)

For CR, schematically illustrated in **Fig. 2.14(a)**, where the undissolved particle is surrounded by molten slag as the transportation rate of the reactants from bulk slag to the particle – slag is much higher compared to that the chemical reaction at the interface, resulting the absence of the boundary layer. The dissolution rate is postulated to be determined by a constant dissolution rate coefficient, k_{con} (m/s). The time-dependent radius and total dissolution time (τ , s) are given as:

$$\frac{t}{\tau} = 1 - \frac{r}{r_0} \quad 2.10$$

$$\tau = \frac{\Delta C \rho_s r_0}{k_{con}} \quad 2.11$$

where r_0 and r (m) are the initial radius and radius at time t (s) of the particle, respectively. ΔC is the concentration difference of the dissolved species between the bulk slag C_s and saturation content C_b (kg/m^3). ρ_s is the density of slag (kg/m^3).

Boundary layer diffusion-controlled dissolution (BLD)

In the BLD [172], the dissolution rate is governed by the mass transfer/diffusion of the dissolved species through the boundary layer. As shown in **Fig. 2.14(b)**, the thickness of the boundary layer is independent of time variation, which means the concentration profile always keeps a constant shape. The time-dependent radius and total dissolution time are given as:

$$\frac{t}{\tau} = 1 - \left(\frac{r}{r_0}\right)^2 \quad 2.12$$

$$\tau = \frac{\Delta C \rho_s r_0^2}{2D} \quad 2.13$$

where D is the diffusion coefficient (m^2/s) of dissolved species in the molten slag.

2) Shell layer diffusion-controlled dissolution (SLD)

In the SLD, the rate-controlling is the mass diffusion through a shell (solid) layer (**Fig. 2.14(c)**). The mass flux inside the shell layer is independent of the intermediate location. The time-dependent radius and total dissolution time (τ) are given as:

$$\frac{t}{\tau} = 1 - 3\left(\frac{r}{r_0}\right)^2 + 2\left(\frac{r}{r_0}\right)^3 \quad 2.14$$

$$\tau = \frac{\Delta C \rho_s r_0^2}{6D} \quad 2.15$$

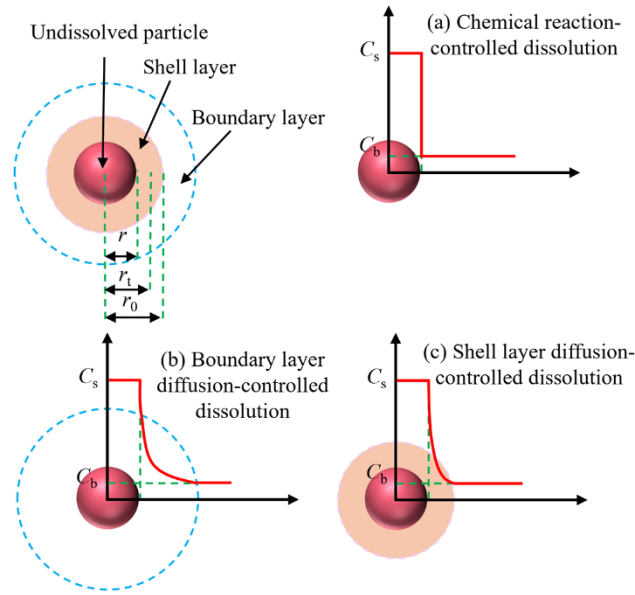


Figure 2.14 Schematic illustration of particle dissolution based on the shrinking core model under mechanisms of (a) Chemical reaction-controlled dissolution (CR), (b) Boundary layer diffusion-controlled dissolution (BLD), and (c) shell layer diffusion-controlled dissolution (SLD)

Xuan and Mu [170] analyzed the dissolution profiles of the particles and observed that they are sometimes located at a particular transition position between the sigmodal profile and parabolic profile. Then, they modified SLD by introducing a parameter φ and proposed a more generalized equation to represent the experimental data. They named it diffusion distance-controlled dissolution (DDD) to fully match general dissolution cases. The time-dependent radius and total dissolution time (τ) are given as:

$$t = \frac{\rho_s r_0^2}{6\Delta C} \left[(3 - 2\varphi) - 3\left(\frac{r}{r_0}\right)^2 + 2\varphi\left(\frac{r}{r_0}\right)^3 \right] \quad 2.16$$

$$\tau = \frac{\rho_s r_0^2 (3 - 2\varphi)}{6\Delta C} \quad 2.17$$

φ is the profile coefficient that controls the distance of diffusion control and depends on the experimental temperature and slag viscosity, and its variation is in the range from 0 to 1. Equation 2.16 was validated by HT-CLSM experimental data for SiO_2 , Al_2O_3 , and MgAl_2O_4 dissolution from the literature, and it showed a reasonable agreement with experimental results. As shown in **Fig. 2.15**, the BLD and SLD model predictions are two extreme cases of the DDD mechanism rather than two different mechanisms.

However, concerns remain regarding the applicability of the SLD and DDD models in determining the rate-limiting step of particle dissolution, despite their agreement with some experimental results. Both models assume the formation of a persistent solid layer throughout dissolution, which contradicts the observed complete disappearance of particles.

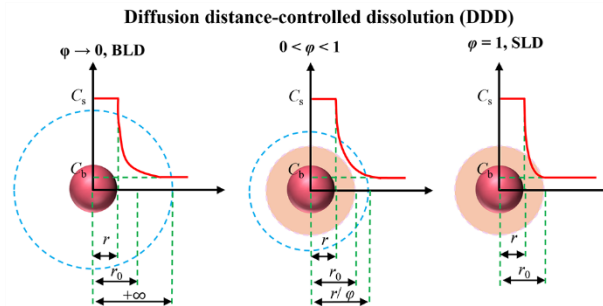


Figure 2.15 Schematic illustration of the particle dissolution using the diffusion distance-controlled dissolution model

The SCM has been widely applied to study the dissolution mechanism of particles, such as Al_2O_3 [165, 166, 168, 171, 173-181], MgO [166, 174, 176, 182], CaO [183, 184], $\text{MgO}\cdot\text{Al}_2\text{O}_3$ [166, 185], $\text{CaO}\cdot 2\text{Al}_2\text{O}_3$ [169] and $\text{TiO}_2\cdot\text{Al}_2\text{O}_3$ [186-188] in $\text{CaO}\text{-SiO}_2\text{-Al}_2\text{O}_3$ type slags with or without MgO at temperatures between 1450 and 1600°C. It is generally accepted that the rate-limiting step for the dissolution of Al_2O_3 is BLD. Fox et al. [176] exceptionally suggested that the rate-limiting step is CR for dissolving Al_2O_3 inclusions. The authors didn't discuss the reason for such a difference. However, it might be caused by the slag properties since they used a commercial mold slag consisting of $\text{SiO}_2\text{-CaO-MgO-Na}_2\text{O-Al}_2\text{O}_3\text{-B}_2\text{O}_3\text{-ZrO}_2$.

Liu et al. [165, 182] suggested that the rate-limiting step for MgO dissolution is BLD, while Valdez et al. [174, 176] claimed that CR is the rate-limiting step in the same slag system. It should be noted that none of the actual dissolution curves perfectly fit the theoretical curves suggested by the SCM. Guo et al. [183, 184] found that the dissolution profile of CaO works well with that of CR in the slag containing MgO . Monaghan et al. [174, 185] proposed that the BLD at least partly

controls the dissolution mechanism of $\text{MgO}\cdot\text{Al}_2\text{O}_3$ particles, and the diffusion coefficients obtained were in the range of $0.76 - 2.2 \times 10^{-10} \text{ m}^2/\text{s}$. Miao et al. [169] reported that the rate-limiting step for the $\text{CaO}\cdot 2\text{Al}_2\text{O}_3$ particle dissolution is BLD at 1550°C and 1600°C . The diffusion coefficients obtained from the experiments range from 5.64×10^{-12} to $5.8 \times 10^{-10} \text{ m}^2/\text{s}$. Sharma et al. [188] found that the dissolution of $\text{TiO}_2\cdot\text{Al}_2\text{O}_3$ was much faster than that of Al_2O_3 in the same slag. BLD was determined as the rate-limiting step for $\text{TiO}_2\cdot\text{Al}_2\text{O}_3$ particle dissolution. Moreover, they proposed the dissolution path for $\text{TiO}_2\cdot\text{Al}_2\text{O}_3$, *i.e.*, the aluminum titanate firstly dissociated into alumina, titanium oxide, and oxygen while the liquid slag penetrated through the particle, then alumina and titanium oxide dissolved in liquid slag, and oxygen leaves the system.

In some cases, the differences between the curves of CR and BLD are comparable due to the experimental scatter. Both theoretical curves fit similarly with experimental data, so it is hard to verify the rate-limiting step by directly comparing them. The rate-limiting step can be further clarified by changing slag viscosity since the dissolution rate of CR is only influenced by temperature. In contrast, viscosity significantly affects the dissolution rate of BLD by influencing the diffusion coefficient.

3) Diffusion in stagnant fluid model

Diffusion in the stagnant fluid model (DS) describes micro-particle dissolution due to concentration differences in a fluid without convection. Dissolution controlled by the diffusion in stagnant flow can be mathematically described by Fick's first and second law of diffusion. [189-191] In the DS, an invariant interface is approximated. In other words, the diffusion field would stay as the particle – slag interface was fixed at the start of the dissolution process. The driving force of the diffusion is the concentration gradient of the dissolving particle at the interface between the particle and the slag. The diffusion equation used to express DS is given as follows:

$$\frac{dr}{dt} = -\frac{a \cdot D}{r} - a * \sqrt{\frac{D}{\pi * t}} \quad 2.18$$

where a is the dimensionless saturation, $a = (C_{\text{sat}} - C_0)/(C_p - C_{\text{sat}})$. C_0 , C_{sat} and C_p denote the component content in the slag, at saturation, and in the particle, respectively. In contrast to the SCM, which provides a simple analytical solution, the diffusion equation must be solved numerically.

In some cases, the SCM could hardly describe the experimental results when the diffusion in the liquid slag occurred at a long distance instead of a thin boundary layer. [168, 178, 192-195]

Verhaeghe et al. [168, 178, 192] applied both SCM and DS to determine the dissolution mechanism of Al₂O₃ particles in CaO-SiO₂-Al₂O₃ type steelmaking slags at temperatures between 1470 and 1630°C. They found that DS shows better agreement with experimental data. The obtained diffusion coefficients ranged from 2.4*10⁻¹¹ to 9.7*10⁻¹¹ m²/s. Feichtinger et al. [195] found that none of the CR, BLD, and DS fit well with their experimental results of SiO₂ dissolution in a steelmaking type slag at 1450°C. Since the shape of dissolution curves of the SiO₂ particle varied as a function of slag composition, they observed a parabolic-like shape for low SiO₂-containing slags and an S-shape with higher SiO₂-containing slags. They introduced a fitting parameter, *f* (between 0 and 1), to the second term of equation 2.18 to describe the dissolution of SiO₂. The slag viscosity determines the value of *f*.

$$\frac{dR}{dt} = -\frac{a \cdot D}{R} - f * a * \sqrt{\frac{D}{\pi * t}} \quad 2.19$$

The dissolution profiles predicted by the modified DS fit well with the experimental curves from different slags. The diffusion coefficient for SiO₂ at 1450°C ranged from 4.44*10⁻¹¹ to 2.38*10⁻¹⁰ m²/s. The same dissolution mechanism of SiO₂ has been reported by Tian et al.[193] and Ren et al. [194]

Without applying SCM and DS to study particle dissolution mechanism and rate, Park et al. [167] revealed the dissolution mechanism of Al₂O₃ and MgO particles in the CaO-Al₂O₃-SiO₂ type slags at 1550°C by post analysis at the particle – slag interface using SEM-EDS. They identified three different dissolution mechanisms for Al₂O₃ and MgO particles in molten slags: 1) direct dissolution of the particle into the molten slag without forming any reaction products. 2) the formation of a dense, needle-like oxide layer on the particle surface, preventing slag penetration and resulting in a linear dissolution rate, 3) tiny reaction products initially formed on the surface of the undissolved particle, then detached from the surface and accumulated into a ring with time surrounding the undissolved particle This created an inner liquid phase between the product ring and the particle, where dissolution first occurred before diffusion through the ring into the bulk slag. The dissolution rate is slower compared to that of direct dissolution.

Further studies are needed to investigate particle dissolution mechanisms in molten slag using post-analysis methods, as conventional models have not accounted for solid product formation and its effects on dissolution. This research could provide deeper insights into dissolution mechanisms

and enable the development of improved models that incorporate solid product formation during the process.

2.4.3.3 Determination of the dissolution rate

The PFM was developed and applied to study the dissolution time of NMIs in molten slag due to its ability to simultaneously describe the dissolution kinetics, diffusion profiles, and morphology of the individual phase. Liu et al. [196] first applied the PFM developed by Heulens et al. [197] to investigate the dissolution of Al_2O_3 NMIs in $\text{CaO-Al}_2\text{O}_3\text{-SiO}_2$ slag. The PFM was validated against an analytical model and experimental data from the literature by comparing the interface position, showing a reasonable agreement. PFM predictions indicated that the dissolution rate of Al_2O_3 NMIs increased with higher temperature and CaO content at a fixed Al_2O_3 content or lower Al_2O_3 content at a fixed CaO/ SiO_2 ratio in the slag. [196] However, the simulated NMI size ($0.2 * 0.2 \mu\text{m}$) was much smaller than real NMIs due to the restriction of the diffusion interface width and diffusion equations, resulting in the dissolution time being less than 0.005 s, which limited its further application. To address this, Xuan et al. [198] developed this PFM by refining the diffusion interface and diffusion equations, enabling to study the isothermal dissolution of Al_2O_3 NMI in liquid slag with size up to 100 μm , assuming diffusion control at the NMI – slag interface. This model was validated by experimental data using HT-CLSM from literature. Their model findings indicate that increasing Al_2O_3 content in the slag while maintaining a similar CaO/ SiO_2 ratio or decreasing MgO content at a low CaO/ SiO_2 ratio prolongs the dissolution time of Al_2O_3 due to the increase in network former or decrease in network breaker. Moreover, they examined the impact of the NMI morphology on the dissolution time and found that irregularly shaped (triangle) NMIs dissolve faster than those with regular shapes (spherical) of the same volume due to their larger contact area. The current PFM has some limitations, including the requirement for parameters such as interfacial energy between NMIs and liquid slag and the diffusion coefficient, which are often unavailable.

Kwon et al. [199, 200] developed a multi-ion diffusion model within the framework of non-equilibrium thermodynamics proposed by Groot et al. [201] This model couples the tracer diffusivities of ions and chemical potentials to simulate the dissolution of solid NMIs in $\text{CaO-Al}_2\text{O}_3\text{-SiO}_2$ slag. Validation was performed by comparing predicted dissolution curves of spherical Al_2O_3 and SiO_2 NMIs with experimental data from the literature, showing a reasonable agreement. A key advantage of this model is its consideration of various diffusion species, including

independent ions, coupled ions, and oxides, challenging the commonly used assumption that diffusion occurs through bulk oxides like CaO, SiO₂, and Al₂O₃. [200] However, further studies are needed to expand its application to NMI dissolution. Notably, both the PFM and multi-ion diffusion models neglect NMI motion, chemical reactions, and thermal convection during dissolution. [197, 200]

2.4.3.4 Effect of parameters on the dissolution kinetics

1) Effect of particle behavior and velocity

Previous studies reported that NMIs not only dissolve but also move, rotate, and dissociate within the molten slag during dissolution experiments via HT-CLSM, as schematically illustrated in **Fig. 2.16**. Such phenomena could significantly impact dissolution mechanisms and kinetics by altering the fluid dynamics at the oxide-slag boundary, resulting in the shape change of the experimental dissolution curve [175, 182, 202]. Unfortunately, none of CR, BLD, and DS account for the motion of particles. Pan et al. [202] incorporated the velocity of NMIs via the Péclet number to consider the convective mass transfer of the dissolving component. A better fit was obtained between model predictions and experimental results. However, the velocity was calculated based on the rotation of the NMIs, which normally only occurs for a specified duration and not over the entire dissolution process based on other in situ experiments. [182, 184] As a result, the fixed angular velocity likely does not accurately represent the true velocity over time.

Another factor affecting the dissolution kinetics beyond particle motion that must be considered is the porosity of particles, which affects the particle's surface area. Since inclusion agglomeration occurs during industrial operations, the morphology of such agglomerated inclusions has been well studied, showing that they have porosity. [37, 203] For example, Yin et al. [204] observed that solid calcium aluminate NMIs were irregular in shape with coarse tips and pores. However, very limited information is available regarding the impact of particle porosity on its dissolution kinetics in the open literature. [205]

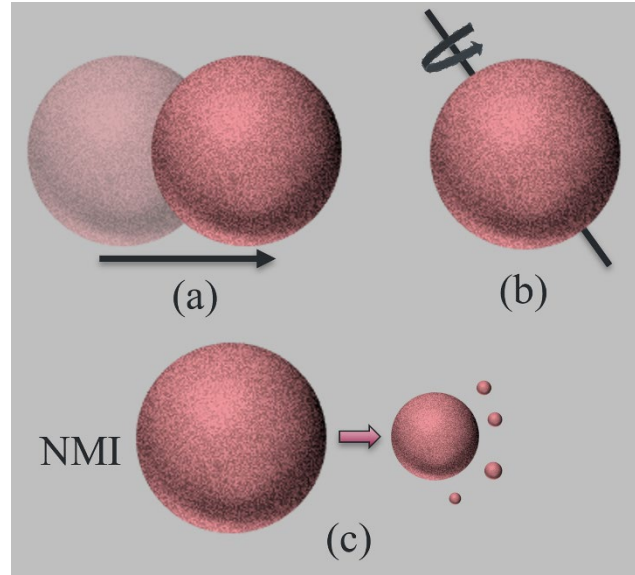


Figure 2.16 Potential particle behavior during dissolution: (a) motion, (b) rotation, and (c) dissociation

2) Effect of temperature

It is well known that the dissolution rate for particles increases with increasing temperature. The effect of temperature on the dissolution rate of particles could be explained from a thermodynamic and kinetic point of view. [168, 171, 177, 180, 183, 184] Thermodynamically, if a local equilibrium is assumed at the particle – slag interface, the driving force for the particle dissolution is related to the concentration difference of the particle between the particle – slag interface and the bulk of the slag. The former can be evaluated from the phase diagram given by the saturation limit. The temperature significantly affects the dissolution rate of the particle by changing this driving force, which means increasing temperature, the saturation concentration of the particle would increase in general. Kinetically, the influence of temperature on the potential rate-limiting step, CR and BLD, can be considered. For the first-order chemical reaction, the rate equation for the particle dissolution is given:

$$J = k * \Delta C \quad 2.20$$

where J is the molar flux of the particle per unit area and represents the dissolution rate, and k is a rate constant.

For BLD, Fick's first law can be applied to the diffusion across the boundary layer. Then the equation for the particle diffusion in the boundary layer is given:

$$J = -D * \frac{\Delta C}{\delta} \quad 2.21$$

where D diffusion coefficient of particle, δ is the boundary layer thickness.

An Arrhenius relation describes the temperature dependency of both k and D : [171]

$$k = k_0 * e^{-E_{a1}/(RT)} \quad 2.22$$

$$D = D_0 * e^{-E_{a2}/(RT)} \quad 2.23$$

where k_0 and D_0 are constants, E_{a1} and E_{a2} are activation energies (kJ/mol), R is the universal gas constant, and T is the temperature (K).

It is clear from equations 2.20 and 2.21 that k and D increase with increasing temperature and, thereby, J increases as well.

3) Effect of slag properties

Two critical parameters for particle dissolution are the concentration difference of species (ΔC , driving force) and slag viscosity (μ), which highly depend on the slag composition. High ΔC and low μ would accelerate the dissolution process and decrease the risk of the particle being entrapped back into molten steel. Based on this knowledge, Ren et al. [180, 181] proposed a correlation between the dissolution rate of Al_2O_3 particles and driving force and slag viscosity, as shown in equation 2.24.

$$DR = 18.716 \times \frac{\Delta C}{\mu} \quad 2.24$$

where DR is the dissolution rate ($\mu\text{m}^3/\text{s}$). μ is the viscosity of slag (Pa·s).

They found a reasonable agreement between their equation and experimental data available in open literature. They [194] also proposed another correlation to predict the dissolution rate of SiO_2 particles, as shown in equation 2.25.

$$DR = 800.29 \times \frac{\Delta C}{\mu} \quad 2.25$$

The constant values in equations 2.24 and 2.25 were suggested based on linear fitting of their experimental data.

Additionally, the particles could react with slag and form intermediate solid products, which might influence their dissolution behaviors. Park et al. [167] reported the formation of reaction products, e.g., $\text{CaO} \cdot 6\text{Al}_2\text{O}_3$, $\text{CaO} \cdot 2\text{Al}_2\text{O}_3$, and $2\text{CaO} \cdot \text{Al}_2\text{O}_3 \cdot \text{SiO}_2$ on the surface of Al_2O_3 particle, but the reaction products did not retard Al_2O_3 dissolution rate. In contrast, they [206] observed a unique dissolution phenomenon during MgO dissolution. The reaction products of $\text{MgO} \cdot \text{Al}_2\text{O}_3$ and $2\text{CaO} \cdot \text{SiO}_2$ formed a ring-like structure around MgO particles. Inside the ring-like structure,

liquid phases corresponded to the co-saturation compositions with $\text{MgO}\cdot\text{Al}_2\text{O}_3$ and $2\text{CaO}\cdot\text{SiO}_2$ phases. This phenomenon retarded the dissolution rate of MgO particles in molten slag.

2.4.3.4 Sources of error in the data using HT-CLSM

Many researchers have documented instances of data scatter or errors in their experimental curves. [168, 169, 171, 177, 180, 183, 184, 195] Several potential sources have been identified as contributing factors to this issue. Firstly, non-spherical particles were employed in the experiments while employing kinetic analysis based on a spherical particle assumption. Secondly, particles' rotation and motion behaviors during the dissolution process can potentially introduce errors and impede the determination of the dissolution mechanism, as particle motion can disrupt the diffusion fields surrounding the particle. Thirdly, the presence of gas bubbles originating from the slag can affect the particle dissolution process upon contact. Note that in some cases, the size of certain gas bubbles exceeds that of the particles themselves. Finally, an error may arise when measuring the projection area of the particle within the 2D frame, necessitating caution when defining the particle boundary during image analysis procedures.

In summary, the dissolution behaviors of solid single-phase particles, such as Al_2O_3 , SiO_2 , and MgO, have been well-studied in various slags at high temperatures using HT-CLSM. It is established that 1) the dissolution of solid particles is primarily controlled by the mass transfer/diffusion of the dissolved component in the molten slag, 2) Higher temperatures, increased concentration difference between the particle – slag and the bulk slag, and lower slag viscosity enhance the dissolution kinetics, and 3) the intermediate solid products may form and affect the dissolution, and 4) particle motion and rotation could occur, and potentially introducing experimental uncertainties. However, research on the dissolution behavior of complex NMIs, particularly CA2 and CA6, remains limited. The influence factors, such as particle motion, porosity, and the formation of intermediate solid products, on their dissolution behaviors are not yet well understood. Additionally, one main limitation of the conventional models is their inability to account for the effect of convection on particle dissolution behavior, which may significantly influence the dissolution kinetics.

2.5 Theories, Structure, and Properties of Slag

Slags in pyrometallurgical operations are multicomponent systems composed of oxides such as CaO, MgO, Al₂O₃, SiO₂, and FeO. The main functions of refining slags include 1) preventing heat loss of liquid steel, 2) Protecting liquid steel from reoxidation by air, 3) acting as a reservoir for chemical reactions, and 4) an absorber of NMIs and other impurities. [18] Understanding and controlling slag properties, including viscosity, melting point, surface tension, and thermal conductivity, are critical to achieving these objectives.

2.5.1 Theories of Slag

Various theories have been developed to describe slag properties, particularly to estimate the activities of slag components at higher temperatures, where direct measurement is challenging due to the corrosive nature of slag systems. These theories can be broadly classified into ionic, molecular, and ionic and molecular coexistence theories.

Ionic theory

Temkin [207] and Herashymenko [208] proposed a hypothesis, also called Temkin Theory, which assumes that the slag consists of two separate sets of ideal solutions of cations and anions, where 1) slag components fully dissociate into ions, and 2) ions of the same charge do not interact, implying complete randomness. Flood et al. [209, 210] further extended this theory by incorporating equilibrium between slag ions, dissolved compounds, and dissolved elements in the metal phase, assuming ideal behavior for ions in the slag and nonideal behavior for elements in the metal phase. The developed theory is named Flood Theory. Moore et al. [211] further explored the application of Flood Theory in complex slags and the phosphorus-oxygen equilibrium between slag and metal.

Masson [212, 213] extended the conventional polymer theory to account for complex anions beyond SiO₄⁴⁻, and to calculate the activity of basic oxides in silicate slags, assuming 1) slags as complex solutions containing polymeric silicate anions and 2) ideal behavior for cations and anions. Masson Theory treats silicates as simple chain units and branched chain units.

Molecular Theory

This theory suggests that 1) the slag consists of molecules rather than ions, simple oxides, e.g., CaO, MnO, FeO, Fe₂O₃, Al₂O₃, and SiO₂ either associate to complex molecules such as Ca₂SiO₄ or remain as free compounds, 2) ideal behaviors for all molecules. [57]

Ion and Molecular Coexistence Theory

Chuiko [214] first proposed this theory and then it was further developed by Zhang et al. [215]. This theory suggests that the structure unit of slag consists of simple ions, simple molecules, and complex molecules, as indicated in the phase diagram. The mass action law is used to determine the activities of the units. [216, 217]

Each theory has inherent assumptions that limit its applicability to real slags, and no single model is universally valid across all slag systems.

2.5.2 Slag Structure

In accordance with the polymer- and structure-based theories [218], oxides can be categorized into three types. The first type is “acid oxide,” which forms intricate three-dimensional networks of anion complexes, exemplified by SiO₂. The second type is “basic oxide,” which disrupts those networks like CaO. The third type is “amphoteric oxide” which is not distinctive, typified by Al₂O₃.

Another way to characterize slag structure is through a term known as parameter Q , which quantifies the degree of polymerization of a slag. For example, in the CaO-Al₂O₃-SiO₂ slag system, Q can be determined via:

$$Q = 4 - NBO/X_T \quad 2.26$$

$$NBO = 2(X_{CaO} - 2X_{Al_2O_3}) \quad 2.27$$

$$X_T = X_{SiO_2} + 2X_{Al_2O_3} \quad 2.28$$

where NBO is the number of non-bridge oxygen atoms, X_T is the number of tetragonally-coordinated atoms, and X_i is the molar ratio of component i in the slag.

A higher Q indicates a greater polymerization degree of the molten slag and, consequently, reduced mobility of dissolving species within the slag.

2.5.3 Slag Properties

Viscosity is one of the most important properties of molten slag, which governs the heat and mass transfer and affects the reaction kinetics in the molten slag and at the slag – steel interface. [21,22] It depends on the composition of ions in the slag. Different models have been developed to calculate viscosity, such as the Urbain Model [219], the Riboud Model [220], the KTH Model [221], and the Quasichemical Solution Model [222, 223]. Generally, the slag viscosity with a given composition decreases exponentially with an increase in temperature. Moreover, decreased acid

oxides like SiO_2 and increased basic oxides and halides like CaO and MgO lower slag viscosity. [224]

Basicity is a concept that describes the ratio of basic oxides to acid oxides or the ratio between the network breaker component and the network former component in the slag. [225] As mentioned above, the oxides in the slag can be divided into two groups: 1) acid oxides, which accept oxygen anions and form complex anions, and 2) basic oxides, which donate oxygen anions and form cations. Since amphoteric oxides, such as Al_2O_3 and Cr_2O_3 , act as basic oxides or acid oxides for the fixed slag composition. The basicity index used to present the slag structure, in general, is defined as the ratio of the total of basic oxides to the total of acid oxides in weight percentage. The most common basicity index used in industry is the binary basicity index, CaO/SiO_2 (wt.%) ratio. [18]

Surface tension plays a critical role in mass transfer during steel refining, affecting the interfacial tension between metal and slag in various phenomena, such as slag – metal emulsion, slag foaming, coagulation of nonmetallic inclusions, and their separation from the liquid steel bath. [226-228] Surface tension is predominantly determined by the surface-active components, such as B_2O_3 and CaF_2 , rather than the bulk composition. [229] High surface tension retards the slag entrainment into the liquid steel, while low surface tension promotes the separation of NMIs from liquid steel into the top slag. [230, 231]

Oxidizing power defines the slag's ability to transfer oxygen to the metal bath, and it is primarily governed by iron oxide activity. [18] The high oxidizing power of slag enhances the diffusion of oxygen metal bath and reoxidation during secondary steelmaking.

2.6 Summary

This Chapter has provided a review of NMI formation, modification, and removal during secondary steelmaking, focusing on NMI dissolution using HT-CLSM. Moreover, slag structure and properties are briefly presented. In the context of NMI modification via calcium treatment, the formation of undesired solid calcium aluminate products CA_2 and CA_6 can occur if the amount of calcium added to liquid steel is insufficient or excessive. Furthermore, CA_2 and CA_6 may also form due to interactions among liquid steel, top slag, and refractories. These NMIs adversely affect both steel castability and final product quality.

Extensive studies have investigated the dissolution kinetics of solid NMIs under varying temperatures, slag compositions, and NMI's sizes using HT-CLSM. Conventional models have been applied to determine dissolution mechanisms. However, most of these studies focus on single-phase NMIs, i.e., Al₂O₃, MgO, CaO, SiO₂, TiN, and Ti₂O₃, while research on complex NMIs, especially for CA2 and CA6, remains limited. Moreover, conventional models do not consider the impact of NMI's velocity and porosity on the dissolution kinetics, despite numerous studies reporting the motion, rotation, and clustering of NMIs. In addition, while some studies have experimentally examined the dissolution path evolution of NMIs, most rely on thermodynamic calculations under equilibrium conditions.

From the scientific angle, several knowledge gaps in literature require further investigation. Questions, such as how would slag composition and temperature affect the dissolution kinetics and mechanism of CA2 and CA6? How will the velocity and porosity of CA2 and CA6 affect their dissolution behaviors? And can a model be developed by incorporating the two features to predict the dissolution time? Is it possible to experimentally validate the evolution of the dissolution path predicted by thermodynamical models? Once the intermediate solid products form, how do they affect the dissolution behaviors of CA2 and CA6? These questions are not clearly answered.

To address the knowledge gaps, a comprehensive understanding of the dissolution kinetics and mechanisms of complex oxide particles, CA2 and CA6, and examining the influence of both process parameters and intrinsic particle properties on dissolution behaviors are essential. Subsequent chapters will present the author's approach to answering these questions.

2.7 References

1. W.M. Lord: *Transa. of Newco. Society* 1945, vol. 25, pp. 163-80.
2. L. Holappa: *Miner. Process. Extr. Metall. Rev.* 2018, vol. 128, pp. 3-16.
3. R.L. Guthrie and M.M. Isac: *Met.* 2022, vol. 12, p. 862.
4. M. Rasch: *Stranggieben—Continuous Casting; A Technical Revolution in the Steel Industry*; Aschendorff Verlag: Münster, Germany 2017, pp. 9-40.
5. <https://www.eurofer.eu/about-steel/learn-about-steel/what-is-steel-and-how-is-steel-made>
Accessed January 2025
6. I. Holappa: In *Treatise on Process Metallurgy*, Elsevier: 2014, pp 301-45.
7. S.K. Dutta and Y.B. Chokshi: In *Basic Concepts of Iron and Steel Making*, 2020, pp 497-536.
8. A. Ghosh: *Secondary steelmaking: principles and applications*. CRC Press, 2000.
9. L.F. González, D.F. González, and J.I. González: *Operations and basic processes in steelmaking*. Springer International Publishing, 2021.

10. In https://www.substech.com/dokuwiki/doku.php?id=ladle_refining.
11. L.F. Zhang and B.G. Thomas: *ISIJ int.* 2003, vol. 43, pp. 271-91.
12. J.H. Park and H.Todoroki: *ISIJ int.* 2010, vol. 15, pp. 1333-46.
13. Z.L. Wang and Y.P. Bao: *Int. J. Miner., Metall. Mater.* 2024, vol. 31, pp. 18-32.
14. V.L.F. Silva, L.J.L. Silva, S.E. Aguiar, and A.C. Silva: *J. Mater. Res. Technol.* 2019, vol. 8, pp. 3453-58.
15. P.G. Jönsson and L.T. Jonsson: *ISIJ Int.* 2001, vol. 41, pp. 1289-302.
16. J.L. Szekely, G. Carlsson, and L. Helle: *Ladle metallurgy*. Springer Science & Business Media, 2012.
17. L. Holappa and O. Wijk: In *Treatise on Process Metallurgy*, 2014, pp 347-72.
18. M. Shamsuddin: *Physical chemistry of metallurgical processes*. Springer, 2016.
19. Z.L.Wang and Y.P. Bao: *Int. J. Miner., Metall. Mater.* 2024, vol. 31, pp. 18-32.
20. K.P. Wang, M. Jiang, X.H. Wang, Y. Wang, H.Q. Zhao, and Z.M. Cao: *Metall. Mater. Trans. B* 2015, vol. 46, pp. 2198-207.
21. J.S. Park and J.H. Park: *Metall. Mater. Trans. B* 2014, vol. 45, pp. 953-60.
22. L.F. Zhang and B.G. Thomas: *ISIJ Int.* 2003, vol. 43, pp. 271–91.
23. H.V. Atkinson and G. Shi: *Prog. Mater. Sci.* 2003, vol. 48, pp. 457-520.
24. S. Seshadri: *Fundamentals of metallurgy*. Taylor & Francis, 2005.
25. S. Katsuhito and M. Yoshimasa: *ISIJ Int.* 2000, vol. 40, pp. 40-47.
26. S. Katsuhito and M. Yoshimasa: *ISIJ Int.* 1996, vol. 36, pp. 388-94.
27. D.C. Park, I.H. Jung, P.C.H. Rhee, and H.G. Lee: *ISIJ Int.* 2004, vol. 10, pp. 1669-78.
28. H.P. Sun, K. Mori, and R.D. Pehlke: *Metall. Mater. Trans. B* 1993, vol. 24, pp. 113-20.
29. V. Brabie: *ISIJ Int.* 1996, vol. 36, pp. S109-S12.
30. P.C. Yan, M.V. Ende, E. Zinngrebe, V.D.L. Sieger, B. Bart, and M.X Guo: *ISIJ Int.* 2014, vol. 54, pp. 2551-58.
31. N.N Lv, L.S. Wu, H.C. Wang, Y.C. Dong, and C. Su: *J. Iron Steel Res. Int.* 2017, vol. 24, pp. 243-50.
32. H. Goto and K. Miyazawa: *ISIJ Int.* 1998, vol. 38, pp. 256-59.
33. H. Tanaka, R. Nishihara, R. Miura, R. Tsujino, T. Kimura, T. Nishi, and T. Imoto: *ISIJ Int.* 1994, vol. 34, pp. 868-75.
34. J.H. Park and Y.B. Kang: *Steel Res. Int.* 2024, vol. 95, p. 2300598.
35. M. Guo, S. Parada, P.T. Jones, J. V. Dyck, E. Boydens, D. Durinck, B. Blanpain, and P. Wollants: *Ceram. Int.* 2007, vol. 33, pp. 1007-18.
36. Volta Redonda EEIMVR-UFF: 2018.
37. S. K.Michelie and C. Bernhard: *Steel Res. Int.* 2022, vol. 93.
38. H. Zhang, Y.B. Peng, S. Zhang, C.S. Liu, R.J. Cheng, and H.W. Ni: *Metall. Mater. Trans. B* 2022, vol. 53, pp. 702-15.
39. D. Janke, Z.T. Ma, P. Valentin, and A. Heinen: *ISIJ Int.* 2000, vol. 40, pp. 31-39.
40. A. Karasangabo and C. Bernhard: *J. Adhes. Sci. Technol.* 2012, vol. 26, pp. 1141-56.
41. K. Mukai: *ISIJ Int.* 1992, vol. 32, pp. 19-25.
42. L.M. Cheng, L.F. Zhang, Y. Ren, and W. Yang: *Metall. Mater. Trans. B* 2021, vol. 52, pp. 1186-93.
43. R. Salomão, V.L. Ferreira, L.R. Oliveira, A.D. Souza, and W.R. Correr: *J. Eur. Ceram. Soc.* 2016, vol. 36, pp. 4225-35.
44. L.P. Pan, Y.W. Li, F.G. Tan, Q. Wang, Y.C. Chen, Q.H. Wang, T.B. Zhu, N. Liao, and Y.B. Xu: *Ceram. Int.* 2023, vol. 49, pp. 16137-48.

45. M.A. Braulio, G.G. Morbioli, D. H. Milanez, and V. C. Pandolfelli: *Ceram. Int.* 2011, vol. 37, pp. 215-21.
46. A.D. Wilson: In *Proceedings of a symposium of inclusions and their influence on material behavior. Chicago (Illinois): ASM International*, 1988, p 21.
47. J.F. Knott: *Trans. Iron Steel Inst. Jpn.* 1981, vol. 21, pp. 305-17.
48. Y.H. Yu, T. Pan, J.C. Yin, SH. u, and Y. Ma: *Iron Steel* 2013, vol. 48, p. 57.
49. y. Ma Yue, T. Pan, B. Jiang, Y.H. Cui, H. Su, and Y. Peng: *Acta Metall Sin* 2011, vol. 47, pp. 978-83.
50. W.M. Garrison: *Iron Steel Technol.* 2007, vol. 4, p. 132.
51. K.B. Park and K.C. Ludema: *Wear* 1994, vol. 175, pp. 123-31.
52. R.C. Chen, Z.G. Wang, F.S. Zhu, H.J. Zhao, J. Qin, and L.Q. Zhong: *J. Alloys Compd.* 2020, vol. 824, p. 153849.
53. C. Wang, X.G. Liu, J.T. Gui, Z.L. Du, Z.F. Xu, and .F. Guo: *Vacuum* 2020, vol. 174, p. 109209.
54. Y. Song, H.N. Zhang, and L. Ren: *Eng. Rep.* 2024, vol. 6, p. e12892.
55. P.A. Thornton: *J. Mater. Sci.* 1971, vol. 6, pp. 347-56.
56. J. Yang, C. Ling, and J. Tang: *Heat Treat. Met.* 2012, vol. 37, pp. 32-36.
57. Y.X. Li and X. Chen: *Foundry China* 2000, vol. 49, pp. 525-28.
58. L.F. Zhang and Y. Ren: In *Handbook of Non-Metallic Inclusions in Steels*, Springer: 2025, pp 1-35.
59. C. Gu, Y.P. Bao, P. Gan, M. Wang, and J.S. He: *Int. J. Miner., Metall. Mater.* 2018, vol. 25, pp. 623-29.
60. J.M. Zhang, S.X. Li, Z.G. Yang, G.Y. Li, W.J. Hui, and Y.Q. W eng: *Int. J. Fatigue* 2007, vol. 29, pp. 765-71.
61. Y. Higuchi, M. Numata, S. Fukagawa, and K. Shinme: *ISIJ Int.* 1996, vol. 36, pp. S151-S54.
62. Y. Ren, W.J. Wang, W. Yang, and L.F. Zhang: *ISIJ Int.* 2023, vol. 63, pp. 1927-40.
63. H. Ohta and H. Suito: *Metall. Mater. Trans. B* 1997, vol. 28, pp. 1131-39.
64. A. Ghosh: *ISIJ int.* 2008, vol. 48, pp. 1552-59.
65. GM Faulring: and *DC HILTY: Iron Steelmaker* 1980, vol. 7, pp. 14-20.
66. J.H. Liu, H.J. Wu, Y.P. Bao, and M. Wang: *Int. J. Miner., Metall. Mater.* 2011, vol. 18, p. 527.
67. Y. Tabatabaei, K.S. Coley, G.A. Irons, and S. Sun: 2018, vol. 49, pp. 2022-37.
68. Y. Tabatabaei, K.S. Coley, G.A. Irons, and S. Sun: *Metall. Mater. Trans. B* 2018, vol. 49, pp. 375-87.
69. J.A. Geldenhuis and P.C. Pistorius: *Ironmaking Steelmaking* 2000, vol. 27, pp. 442-49.
70. S.F. Yang, L.F. Zhang, L.Y. Sun, J.S. Li, and K.D. Peaslee: *Iron Steel Technol.* 2012, pp. 245-58.
71. G.J.W. Kor: In *Steelmaking Conference Proceedings.*, 1989, pp 39-44.
72. R.V. Väinölä, L.E.K. Holappa, and P.H.J. Karvonen: *J. Mater. Process. Technol* 1995, vol. 53, pp. 453-65.
73. R. Maiti and E.B. Hawbolt: *J. Mater. Energy Syst.* 1985, vol. 6, pp. 251-62.
74. Y. Tomita: *J. Mater. Sci.* 1990, vol. 25, pp. 5179-84.
75. G.Z. Li, F.M. Wang, R. Hui, and W.K. Cao: *Int. J. Miner., Metall. Mater.* 2009, vol. 16, pp. 650-53.
76. J. Moon, S.J. Kim, and C. Lee: *Met. Mater. Int.* 2013, vol. 19, pp. 45-48.

77. L.M. Wang, Qin Q. Lin, J.W. Ji, and D.N. Lan: *J. Alloys Compd.* 2006, vol. 408, pp. 384-86.
78. L.J. Yue, L.M. Wang, and J.S. Han: *J. Rare Earths* 2010, vol. 28, pp. 952-56.
79. D.H. Bao, G.G. Cheng, Y. Huang, T. Qiao, and W.X. Dai: *Steel Res. Int.* 2022, vol. 93, p. 2100304.
80. F. Pan, H.L. Chen, Y.H. Su, and W.S. Hwang: *Sci. Rep.* 2017, vol. 7, p. 2564.
81. W.N. Shi, S.F. Yang, and J.S. Li: *Sci. Rep.* 2018, vol. 8, p. 4830.
82. S.L.A. mirnov, V.A. Rovnushkin, A.B. Dobuzhskaya, G.N. Yunin, and E.V. Polevoi: *Steel in Translation* 2016, vol. 46, pp. 805-13.
83. S.P. Burmasov, A.V. Murzin, L.E. Dresvyankina, V.A. Toporov, and A.G. Gudov: *Metallurgist* 2016, vol. 59, pp. 1068-74.
84. X.K. Cui, B. Song, and J.H. Mao: *Trans. Indian Inst. Met.* 2022, vol. 75, pp. 2221-30.
85. P.C. Lu, H.B. Li, H. Feng, Z.H. Jiang, and Y.B. Dai: *Metall. Mater. Trans. B* 2022, vol. 53, pp. 1920-35.
86. X.Q. Wang, Z.W. Wu, B. Li, W.X. Chen, J. Zhang, and J. Mao: *J. Rare Earths* 2024, vol. 42, pp. 431-45.
87. A. Vahed and D.A.R. Kay: *Metall. Mater. Trans. B* 1975, vol. 6, pp. 285-87.
88. P.E. Waudby: *Inter. Met. Rev.* 1978, vol. 23, pp. 74-98.
89. H. Zhang, Y.B. Peng, S. Zhang, C.S. Liu, . Cheng, and H.W. Ni: *Metall. Mater. Trans. B* 2022, vol. 53, pp. 702-15.
90. H. Suito and R. Inoue: *ISIJ Int.* 1996, vol. 36, pp. 528-36.
91. S.H. Chen, M. Jiang, X.. He, and X.H. Wang: *Int. J. Miner., Metall. Mater.* 2012, vol. 19, pp. 490-98.
92. L.F. Zhang and S. Taniguchi: *Int. Mater. Rev.* 2000, vol. 45, pp. 59-82.
93. J.S. Park and J.H. Park: *Metall. Mater. Trans. B* 2016, vol. 47, pp. 3225-30.
94. S. Sridhar and A. W. Cramb.: *High Temperature Materials and Processes* 2003, vol. 22, pp. 275-82.
95. S.I. Shimasaki, S. Narita, and S. Taniguchi: *Materials Science Forum* 2014, vol. 794-796, pp. 1089-94.
96. R.H. Yoon and G.H. Luttrell: *Miner. Process. Extr. Metall. Rev.* 1989, vol. 5, pp. 101-22.
97. H.L. Yang, P. He, and Y.C. Zhai: *ISIJ Int.* 2014, vol. 54, pp. 578-81.
98. L.F. Zhang, S. Taniguchi, and K. Matsumoto: *Ironmaking Steelmaking* 2013, vol. 29, pp. 326-36.
99. Y.G. Xu, M. Ersson, and P.G. Jönsson: *ISIJ Int.* 2016, vol. 56, pp. 1982-88.
100. H.J. Duan, Y. Ren, and L.F. Zhang: *Metall. Mater. Trans. B* 2018, vol. 50, pp. 16-21.
101. H.J. Duan, P.R. Scheller, Ying Y. Ren, and L.F. Zhang: *JOM* 2018, vol. 71, pp. 69-77.
102. X.P. Guo, J. Godinez, N.J. Walla, A.K. Silaen, H. Oltmann, V. Thapliyal, A. Bhansali, E. Pretorius, and C.Q. Zhou: *Processes* 2021, vol. 9.
103. G.J. Chen and S.P. He: *JOM* 2019, vol. 71, pp. 4206-14.
104. A.V. Nguyen, J. Ralston, and H.J. Schulze: *Int. J. Miner. Process.* 1998, vol. 53, pp. 225-49.
105. L.H. Wang, H.G. Lee, and P. Hayes: *ISIJ Int.* 1996, vol. 36, pp. 7-16.
106. M. Söder, P. Jönsson, and L. Jonsson: *Steel Res. Int.* 2004, vol. 75, pp. 128-38.
107. L.T. Wang, Q.Y. Zhang, S.H. Peng, and Z.B. Li: *ISIJ Int.* 2005, vol. 45, pp. 331-37.
108. K.L. Sutherland: *J. Phys. Chem.* 1948, vol. 52, pp. 394-425.

109. D.Y. Sheng, M. Söder, P. Jönsson, and L. Jonsson: *Scand. J. Metall.* 2002, vol. 31, pp. 134-47.
110. Q. Cao and L.L. Nastac: *Ironmaking Steelmaking* 2018, vol. 45, pp. 984-91.
111. W.T. Lou and M.Y. Zhu: *Metall. Mater. Trans. B* 2013, vol. 44, pp. 762-82.
112. X.L. Guo, J.B. Yu, X.F. Ren, D.H. Xue, W.D. Xuan, Y.B. Zhong, and Z.M. Ren: *Ironmaking Steelmaking* 2018, vol. 45, pp. 648-54.
113. L.F. Zhang and S. Taniguchi: *Int. Mater. Rev.* 2000, vol. 45, pp. 59-82.
114. W. Liu, J. Liu, H.X. Zhao, S.F. Yang, and J.S. Li: *Metall. Mater. Trans. B* 2021, vol. 52, pp. 2430-40.
115. K. Nakajima and K. Okamura: In *Proceedings of the 4th International Conference on Molten Slags and Fluxes, Tokyo, Japan, 1992*.
116. L.I. Krupman, Y.U.G. Yaroslavtsev, V.V. Averin, and K.P. Bziava: *Izv. Akad. Nauk SSSR, Met.* 1977, pp. 21-25.
117. I.I. Bornatskii, L.I. Krupman, B.P. Sinyagovskii, E.N. Shinkarenko, and Y.G. Yaroslavtsev: *Metallurgist* 1967, vol. 11, pp. 483-86.
118. D. Bouris and G. Bergeles: *Metall. Mater. Trans. B* 1998, vol. 29, pp. 641-49.
119. M. Valdez, G.S. Shannon, and S. Sridhar: *ISIJ Int.* 2006, vol. 46, pp. 450-57.
120. J. Strandh, K. Nakajima, R. Eriksson, and P. Jönsson: *ISIJ Int.* 2005, vol. 45, pp. 1838-47.
121. G. Shannon, L. White, and S. Sridhar: *Mater. Sci. Eng.: A* 2008, vol. 495, pp. 310-15.
122. G.N. Shannon and S. Sridhar: *Scand. J. Metall.* 2005, vol. 34, pp. 353-62.
123. S.F. Yang, W. Liu, and J.S. Li: *JOM* 2015, vol. 67, pp. 2993-3001.
124. S.F. Yang, J.S. Li, C. Liu, L.Y. Sun, and H.B. Yang: *Metall. Mater. Trans. B* 2014, vol. 45, pp. 2453-63.
125. C. Liu, S.F. Yang, J.S. Li, L.B. Zhu, and X.G. Li: *Metall. Mater. Trans. B* 2016, vol. 47, pp. 1882-92.
126. C.J. Xuan, E.S. Persson, R. Sevastopolev, and M. Nzotta: *Metall. Mater. Trans. B* 2019, vol. 50, pp. 1957-73.
127. M. Magnelöv, U. Sjöström, and S.C. Du: In *VII International Conference on "Molten Slags Fluxes and Salts". South African: The South African Institute of Mining and Metallurgy*, 2004, pp 577-84.
128. Y.L. Zhou, Z.Y. Deng, and M.Y. Zhu: *Int. J. Miner., Metall. Mater.* 2017, vol. 24, pp. 627-37.
129. P. Misra, V. Chevrier, S. Sridhar, and A.W. Cramb: *Metall. Mater. Trans. B* 2000, vol. 31, p. 1135.
130. B. Coletti, B. Blanpain, S. Vantilt, and S. Sridhar: *Metall. Mater. Trans. B* 2003, vol. 34, pp. 533-38.
131. G. Shannon, Y. Wang, S. Vantilt, B. Coletti, B. Blanpain, and S. Sridhar: In *Proceedings of the VII international conference on molten slags, fluxes and salts*, 2004, pp 571-76.
132. S. Vantilt, B. Coletti, B. Blanpain, J. Fransaer, P. Wollants, and S.S. Sridhar: *ISIJ Int.* 2004, vol. 44, pp. 1-10.
133. J. Wikström, K. Nakajima, H. Shibata, A. Tilliander, and P. Jönsson: *Ironmaking Steelmaking* 2013, vol. 35, pp. 589-99.
134. Y.Z. Huo, H.Z. Gu, A. Huang, B.Y. Ma, L.Y. Chen, G.Q. Li, and Y.W. Li: *J. Iron Steel Res. Int.* 2022, vol. 29, pp. 1711-22.
135. A.G. Martinez M.A. Braulio, A.P. Luz, C. Liebske, V.C. Pandolfelli: *Ceram. Int.* 2011, vol. 37, pp. 1935-45.

136. A.P. Luz, M.A.L. Braulio, A.G. Martinez, and V.C. Pandolfelli: *Ceram. Int.* 2012, vol. 38, pp. 1497-505.
137. E.Y. Sako, M.A.L. Braulio, and V.C. Pandolfelli: *Ceram. Int.* 2012, vol. 38, pp. 4783-89.
138. S. Yilmaz: *Ironmaking Steelmaking* 2013, vol. 33, pp. 151-56.
139. E. Benavidez, E. Brandaleze, L. Musante, and P. Galliano: *Procedia Mater. Sci.* 2015, vol. 8, pp. 228-35.
140. B.Y. Ma, Y. Yin, Q. Zhu, Y.Y. Zhai, Y. Li, G.Q. Li, and J.K. Yu: *Refract. Ind. Ceram.* 2016, vol. 56, pp. 494-501.
141. H.Y. Tang, G.H. Wu, Y. Wang, J.S. Li, P. Lan, and J.Q. Zhang: *Ceram. Int.* 2017, vol. 43, pp. 16502-11.
142. B.Y. Ma, X.M. Ren, Z. Gao, J.L. Tian, Z.H. Jiang, W.Y. Zan, J.K. Yu, F. Qian, Y.N. Cao, and G.F. Fu: *Int. J. Appl. Ceram. Technol.* 2021, vol. 19, pp. 1265-73.
143. Y.S. Zou, H.Z. Gu, A. Huang, L.P. Fu, G.Q. Li, L.W. Wang, and D. Chen: *Ceram. Int.* 2022, vol. 48, pp. 18513-21.
144. J.Y. Choi, H.G. Lee, and J.S. Kim: *ISIJ Int.* 2002, vol. 42, pp. 852-60.
145. P.T. Jones M. Guo, S. Parada, E. Boydens, J.V. Dyck, B. Blanpain, P. Wollants,: *J. Eur. Ceram. Soc.* 2006, vol. 26, pp. 3831-43.
146. S.L. Xiang, X.W. Lv, B. Yu, J. Xu, and J.Q. Yin: *Metall. Mater. Trans. B* 2014, vol. 45, pp. 2106-17.
147. R.R. Wei, X.W. Lv, Z.W. Yue, and S.L. Xiang: *Metall. Mater. Trans. B* 2016, vol. 48, pp. 733-42.
148. B. Yu, X.W. Lv, S.L. Xiang, and J. Xu: *Metall. Mater. Trans. B* 2016, vol. 47, pp. 2063-71.
149. C.W. Andrés, M.N. Moliné, S. Camelli, and A.G.T. Martinez: *Ceram. Int.* 2020, vol. 46, pp. 24495-503.
150. S.H. Hu, A. Huang, Q.L. Jia, S.W. Zhang, and L.G. Chen: *Ceram. Int.* 2021, vol. 47, pp. 11276-84.
151. Y.H. Liang, A. Huang, X.W. Zhu, H.Z. Gu, and L.P. Fu: *Ceram. Int.* 2015, vol. 41, pp. 8149-54.
152. Z.H. Wang, T. Maotsela, P.M. Toperesu, G.M. Kale, J. Daji, and D. Parkinson: *Ceram. Int.* 2019, vol. 45, pp. 725-32.
153. W.Z. Mu and C.J. Xuan: *Ceram. Int.* 2020, vol. 46, pp. 14949-56.
154. J.H. Welch: *J. Sci. Instrum.* 1954, vol. 31, pp. 458-64.
155. Y. Kashiwaya, C.E. Cicutti, A.W. Cramb, and K. Ishii: *ISIJ int.* 1998, vol. 38, pp. 348-56.
156. G. Kim and Y. Chung: *Steel Res. Int.* 2024, vol. 95.
157. J. H. Welch: *Journal of Scientific Instruments* 1954, vol. 31, pp. 458-64.
158. L.J. Zhou, W.L. Wang, F.J. Ma, J. Li, J. Wei, H. Matsuura, and F. Tsukihashi: *Metall. Mater. Trans. B* 2011, vol. 43, pp. 354-62.
159. Y. Kim, Y. Kashiwaya, and Y. Chung: *Ceram. Int.* 2020, vol. 46, pp. 6205-11.
160. F.H. Chen, P. Tang, G.H. Wen, L. Yu, and S.P. Gu: *ISIJ Int.* 2021, vol. 61, pp. 200-08.
161. S. Yeo, H. Um, and Y. Chung: *Metall. Mater. Trans. B* 2021, vol. 52, pp. 3938-45.
162. M. Minsky: *Scanning* 1988, vol. 10, pp. 128-38.
163. W.Z. Mu, P. Hedström, H. Shibata, P.G. Jönsson, and K. Nakajima: *JOM* 2018, vol. 70, pp. 2283-95.
164. S. Niknafs, D. Phelan, and R. Dippenaar: *J. Microsc.* 2013, vol. 249, pp. 53-61.

165. K.W. Yi, C. Tse, J.H. Park, M. Valdez, A.W. Cramb, and S. Sridhar: *Scand. J. Metall.* 2003, vol. 32, pp. 177-84.
166. B. J. Monaghan, L. Chen, and J. Sorbe: *Ironmaking steelmaking* 2005, vol. 32, pp. 258-64.
167. J.H. Park, I.H. Jung, and H.G. Lee: *ISIJ Int.* 2006, vol. 46, pp. 1626-34.
168. J. Liu, M. Guo, P.T. Jones, F. Verhaeghe, B. Blanpain, and P. Wollants: *J. Am. Ceram. Soc.* 2007, vol. 90, pp. 3818-24.
169. K. Y. Miao, A. Haas, M. Sharma, W. Z. Mu, and N. Dogan: *Metall. Mater. Trans. B* 2018, vol. 49, pp. 1612-23.
170. C.J. Xuan and W.Z. Mu: *J. Am. Ceram. Soc.* 2020, vol. 104, pp. 57-75.
171. L. Chen B.J. Monaghan: *J. Non-Cryst. Solids* 2004, vol. 347, pp. 254-61.
172. O. Levenspiel: *Chemical reaction engineering.* John wiley & sons, 1998.
173. S. Sridhar and A.W. Cramb: *Metall. Mater. Trans. B* 2000, vol. 31, pp. 406-10.
174. M. Valdez, K. Prapakorn, A.W. Cramb, and S. Sridhar: *Steel Res. Int.* 2001, vol. 72, pp. 291-97.
175. M. Valdez, K. Prapakorn, A.W. Cramb, and S. Sridhar: *Ironmaking Steelmaking* 2002, vol. 29, pp. 47-52.
176. A.B. Fox, J. Gisby, R.C. Atwood, P. D. Lee, and S. Sridhar: *ISIJ Inter.* 2004, vol. 44, pp. 836-45.
177. B.J. Monaghan and L. Chen: *Steel Res. Int.* 2005, vol. 76, pp. 348-54.
178. F. Verhaeghe, J. Liu, M. Guo, S. Arnout, B. Blanpain, and P. Wollants: *Appl. Phys. Lett.* 2007, vol. 91, p. 124104.
179. S. Michelic, J. Goriupp, S. Feichtinger, Y.B. Kang, C. Bernhard, and J. Schenk: *Steel Res. Int.* 2016, vol. 87, pp. 57-67.
180. C. Ren, L. Zhang, J. Zhang, S. Wu, P. Zhu, and Y. Ren: *Metall. Mater. Trans. B* 2021, vol. 52, pp. 3288-301.
181. C. Ren, C. Huang, L. Zhang, and Y. Ren: *Int. J. Miner., Metall. Mater.* 2023, vol. 30, pp. 345-53.
182. J. Liu, M. Guo, P.T. Jones, F. Verhaeghe, B. Blanpain, and P. Wollants: *J. Eur. Ceram. Soc.* 2007, vol. 27, pp. 1961-72.
183. X.L. Guo, Z.H.I. Sun, J. V.Dyck, M.X. Guo, and B. Blanpain: *Ind. Eng. Chem. Res.* 2014, vol. 53, pp. 6325-33.
184. X.L. Guo, J.V. Dyck, M.X. Guo, and B. Blanpain: *AIChE J.* 2013, vol. 59, pp. 2907-16.
185. B.J. Monaghan and L. Chen: *Ironmaking steelmaking* 2006, vol. 33, pp. 323-30.
186. M. Sharma, W. Mu, and N. Dogan: *JOM* 2018, vol. 70, pp. 1220-24.
187. H.A. Dabkowska M. Sharma, N. Dogan *Steel Res. Int.* 2019, vol. 90, p. 1800367.
188. M. Sharma and N. Dogan: *Metall. Mater. Trans. B* 2020, vol. 51, pp. 570-80.
189. M.J. Whelan: *Met. Sci. J.* 1969, vol. 3, pp. 95-97.
190. H.B. Aaron, D. Fainstein, and G.R. Kotler: *J. Appl. Phys.* 1970, vol. 41, pp. 4404-10.
191. L.C. Brown: *J. Appl. Phys.* 1976, vol. 47, pp. 449-58.
192. F. Verhaeghe, J. Liu, M. Guo, S. Arnout, B. Blanpain, and P. Wollants: *J. Appl. Phys.* 2008, vol. 103, p. 023506.
193. T. Tian, Y. Zhang, H. Zhang, K. Zhang, J. Li, and H. Wang: *Int. J. Appl. Ceram. Technol.* 2019, vol. 16, pp. 1078-87.
194. Y. Ren, P. Zhu, C. Ren, N. Liu, and L. Zhang: *Metall. Mater. Trans. B* 2022, vol. 53, pp. 682-92.

195. S. Feichtinger, S.K. Michelic, Y.B. Kang, and C. Bernhard: *J. Am. Ceram. Soc.* 2014, vol. 97, pp. 316-25.
196. J.J Liu, J. Zou, M.X. Guo, and N. Moelans: *Comput. Mater. Sci.* 2016, vol. 119, pp. 9-18.
197. J. Heulens, B. Blanpain, and N. Moelans: *Acta Mater.* 2011, vol. 59, pp. 2156-65.
198. C.J Xuan and W.Z Mu: *J. Am. Ceram. Soc.* 2019, vol. 102, pp. 6480-97.
199. S.Y. Kwon, R.J. Hill, and I.H. Jung: *Calphad* 2021, vol. 72, pp. 1-8.
200. Sun Yong Kwon, Reghan J. Hill, and In-Ho Jung: *Journal of the American Ceramic Society* 2023, vol. 107, pp. 1835-47.
201. D. Groot, S. Ruurds, and P. Mazur: *Non-equilibrium thermodynamics*. Courier Corporation, 2013.
202. P. Yan, B.A. Webler, P.C. Pistorius, and R.J. Fruehan: *Metall. Mater. Trans. B* 2015, vol. 46, pp. 2414-18.
203. L. C. Zheng, A. Malfliet, B. Q. Yan, Z. H. Jiang, B. Blanpain, and M. X. Guo: *ISIJ Int.* 2022, vol. 62, pp. 1573-85.
204. H.B. Yin, H. Shibata, T. Emiland, and M. Suzuk: *ISIJ Int.* 1997, vol. 37, p. 10.
205. T.F. Deng, J. Gran, and S.C. Du: *Steel Res. Int.* 2010, vol. 81, pp. 347-55.
206. Jin-Hong PARK, In-Ho JUNG, and Hae-Geon LEE: *ISIJ International* 2006, vol. 46, pp. 1626–34.
207. M.O. Temkin: *Acta Phys. Chem., USSR* 1945, vol. 20, pp. 411-23.
208. P. Herasymenko and G.E. Speight: *J. Iron Steel Inst., London* 1950, vol. 166, pp. 169-83.
209. H. Flood and K. Grjotheim: *J. Iron Steel Inst., London* 1952, vol. 171, pp. 64-70.
210. H. Flood, T. Forland, and K. Grjotheim: *Inst. Mi. Met.(London)* 1953, p. 46.
211. J.J. Moore: *Chemical metallurgy*. Elsevier, 2013.
212. C.R. Masson: *Math. Phys. Sci.* 1965, vol. 287, pp. 201-21.
213. C.R. Masson, I.B. Smith, and S.G. Whiteway: *Can. J. Chem.* 1970, vol. 48, pp. 1456-64.
214. N.M. Chuiko: *J. Ferr. Met.* 1959, vol. 5, pp. 3-10.
215. J. Zhang: *The Publishing House of Metallurgical Industry, Beijing* 2007, vol. 245, pp. 32-45.
216. J. Zhang: *Int. J. Miner., Metall. Mater.* 2002, vol. 9, pp. 90-98.
217. J. Zhang: *Acta Metall. Sin. (Engl. Lett.)* 2002, vol. 15, pp. 353-62.
218. D.R. Gaskell: *Metall. Treatises* 1981, vol. 6, pp. 59-78.
219. G. Urbain: *Steel .Res* 1987, vol. 58, pp. 111-16.
220. P.V. Riboud, Y. Roux, D. Lucas, and H. Gaye: *Metallweiterverarb* 1981, vol. 17, pp. 859-66.
221. F.Z. Ji, S.C. Du, and S. Seetharaman: *Metall. Mater. Trans. B* 1997, vol. 28, pp. 827-34.
222. A.D. Pelton and P. Chartrand: *Metall. Mater. Trans. A* 2001, vol. 32, pp. 1355-60.
223. Y. Harada, N. Saito, and K. Nakashima: *Metall. Mater. Trans. B* 2021, vol. 52, pp. 968-77.
224. S. Seshadri, M. Kusuhira, and S.C. Du: *Steel Res. Int.* 2005, vol. 76, pp. 267-78.
225. M. Sajid, C.G. Bai, M. Aamir, Z.X. You, Z.M. Yan, and X X.M. Lv: *ISIJ Int.* 2019, vol. 59, pp. 1153-66.
226. P.V. Riboud and L.D. Lucas: *Can. Metall. Q.* 1981, vol. 20, pp. 199-208.
227. T. Tanaka, K. Hack, T. Iida, and S. Hara: *Zeitschrift für Metallkunde* 1996, vol. 87, pp. 380-89.
228. T. Tanaka, T. Kitamura, and I.A. Back: *ISIJ Int.* 2006, vol. 46, pp. 400-06.

229. J. Wikström, K. Nakajima, L. Jonsson, and P. Jönsson: *Steel Res. Int.* 2008, vol. 79, pp. 826-34.
230. B.J. Monaghan, H. Abdeyazdan, N. Dogan, M.A. Rhamdhani, R.J. Longbottom, and M.W. Chapman: *ISIJ Int.* 2015, vol. 55, pp. 1834-40.
231. V.D. Eisenhüttenleute: *Slag Atlas*. Slag Atlas, 3rd ed., V.D. Eisenhüttenleute, ed., Slag Atlas, 2nd ed., Verlag Stahleisen GmbH, Dusseldorf, 1995.

Chapter 3

In-situ Confocal Microscopy Study of The Dissolution Kinetics of Calcium Aluminate Inclusions in CaO-Al₂O₃-SiO₂ Type Steelmaking Slags

In Chapter 3, all experiments and data analysis were carried out by me. Dr. Muhammad Nabeel provided the training for high temperature confocal laser scanning microscopy and assisted with the slag preparation. Xiaogang Li, Doug Culley and Chris Butcher provided support and training for instruments. Useful discussions on the results were provided by Dr. Neslihan Dogan, Dr. Muhammad Nabeel, Dr. André B. Phillion and Dr. Wangzhong Mu.

The manuscript was initially drafted by me, edited, and revised to the final version by Dr. André B. Phillion, Dr. Muhammad Nabeel, Dr. Neslihan Dogan, and Dr. Wangzhong Mu. This chapter has been published in *Journal of Iron and Steel Research International*, 2025, DOI: <https://doi.org/10.1007/s42243-024-01397-x>. The following chapter is the pre-publication version of this article.

In-situ Confocal Microscopy Study of The Dissolution Kinetics of Calcium Aluminate Inclusions in CaO-Al₂O₃-SiO₂ Type Steelmaking Slags

Guang Wang^{1,*}, Muhammad Nabeel¹, Wang-zhong Mu^{2,3}, A.B. Phillion¹, Neslihan Dogan^{1,4,*}

¹ Department of Materials Science and Engineering, McMaster University, Hamilton L8S4L7, Canada

² Department of Materials Science and Engineering, KTH Royal Institute of Technology, Stockholm 10044, Sweden

³ Engineering Materials, Department of Engineering Science and Mathematics, Luleå University of Technology, Luleå 97187, Sweden

⁴ Department of Materials Science and Engineering, Delft University of Technology, Delft, 2628CD, The Netherlands

Corresponding author: Guang Wang, Neslihan Dogan

* Email: wangg84@mcmaster.ca, n.d.dogan@tudelft.nl

Abstract

Dissolution kinetics of CaO·2Al₂O₃ (CA2) particles in a synthetic CaO-Al₂O₃-SiO₂ steelmaking slag system has been investigated using high-temperature confocal laser scanning microscope (HT-CLSM). Effects of temperatures (i.e., 1500, 1550, and 1600°C) and slag composition on the dissolution time of CA2 particles are investigated, along with the time dependency of the projection area of the particle during the dissolution process. It is found that the dissolution rate was enhanced by either an increase of temperature or a decrease of slag viscosity. Moreover, a higher ratio of CaO/Al₂O₃ (C/A) leads to an increased dissolution rate of CA2 particle at 1600°C. Thermodynamic calculations suggested that the dissolution product, i.e. melilite formed on the surface of the CA2 particle during dissolution in slag with a C/A ratio of 3.8 at 1550°C. Scanning electron microscopy equipped with energy dispersive X-ray spectrometry (SEM-EDS) analysis of as-quenched samples confirmed the dissolution path of CA2 particles in slags with C/A ratios of 1.8 and 3.8 as well as the melilite formed on the surface of CA2 particle. The formation of this layer during the dissolution process was identified as a hindrance, impeding the dissolution

of CA₂ particle. A valuable reference for designing or/and choosing the composition of top slag for clean steel production is provided, especially using calcium treatment during the secondary refining process.

Keywords

In-situ observation; Dissolution kinetics; Confocal laser scanning microscope; Calcium aluminate inclusions; Steelmaking slags; Clean steel

3.1 Introduction

The presence of non-metallic inclusions (NMIs) in steel degrades the final product's mechanical properties, such as tensile strength and corrosion resistance. [1, 2] Moreover, specific types of NMIs can cause some engineering problems, such as clogging of the submerged entry nozzle (SEN) during continuous casting. [3] As a result, it is crucial to minimize the presence of NMIs in steels.

Different approaches have been developed and applied to control and remove NMIs during the secondary steelmaking process. Two common approaches are introduced here. The first one is the modification of NMIs' composition and morphology in liquid steel. A well-known example is the calcium treatment for aluminum killed steel, which modifies the solid alumina inclusions to become liquid or semi-liquid calcium aluminates and changes their shape from irregular to spherical. These modifications significantly reduce the risk of SEN clogging and product defects. [4-6] However, inadequate calcium addition can result in incomplete alteration of alumina inclusions, leading to the creation of undesired solid inclusions like CaO·2Al₂O₃ (CA₂) and CaO·6Al₂O₃ (CA₆). If these compounds form, there is an enhanced risk of blockages within the SEN during continuous casting. The second approach is the removal of NMIs from the liquid steel into the molten slag. The removal of NMIs out of the liquid steel can occur in the ladle, tundish, or continuous caster. Irrespective of the process, removal occurs in three stages: flotation of the inclusion from bulk steel to the steel-slag interface, separation of the inclusion from the steel-slag interface, and dissolution of the inclusion into the steelmaking slag. For the last stage, a rapid dissolution of NMIs is desirable. If the dissolution kinetics of NMIs are insufficient, they may oscillate at the slag interface, elevating the risk of re-entrainment.

Over the past few decades, different approaches have been applied to investigate the dissolution of NMIs in the steelmaking slags, especially temperature is the key parameter to be investigated. [7-9] The most common approach is the so-called rotating finger test, or named rotating cylinder test and rotating dip test. For this method, firstly, an oxide cylinder with a diameter of about 1 cm is inserted into the liquid slag; and secondly, the dissolution kinetics are determined from the reduction in the diameter of the cylinder. While this method has provided much insight into NMI's dissolution, a significant limitation is the substantial difference in size between the immersed oxide cylinder and oxide inclusions that occur during the process. Potentially, the difference raises doubts regarding the applicability of data obtained from centimeter-sized samples to dissolution kinetics at micron-scale dimensions.

High-temperature confocal laser scanning microscope (HT-CLSM) is a robust facility that has been developed in the last two decades and provides an in-situ real-time observation capability for investigating the behavior of micron-size NMIs under conditions relevant to the steelmaking process. Sridhar et al. [10] first reported the dissolution process of alumina inclusion in the molten slag. Since then, several studies have been carried out to study the dissolution of different types of inclusion in molten slags. These studies were primarily directed towards the elucidation of the dissolution mechanisms and kinetics of single-phase NMIs including Al_2O_3 [1, 10-21], MgO [1, 13, 15, 22], CaO [23, 24], and SiO_2 [2, 25, 26], as well as the complex NMIs, MgAl_2O_4 [1, 13, 15, 27] and Al_2TiO_5 [28-30] in the steelmaking slag systems, e.g. $\text{CaO-Al}_2\text{O}_3\text{-SiO}_2$ with or without MgO at high temperature ranging from 1250 to 1630°C. Besides the above mentioned inclusion types, limited information is available in the open literature regarding the dissolution kinetics of calcium aluminate inclusions, e.g., $\text{CaO}\cdot 2\text{Al}_2\text{O}_3$ (CA2) [6] in steelmaking slags. Miao et al. [6] conducted pioneering research on the dissolution of CA2 in two $\text{CaO-Al}_2\text{O}_3\text{-SiO}_2$ type slags at different temperatures. Their findings indicated that mass transfer of the dissolving species within the molten slag is the rate-limiting step for CA2 dissolution. Furthermore, they observed that the dissolution rate of CA2 was enhanced by higher temperatures and lower SiO_2 content in slag. However, the study employed two types of slags with different C/A ($\text{CaO}/\text{Al}_2\text{O}_3$) ratios and SiO_2 contents to study the effect of SiO_2 content on the dissolution rate of CA2 particles. This introduces uncertainty regarding the role of the C/A ratio in accelerating CA2 dissolution. Moreover, the impact of one of the most critical factors, the C/A ratio of the refining slag, affecting the total oxygen in molten steel [31], was not explored in relation to the dissolution kinetics of the CA2

particles. Systematic study of the important process parameters is required for a better understanding of the dissolution kinetics and mechanisms of these complex inclusions for achieving clean steel production during the secondary steelmaking process.

This study fills the above-mentioned knowledge gap by combining in-situ observation of CA2 particle dissolution via HT-CLSM, thermodynamic calculations, and electron microscopy. The effect of temperature and slag properties (C/A) ratio and slag viscosity was quantified. Moreover, the dissolution path of CA2 in two slags at 1550°C was determined.

3.2 Methodology

3.2.1 Materials

Steelmaking type slags were synthesized in the laboratory using high purity (> 99.5%) laboratory-grade powders of CaCO₃, CaO, SiO₂ and Al₂O₃ obtained from Alfa Aesar, USA. The CaO powder was roasted at 1100°C for 12 h under air before use to eliminate moisture and decompose any residual CaCO₃ present in the powder.

3.2.1.1 CA2 particle preparation

For the preparation of CA2 particles, a total of 100 g of CaCO₃ and Al₂O₃ powder in stoichiometric proportions, were prepared. The mixture underwent a mixing process to get the well mixed powder. The details of the mixing process can be found elsewhere. [6] The powder was lightly moistened with approximately 5% distilled water. Approximately 20 g of the dried and moistened powder was compacted into a pellet with a diameter of 2.5 cm and a height of 2 cm. A pressure of 20 MPa was applied for 30 s to ensure proper pellet formation. These pellets were then transferred into an alumina crucible and subjected to sintering in a vertical tube furnace. The sintering process involved heating the pellets at a rate of 10°C/min until reaching 1600°C followed by an isothermal hold for 24 h. Subsequently, the pellets were gradually furnace cooled at 10°C/min to room temperature. Throughout the entire sintering process, argon gas was injected to maintain an inert atmosphere. The sintered pellets were characterized by performing room-temperature powder X-ray Diffraction (XRD) measurements using a PANalytical X'Pert diffraction instrument, which uses a copper source with a wavelength of 1.54056 Å. A Rietveld refinement of the XRD pattern was performed using the FULLPROF suite. As can be seen in **Figure 3.1**, the acquired XRD patterns matched those of the standard reference CA2. [32] Notably, no additional phases were detected, confirming the successful preparation of high-purity CA2.

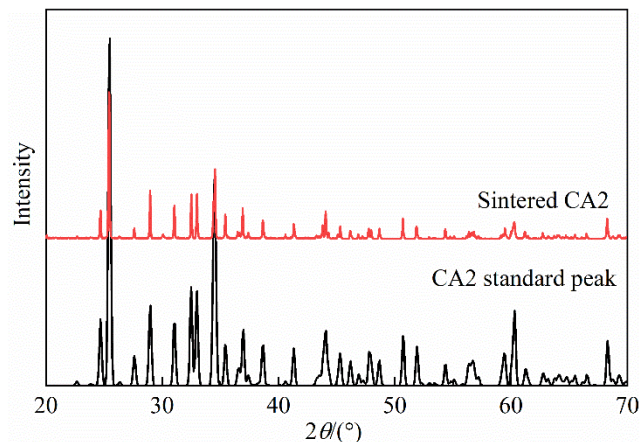


Figure 3.1 XRD patterns of CA2 prepared by sintering at 1600°C for 24 h

3.2.1.2 Slag preparation

Several key factors were considered when designing the slag composition for dissolution experiments using HT-CLSM. First, the slag had to be transparent (or semi-transparent) to enable clear observation of particle dissolution. Second, the liquidus temperature of the slag needed to be lower than that of the inclusions to ensure that the slag was completely liquid and had a homogeneous composition. Finally, slags were designed to provide different C/A ratios and different SiO₂ content. CaO and Al₂O₃ were included to enhance the wettability of the slag with inclusions, while SiO₂ supported the transparency of the slag. Transition-metal oxides such as FeO and CrOx were avoided as they increase the opacity of the slag.

The preparation of slag samples involved mixing powder of CaO, SiO₂, and Al₂O₃ in stoichiometric amounts and heating them to the target temperature, i.e., 50°C higher than the theoretical liquidus temperature of the slag. This mixture was fully melted in a platinum crucible placed in a box furnace and then held isothermally for 4 h to ensure homogenization. Post-preparation, the composition of slag was confirmed by inductively coupled plasma optical emission spectroscopy (ICP-OES).

Five different slags were prepared, with the composition shown in **Table 3.1**. Slag C/A_1, C/A_2, and C/A_4 had a similar SiO₂ content but different C/A ratios to study the effect of C/A ratio on CA2 dissolution kinetics; Slag S50, S40, and S10 had a similar C/A ratio and but different SiO₂ content. These were fabricated to investigate the effect of slag viscosity on CA2 dissolution kinetics. The influence of temperature on the dissolution of CA2 particles was conducted in slag

C/A_1. Please note that slag C/A_2 and S40 are identical. The different nomenclature is used in order to facilitate the discussion of experimental results.

Table 3.1 Slag composition and experimental temperatures

Slags	Composition/wt.%			C/A	<i>T</i> /°C
	CaO	Al ₂ O ₃	SiO ₂		
C/A_1	29	32	39	0.9	1500, 1550, 1600
C/A_2	38	21	41	1.8	1550, 1600
C/A_4	49	13	38	3.8	1550, 1600
S50	33	18	49	1.8	1550
S40	38	21	41	1.8	1550
S10	52	38	10	1.5	1550

3.2.2 In-situ observation experiments

An HT-CLSM (VL2000DX-SVF17SP, Yonekura) was employed to perform the dissolution experiments on the CA₂ particles while making continuous in-situ observations. The technical details of the HT-CLSM facility and operation procedure can be found elsewhere. [33] The experiment was conducted as follows. Firstly, approximately 0.15 g of slag was pre-melted in a Pt crucible of 5 mm in diameter and 6 mm in height within the high temperature furnace via fast heating and cooling. Secondly, a CA₂ particle was placed on the top of the pre-melted slag. Third, the CA₂-slag assembly was heated to the test temperature following a specified heating profile. Finally, the dissolution process was recorded via HT-CLSM at a frame rate of 10 Hz. To avoid changing the composition of the slag, the mass of the CA₂ particle was kept very small, and less than 0.1% of the pre-melted slag.

Figure 3.2 illustrates the entire sample assembly. As can be seen, the Pt crucible, slag, and the CA₂ particle were positioned within an alumina crucible, and on top of a sample holder. A B-type thermocouple, sheathed in an alumina tube, was affixed to the base of the sample holder to measure temperature. This setup resulted in a temperature gradient between the slag surface and the bottom of the alumina crucible; temperature calibration was performed by using a pure iron disc 5 mm in diameter and 2 mm in height. This revealed a temperature difference of around + 17°C between the surface of the iron disc and the thermocouple. It should be noted that the molten slag wetted

the Pt crucible and showed a concave surface; however, this does not affect the observation of the dissolution process.

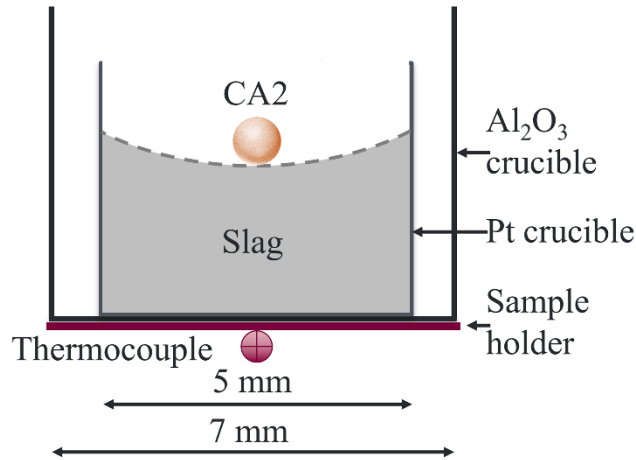


Figure 3.2 Sample holder assembly used in high temperature furnace

Each test followed the same thermal profile, as shown in **Fig. 3.3**. A rapid heating rate of 1000 °C/min was used to elevate the sample temperature to a value of 50°C lower than each testing temperature. Subsequently, a lower heating rate of 50°C/min was used to heat the sample to the testing temperature. This approach served to mitigate the premature dissolution of CA2 particles without overheating past the desired temperature. To ensure experimental repeatability, the dissolution experiments conducted in slag C/A_1 at 1550°C were repeated 4 times. Note that the onset time of CA2 dissolution, t_0 , was defined as the moment the particle was fully immersed in the molten slag after reaching the testing temperature. Furthermore, the dissolution path of the CA2 particles in slag C/A_2 and C/A_4 at 1550°C was interrupted after 90 and 70 s dissolution by quenching the system using helium with a cooling rate at 2000°C/min, respectively. After the experiments were completed, SEM-EDS microanalysis was performed on the two quenched samples using a JEOL6610LV. Thermodynamic calculations were carried out using FactSage 8.0. [34] These calculations included generation of ternary phase diagram, and the determination of slag viscosity using the FToxid databases.

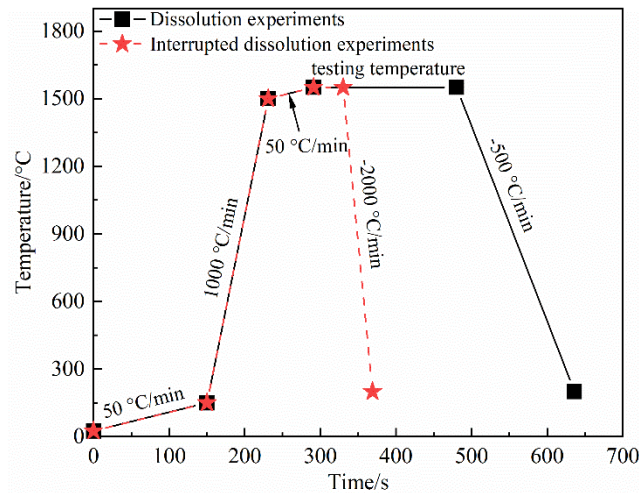


Figure 3.3 Thermal cycle for dissolution and interrupted experiments

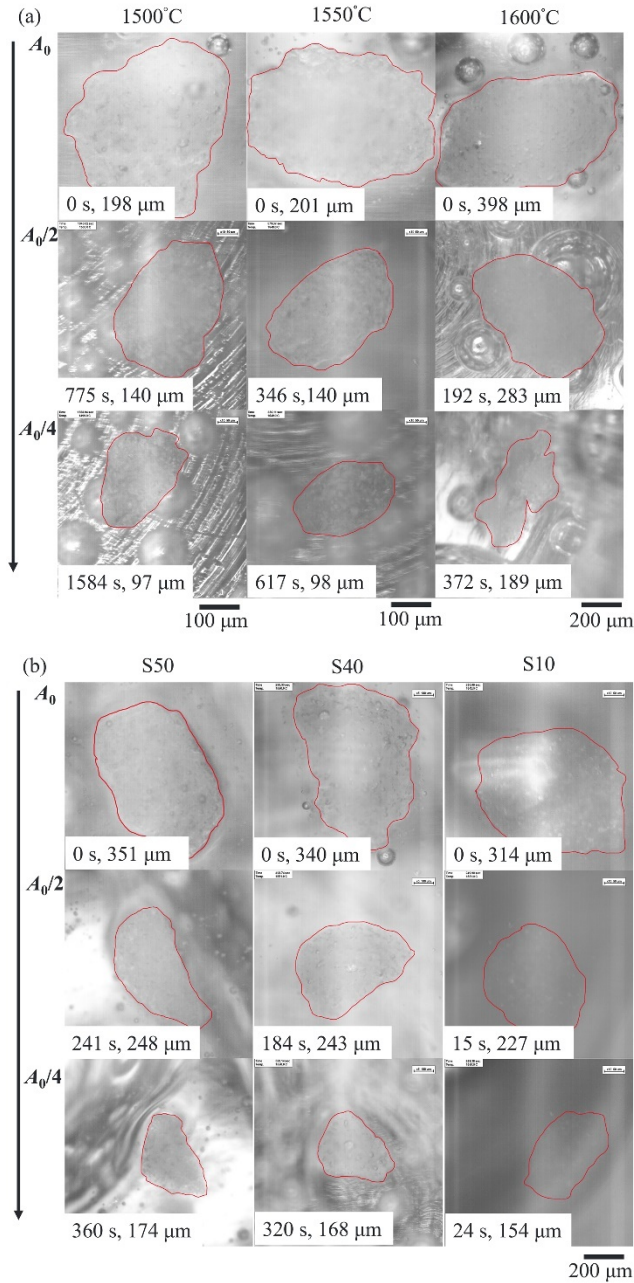
3.3 Results and discussion

3.3.1 In-situ observations experiments

In-situ images taken from the CCD camera are used for the evolution of the cross-section area of a CA2 particle. It is critical that the chosen images focus on the same surface of the CA2 particle throughout any one dissolution experiment. The area measurements were conducted using the commercial software ImageJ. [35] To minimize manual error, each image's measurement was repeated three times, and the average value was calculated. Note that the measurements represent the 2D projection area from the view observable via HT-CLSM.

Fig. 3.4 provides a sequence of images showing the dissolution process of CA2 in the C/A_1 at 1500, 1550, and 1600°C, in slags with different viscosities at 1550°C, and in slags with different C/A ratios at 1600°C. Each image within the figure depicts the CA2 particle positioned centrally, with the red line denoting the CA2 particle – slag boundary. The initial area of the CA2 particle at t_0 is denoted as A_0 . Across all three series of experiments, a continuous reduction in area with time is observed, with no discernible product layer evident on the surface of the CA2 particle. The equivalent radius (r) of CA2 was calculated according to the area assuming CA2 is spherical. As shown in **Fig. 3.4(a)**, the dissolution time at high temperatures is much shorter than at low temperatures. Further, as shown in **Fig. 3.4(b)**, a decrease in slag viscosity enhances the dissolution time reduction. Note that semi-transparent S10, owing to its low SiO₂ content, results in a less distinct boundary line between CA2 particles compared to other slags. Finally, as shown in **Fig. 3.4(c)** a higher C/A ratio slag qualitatively correlates with a decreased dissolution time. It is

interesting to observe that the CA2 particle in slag C/A_2 progressively became transparent during dissolution. This phenomenon could potentially be attributed to the faster transport of Ca^{2+} cations compared to AlO_x^{y-} anions in the molten slag. [36] A similar phenomenon was also observed by Liu et al. [22] for the dissolution of a MgO particle in the ternary CaO-Al₂O₃-SiO₂ slag at 1600°C.



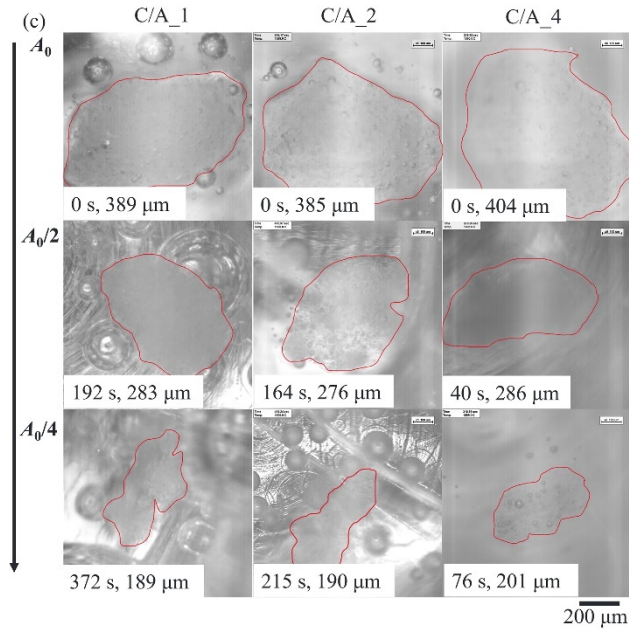


Figure 3.4 A sequence of images showing dissolution process of CA2. (a) In slag C/A_1 at 1500, 1550 and 1600°C; (b) in slag with different viscosities at 1550°C; (c) in slag with different C/A ratios at 1600°C. s—Dissolution time of particle; μm —equivalent radius of particle

In addition to dissolution, the CA2 particles are observed to rotate, move, and dissociate during experimentation. **Fig. 3.5** shows one such process, the dissociation of CA2 particle in slag C/A_1 at 1550°C after 846 s of dissolution. At that time, several tiny particles began to detach and move away from the primary particle, as shown in **Fig. 3.5(b)**. Then, all particles continued to dissolve in the molten slag, with the small particles disappearing first due to their smaller size. Since the dissolution rate of NMIs is proportional to their contact area with the molten slag, [37, 38] the dissociation of CA2 particles would augment the contact area, leading to a higher dissolution rate. To mitigate the influence of dissociation on the dissolution kinetics, data after CA2 dissociation was excluded from the original dataset in all experiments. This approach enabled isolating the effects of dissociation and ensured a more accurate assessment of dissolution kinetics.

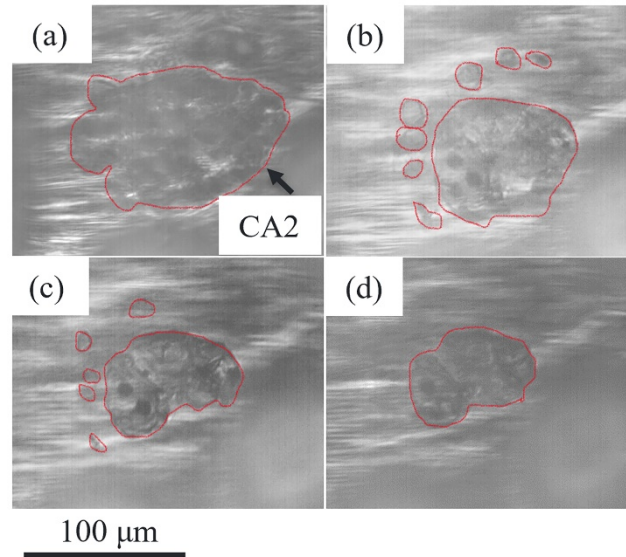


Figure 3.5 Dissociation of a particle during dissolution in slag C/A_1 at 1550°C. (a) 846 s; (b) 876 s; (c) 897 s; (d) 917 s

3.3.2 Effect of temperature on dissolution time of CA2 particle

In **Fig. 3.6**, the normalized area changes with the time of a CA2 particle in the slag C/A_1 at three distinct temperatures are compared. The dissolution time from A_0 to $A_0/4$ significantly decreased from around 1560 to 617, and to 370 s as the temperature increased from 1500 to 1550°C, and further to 1600°C. The influence of temperature on the dissolution time of particles can be elucidated from both thermodynamic and kinetic perspectives. [14, 16, 17, 20, 23, 24] Thermodynamically, assuming local equilibrium at the particle/slag interface, the driving force for particle dissolution is related to the concentration difference (ΔC) of dissolving species between the particle-slag interface and the bulk of the slag. The former can be evaluated from the phase diagram, given by the saturation limit. The temperature significantly impacts the dissolution rate of particles by changing this driving force; generally, an increase in temperature augments the saturation concentration of the particle. In the present study, it is assumed that the driving force for CA2 particle dissolution was the concentration difference between the bulk slag and the saturation content for Al_2O_3 ($\Delta C_{\text{Al}_2\text{O}_3}$). This assumption is grounded in the fact that the size of the Ca^{2+} cation is smaller than that of the AlO_x^{y-} anion and the diffusion coefficient of Ca^{2+} cation is considerably higher than that of AlO_x^{y-} anion. [36] The $\Delta C_{\text{Al}_2\text{O}_3}$ increased from 458 kg/m³ (13 wt.%) to 867 kg/m³ (25 wt.%) with an increase in temperature from 1500 to 1600°C. Additionally, the activity

of the dissolving component at the particle-slag interface and in the bulk slag can influence the dissolution time as well. [2] In this study, the activity of Al_2O_3 at the particle-slag interface is used as the activity of the reactant Al_2O_3 rather than that in the solid CA2. Using FactSage 8.0 with the FToxid databases, [34] the activities of Al_2O_3 in slag C/A_1 at 1500, 1550, and 1600°C were calculated to be 1.47×10^{-1} , 1.76×10^{-1} , 2.07×10^{-1} at the particle-slag interface, and 7.11×10^{-2} , 7.43×10^{-2} , and 7.74×10^{-2} in the bulk slag, respectively. These results indicate that the difference in Al_2O_3 activity between the particle-slag interface and bulk slag increases as the temperature rises. The increase in this difference results in improved mobility of the AlO_x^{y-} anion within the molten slag, thereby reducing the overall dissolution time.

From the kinetic perspective, temperature changes will also strongly affect the rate of chemical reaction and/or boundary layer diffusion. For a first-order chemical reaction, the rate of particle dissolution is given by:

$$J = k * C_1 \quad (1)$$

where J is the molar flux of particle per unit area; k is a rate constant; and C_1 is the concentration difference of the dissolving species between solid oxide and bulk slag. For boundary layer diffusion, Fick's first law can be applied to the diffusion across the boundary layer. In this case, the rate of particle dissolution is given by:

$$J = -D * \frac{C_2}{\delta} \quad (2)$$

where D is the diffusion coefficient of dissolving species; and C_2 is the concentration difference of the dissolving specie between the inside and outside of the boundary layer with thickness δ . An Arrhenius relation describes the temperature dependency of both k and D : [14]

$$k = k_0 * e^{-E_{a1}/(RT)} \quad (3)$$

$$D = D_0 * e^{-E_{a2}/(RT)} \quad (4)$$

where k_0 and D_0 are constants; E_{a1} and E_{a2} are activation energies; R is the universal gas constant; and T is the absolute temperature. It is clear from Eqs. (3) and (4) that k and D increase with increasing temperature and therefore so does J , and by extension the dissolution rate. In addition to the change in driving force, viscosity impacts the dissolution rate as well. By increasing the temperature from 1500 to 1600°C, the slag viscosity was calculated to decrease from 3.12 to 1.32 Pa·s. The elevated $\Delta C_{\text{Al}_2\text{O}_3}$ and activity difference, and reduced viscosity are conducive to accelerate the transport of AlO_x^{y-} from the CA2 – slag interface to the bulk slag. [2, 6, 20]

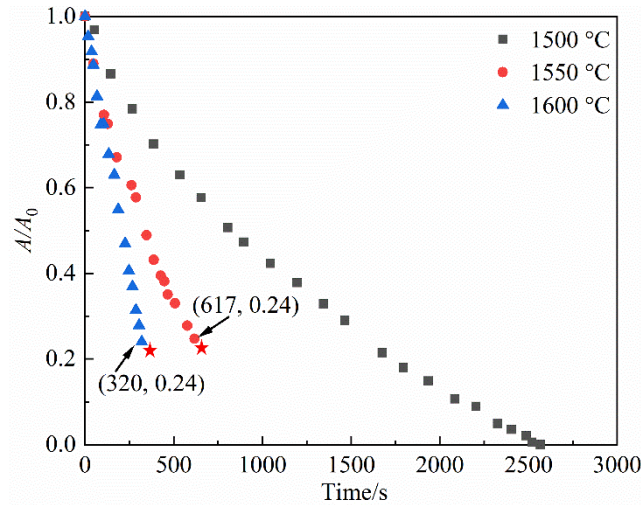


Figure 3.6 Evolution in normalized area of a CA2 particle with time in slag C/A_1 as a function of temperature. Star symbol—Moment when particle dissociation happened, and data after that point is not collected

3.3.3 Effect of slag viscosity on dissolution time of CA2 particle

As shown in **Fig. 3.7**, the total dissolution time of the CA2 particle at 1550 °C exhibited a slight decrease from 800 to 650 s as the viscosity of the slag decreased from 1.35 Pa·s (S50) to 0.63 Pa·s (S40). A further reduction in the slag viscosity to 0.17 Pa·s (S10) resulted in a substantial drop in the total dissolution time to 37 s. The change in dissolution time could be a result of two phenomena: the concentration difference of the dissolving species between the particle-slag interface and the bulk of the slag since each of these slags has a different composition, or the underlying slag structure which directly controls the viscosity (along with slag composition and temperature).

Examining the first phenomenon, it can be seen that the decrease of $\Delta C_{Al_2O_3}$ in kg/m^3 from S50 (1481 kg/m^3 , 32 wt.%) to S40 (887 kg/m^3 , 26 wt.%) is much larger than the decrease from S40 to S10 (801 kg/m^3 , 22 wt.%). This trend is opposite to what was observed for the total dissolution time, and thus, the decrease in the total dissolution time is not so much affected by the change of $\Delta C_{Al_2O_3}$. Miao et al. [6] also reported that the total dissolution time for CA2 in CaO- Al_2O_3 -SiO₂ slag with 5.5 wt.% SiO₂ content was shorter than that in a slag with 46.3% SiO₂ content at the same temperature, despite the $\Delta C_{Al_2O_3}$ being lower in the 5.5 wt.% SiO₂ slag.

Examining the second phenomenon requires a short review of slag structure. One approach is to analyze slag structure through polymer-based and structure-based theories, [39] where the slag

structure is affected by the content of different oxides present in the slag as they strongly affect the degree of polymerization. SiO₂ is an “acid oxide”, and forms an intricate three-dimensional network of anion complexes, whereas CaO is a “basic oxide”, and disrupts the three-dimensional networks formed from the SiO₂ oxides. Finally, Al₂O₃ is classified as an “amphoteric oxide” which does not have any distinctive nature. The higher content of network formers, SiO₂ in S50 and S40, significantly surpasses that of S10, while the content of network breakers, like CaO, in S50 and S40 is lower than that in S10. As a result, the presence of complex three-dimensional networks in S10 was comparatively reduced, resulting in making it easier for species to transport away from the interface in S10 as compared to in S40 and S50. This reduced resistance facilitates faster dissolution of a CA₂ particle in S10. The degree of polymerization can be quantified using the Q parameter, which in the CaO-Al₂O₃-SiO₂ slag system is determined via: [36]

$$Q = 4 - NBO/X_T \quad (5)$$

$$NBO = 2 (X_{CaO} - 2X_{Al_2O_3}) \quad (6)$$

$$X_T = X_{SiO_2} + 2X_{Al_2O_3} \quad (7)$$

where NBO is the number of non-bridge oxygen atoms; X_T is the number of tetragonally-coordinated atoms; and X_i is the molar ratio of component i in the slag. A higher Q indicates a greater degree of polymerization of the molten slag and consequently, reduced mobility of dissolving species within the slag. The Q value for S10 is 2.7, contrasting with 3.3 for S50 and 3.2 for S40. This disparity potentially enhances the transport of AlO_x^{y-} anions from the CA₂ particle-slag interface to the bulk slag, thereby significantly accelerating the dissolution process in S10 as compared to that in S40 and S50. Therefore, similar Q values would result in close dissolution profiles of S50 and S40. Moreover, as discussed in [40], Q values between 3 to 4 result in a slag structural unit known as “sheet” whereas slag with Q values between 2 to 3 have a structural unit known as “chain”. As a result, the significant decrease in total dissolution time from S40 to S10 slags is primarily affected by the change in slag structure. Finally, it should also be noted that the particle in the S10 experiment was observed to be rotating much faster than the particles in the S40 and S50 experiments. This could also have affected the dissolution time.

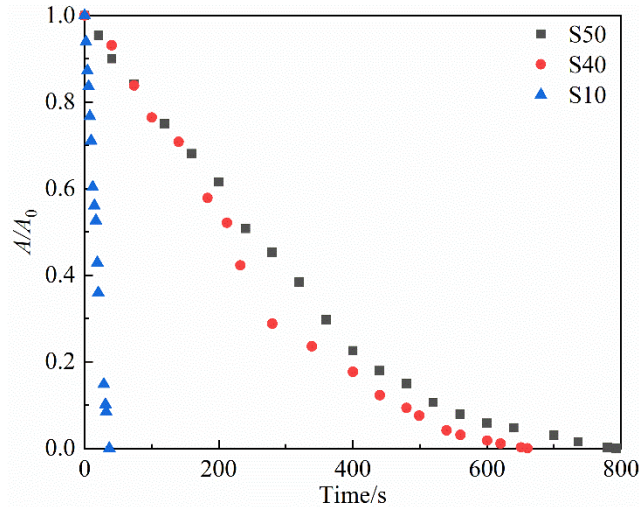


Figure 3.7 Evolution in normalized area of a CA₂ particle with time at 1550 °C in slags with different SiO₂ contents and different viscosities

3.3.4 Effect of C/A ratio on dissolution time of CA₂ particles

The effect of the C/A ratio on the dissolution of CA₂ particles was investigated in three slags having C/A ratios of 0.9, 1.8, and 3.8, each possessing similar SiO₂ content (~ 40 wt.%) at 1600 and 1550°C, respectively. **Fig. 3.8(a)** illustrates the normalized area change of CA₂ particles with time at 1600°C. As can be seen, the dissolution time from A_0 to $A_0/4$ of CA₂ at 1600°C decreased from around 315 to 81 s by increasing the C/A ratio from 0.9 to 3.8. This decrease in dissolution time can be attributed to the continuous decrease in slag viscosity from 1.32 to 0.17 Pa·s, coupled with an increase in the $\Delta C_{Al_2O_3}$ from 867 kg/m³ (25 wt.%) to 1271 kg/m³ (40 wt.%) as the C/A ratio increased from 0.9 to 3.8. Both factors, low viscosity, and high driving force, enhanced the dissolution of the CA₂, resulting in a shortened dissolution time. **Fig. 3.8(b)** depicts the normalized area change with time in slags with different C/A ratios at 1550°C. Initially, the dissolution time A_0 to $A_0/4$ of CA₂ particle decreased from 617 to 340 s with an increase in C/A ratio from 0.9 to 1.8. This decrease can be attributed to a reduction in slag viscosity from 2.00 to 0.63 Pa·s, coupled with an increase in $\Delta C_{Al_2O_3}$ from 606 kg/m³ (18 wt.%) to 887 kg/m³ (26 wt.%). These factors collectively promote the dissolution of the CA₂ particle. However, with a further increase in the C/A ratio to 3.8, the dissolution time unexpectedly increased to 710 s. At this C/A ratio, the viscosity was further decreased to 0.22 Pa·s, and the $\Delta C_{Al_2O_3}$ dropped to 372 kg/m³ (26 wt.%). This unexpected behavior suggests that factors beyond $\Delta C_{Al_2O_3}$ and slag viscosity may influence the dissolution kinetics of the CA₂ particle at higher C/A ratios.

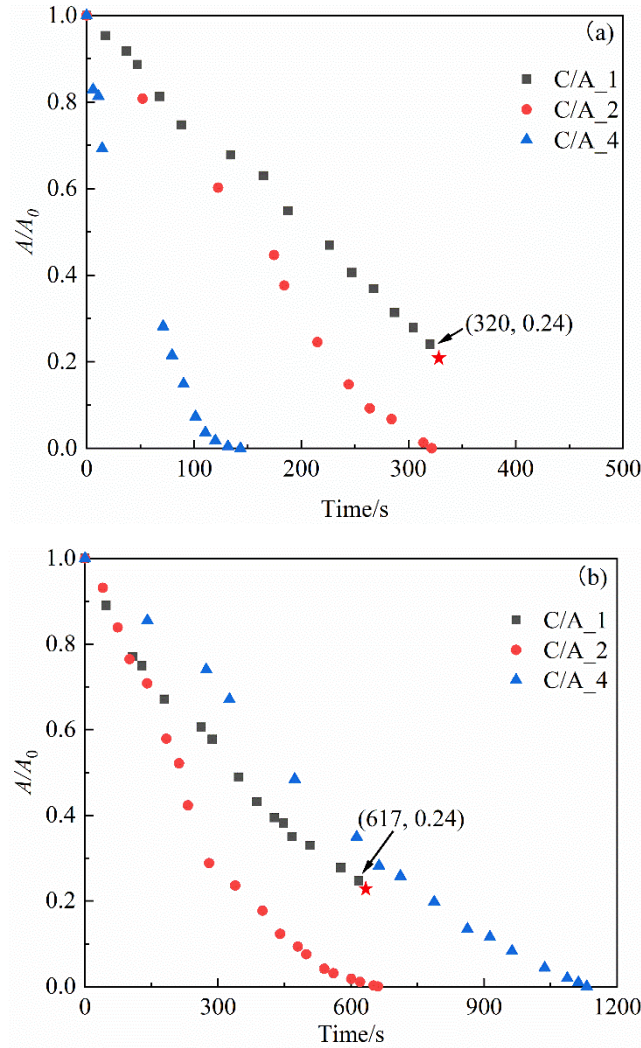


Figure 3.8 Evolution of normalized area of a CA2 particle with time as a function of slag C/A ratio at 1600 (a) and 1550°C (b). Star symbol—Moment when particle dissociation happened, and data after that point is not collected

To gain increased insight into the effects of the C/A ratio on the dissolution of CA2 at 1550°C, the stable phases potentially present in the CA2, SiO₂-Al₂O₃-CaO system at this temperature were calculated using FactSage 8.0 with FToxid database. [34] **Fig. 3.9** shows the relevant ternary diagram, marked with the composition of CA2, and the initial compositions of slags C/A_1, C/A_2, and C/A_4, as well as black solid lines denoting the two-phase tie lines, dashed lines denoting the expected dissolution paths of CA2 in the three slags, and the melilite and CA6 solid phase regions. Although the dissolution is inherently a non-equilibrium process and the dissolution path does not have to be a straight line, the phase diagrams allow for the prediction of phases that may precipitate

adjacent to the CA2 particle.

As can be seen in **Fig. 3.9**, at 1550°C, the composition of all three slags was situated within the fully liquid region. However, the expected dissolution path for slag C/A_1 comes very close to the solid CA6 phase boundary, while the dissolution path for slag C/A_4 crosses through the solid melilite phase boundary. Thus, the formation of intermediate solid products during the dissolution process, especially for C/A_4, is anticipated. Generally, the formation of an intermediate solid phase on the surface of a solid particle can impede the dissolution of particles by decreasing the transport rate of products from and reactants to the particle surface. [23] In extreme cases, solid products may halt the dissolution if they are densely packed on the particle surface and do not dissolve into the bulk slag. It would appear that the formation of a solid layer on the surface of the CA2 particle during its dissolution in slag C/A_4 at 1550°C, which could have contributed to the observed prolonged dissolution time.

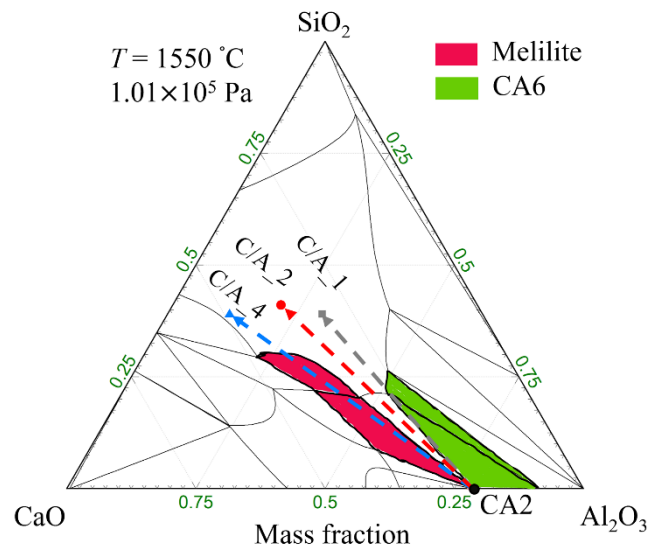


Figure 3.9 Prediction of phase stability of CA2 particle-slag system with FactSage 8.0 [34] at 1550°C

3.3.5 Determination of dissolution path

To gain deeper insights into the dissolution path of a CA2 particle in slag C/A_2 and slag C/A_4, SEM-EDS line scan analysis was conducted along the CA2 particle/slag interface and combined with FactSage thermodynamic calculations. The results are shown in **Figs. 3.10–3.12**. In order to interpret the line scan information with respect to the dissolution path, a mechanism for

distinguishing the CA2 particle, slag C/A_2, slag CA_4, and melilite must be identified. As shown in **Table 3.2**, each of these compounds has a distinct elemental composition. Thus, in the CA2 particle-slag C/A_2 system, regions at the particle/slag interface that lack Si can be classified as CA2, while regions where Ca, Al, and Si stably coexist can be labeled as slag C/A_2. Boundary layers are regions having a decreasing Ca and Si composition while the Al content steadily increases. Similarly, in the CA2 particle – C/A_4 slag system, the non-Si regions at the particle/slag interface can be designated as CA2, while regions where Ca, Al, and Si coexist, with Al and Si constituting ~20 and ~10 wt.%, can be identified as melilite. All other regions can be classified as slag C/A_4.

Fig. 3.10 displays the SEM back scattered electron image, and the elements Ca, Al, and Si distribution obtained from the EDS line scan of the CA2 particle, C/A_2 slag interface after 90 s of dissolution at 1550°C. Following the defined criteria, different regions were identified. The dark-colored middle region in the SEM image represents CA2. An outer layer around the CA2 particle was determined to be the boundary layer, with a thickness of 230 to 240 μm. The C/A_2 slag region followed the boundary layer. Moreover, a visible color difference between the slag and the boundary layer was evident in the SEM image. The presence of a boundary layer confirmed that the assumption of the rate determining step for the dissolution process is the mass transfer of AlO_x^{y-} anion in the slag phase. Note that fluctuations in element concentration, especially within the CA2 particle itself, result from slag penetration into the CA2 particle through its pores.

Fig. 3.11 shows the SEM back scattered electron image and the elements Ca, Al, Si distribution by EDS line scan of CA2 particle, C/A_4 slag interface after 70 s of dissolution at 1550°C. As can be seen, there is the CA2 particle in the central region, followed by a layer of melilite 105 – 111 μm in thickness, and then a boundary layer of about 115 μm.

Fig. 3.12 shows the dissolution paths of CA2 in slag C/A_2 (circle symbol) and slag C/A_4 (triangle symbol) at 1550°C. The data points donated by circle and triangle symbols were taken from the EDS results for both slag systems at different regions along the scanned line. The dashed lines in **Fig. 3.12** donate the theoretical dissolution paths for CA2 in these two slags. It is evident that the prolonged dissolution of CA2 in slag C/A_4 compared to slag C/A_2 at 1550°C is attributed to the formation of the solid melilite phase on the surface of the CA2 particle. The same reaction product melilite for Al_2O_3 dissolution at 1550°C was also reported by Park et al. [41] in a

ternary 53CaO-5Al₂O₃-42SiO₂ (wt.%) slag and by Sandhage et al. [42] in a quaternary 27CaO-21Al₂O₃-42SiO₂-10MgO (wt.%) slag, which retarded the dissolution of Al₂O₃.

Table 3.2 Elemental composition of CA2 particle, slag C/A_2, slag CA_4 and melilite at 1550°C (wt.%)

Composition	Ca	Al	Si
CA2	15	42	0
C/A_2	27	11	19
C/A_4	34	7	17
Melilite	29	20	10

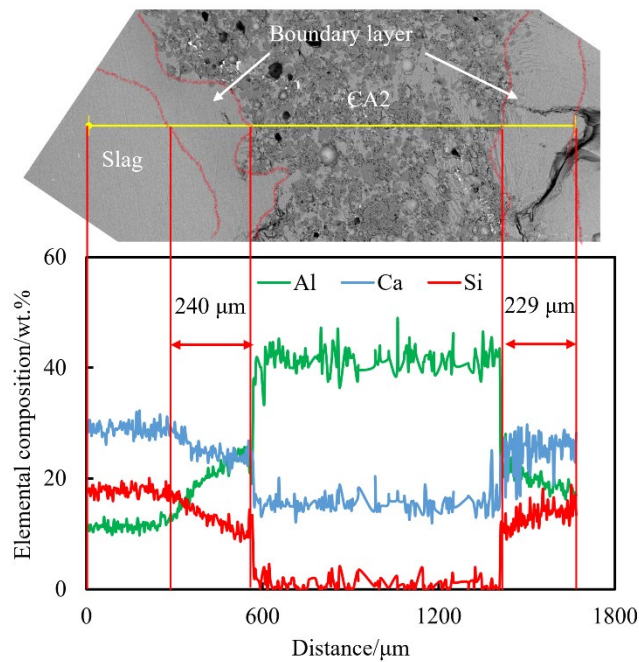


Figure 3.10 SEM back scattered electron image and EDS line scan analysis of CA2 particle - CA_2 slag interface after 90 s dissolution at 1550°C

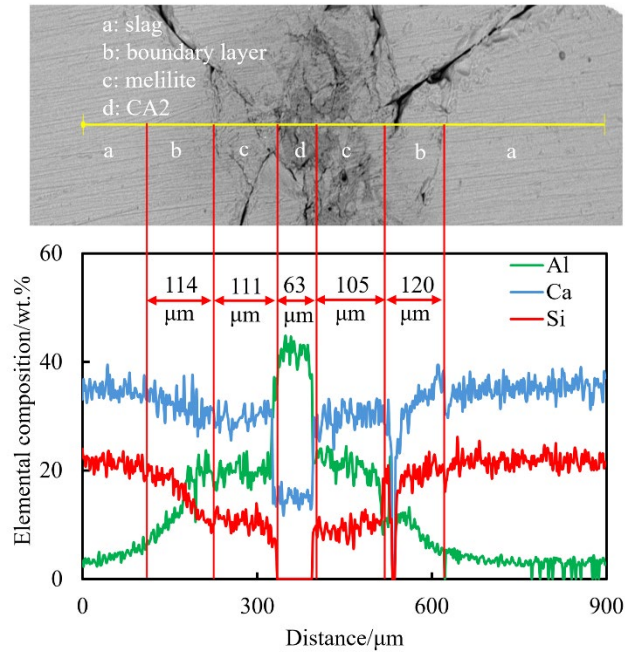


Figure 3.11 SEM back scattered electron image and EDS line scan analysis of CA2 particle, CA_4 slag interface after 70 s dissolution

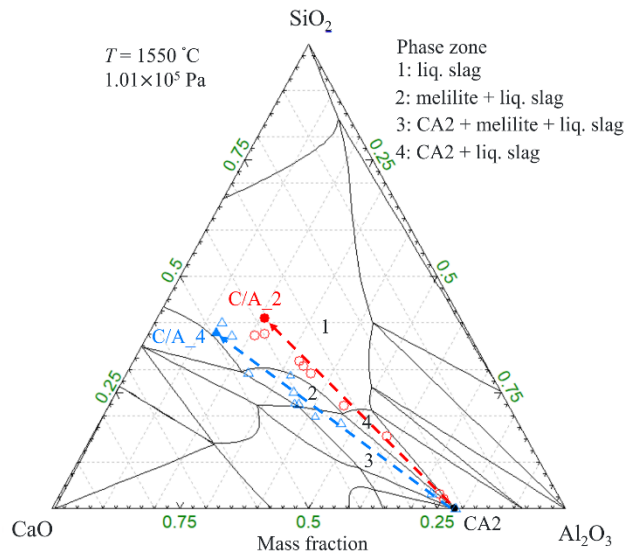


Figure 3.12 Dissolution paths of CA2 in slag C/A_2 and slag C/A_4 at 1550°C. Circle—EDS line scan results; triangle dash line—thermodynamic calculation results

3.3.6 Comparison with literature data and practical consideration

The dissolution kinetics between Al_2O_3 and CA2 particles from the literature and current study were compared since the assumption is that the driving force for CA2 particle dissolution is the

concentration difference between the bulk slag and the saturation content for Al_2O_3 ($\Delta C_{\text{Al}_2\text{O}_3}$), which is the same as that for Al_2O_3 dissolution. **Fig. 3.13** illustrates the average area reduction rate, $\Delta A/\tau$, change as a function of the dissolution factor, $(\Delta C_{\text{Al}_2\text{O}_3})/\mu$. ΔA is area change of CA2 during the dissolution time, τ , before dissociation happens in comparison with the A_0 . As can be seen at low $(\Delta C_{\text{Al}_2\text{O}_3})/\mu$ value (< 1000), the difference of $\Delta A/\tau$ between Al_2O_3 and CA2 particles is small, and it becomes noticeable when $(\Delta C_{\text{Al}_2\text{O}_3})/\mu$ value is higher than 1000. This difference in the $\Delta A_0/\tau$ may be due to 1) the greater porosity of lab produced CA2 particles compared to commercially available dense Al_2O_3 particles; 2) the faster dissolution of CaO in CA2 particles, which exposes more Al_2O_3 surface to the liquid slag, increasing the contact area between CA2 particle and molten slag. Moreover, the dissolved CaO from CA2 particles can act as a network breaker, enhancing the mobility of molten slag in a local regime around CA2 particle.

In the present dissolution experiments, CA2 particles were only immersed and dissolved into the molten slag under natural convection without any additional forces. In practical applications, the inclusion dissolution typically occurs at the molten steel/top slags interface during the steel refining process, at the steel/tundish slags interface, as well as at the steel/mold fluxes interface during casting, conditions that more closely resemble natural convection. When the melilite phase forms an out layer around the CA2 particle, the CA2 dissolution rate is slower than in other cases at the same temperature. The authors believe that the experimental conditions in this study are relevant to the industrial conditions and the findings offer a valuable reference for designing or/and choosing the composition of top slag, tundish slag, and mold fluxes. This is particularly for Al-killed steel with Ca-treatment, where the calcium is fed into molten steel in the final minutes during the secondary steelmaking, necessitating rapid inclusion dissolution by the top slag.

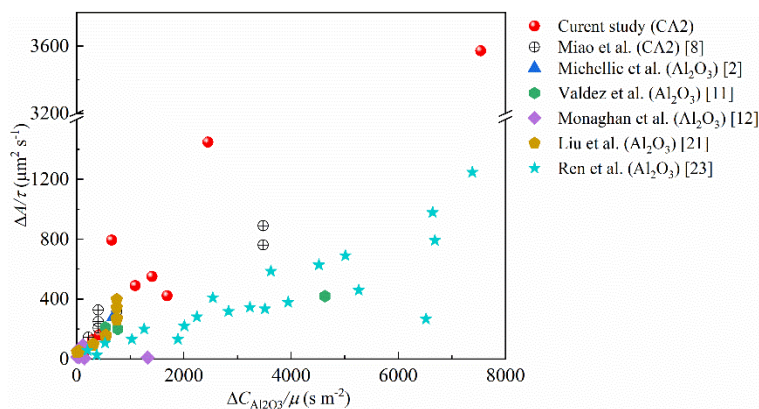


Figure 3.13 Average area reduction rate of different types of particles as a function of $(\Delta C_{Al_2O_3})/\mu$

3.4 Conclusions

1. The increase in temperature enhances the dissolution rate of CA2 across all types of CaO-Al₂O₃-SiO₂ slags. Furthermore, the dissolution rate of CA2 significantly decreases when the SiO₂ content increased from 10% to 40 wt.%. However, a further increase to 50 wt.% SiO₂ did not significantly influence the dissolution rate.
2. The significant decrease in total dissolution time from the slag with 40 wt.% SiO₂ to the slag with 10 wt.% SiO₂ is primarily affected by the change in slag structure.
3. At 1600°C, a higher C/A ratio leads to an increased CA2 dissolution rate. However, it was observed that the formation of melilite layer during the dissolution process acts as a hindrance, impeding the dissolution of the CA2 particle at 1550°C.
4. The presence of a boundary layer at the CA2 particle, C/A_4 slag interface is identified as a solid melilite phase which was observed at the surface of the CA2 particle in the CA2 particle, C/A_4 slag system. These observations are consistent with the thermodynamic predictions, validating the accuracy of the experimental and analytical methodologies employed.

Acknowledgments

The authors would like to thank the Natural Sciences and Engineering Research Council of Canada (NSERC) for funding this research. This research used a high temperature confocal laser scanning microscope-VL2000DX-SVF17SP funded by Canada Foundation for Innovation John Evans Leaders Fund (CFI JELF, Project Number: 32826), a PANalytical X'Pert diffraction instrument located at the Centre for crystal growth, Brockhouse Institute for Materials Research, and a scanning electron microscope-JEOL 6610 located at the Canadian Centre for Electron Microscopy at McMaster University. W. Mu would like to acknowledge Swedish Iron and Steel Research Office (Jernkonteret), STINT and SSF for supporting the time for international collaboration research regarding clean steel.

Statements and Declarations

On behalf of all authors, the corresponding author states that there is no conflict of interest.

Reference

1. M. Valdez, K. Prapakorn, A.W. Cramb, and S. Sridhar: *Steel Res. Int.* 2001, vol. 72, pp. 291-97.
2. S. Feichtinger, S.K. Michelic, Y.B. Kang, and C. Bernhard: *J. Am. Ceram. Soc.* 2014, vol. 97, pp. 316-25.
3. S. Waterfall S. Sun, N. Strobl, D. Liao, D. Holdridge: In *8th International Symposium on High-Temperature Metallurgical Processing*, Springer: 2017, pp 347-57.
4. W. Yang, L. Zhang, X. Wang, Y. Ren, X. Liu, and Q. Shan: *ISIJ Int.* 2013, vol. 53, pp. 1401-10.
5. Y. Liu L. Zhang, Y. Zhang, W. Yang, W. Chen: *Metall. Mater. Trans. B* 2018, vol. 49, pp. 1841-59.
6. K. Y. Miao, A. Haas, M. Sharma, W. Z. Mu, and N. Dogan: *Metall. Mater. Trans. B* 2018, vol. 49, pp. 1612-23.
7. P.T. Jones M. Guo, S. Parada, E. Boydens, J.V. Dyck, B. Blanpain, P. Wollants,: *J. Eur. Ceram. Soc.* 2006, vol. 26, pp. 3831-43.
8. A.G.Martinez M.A. Braulio, A.P.Luz, C. Liebske, V.C. Pandolfelli: *Ceram. Int.* 2011, vol. 37, pp. 1935-45.
9. Y. Kashiwaya, C.E. Cicutti, A.W. Cramb, and K. Ishii: *ISIJ Int.* 1998, vol. 38, pp. 348-56.
10. S. Sridhar and A.W. Cramb: *Metall. Mater. Trans. B* 2000, vol. 31, pp. 406-10.
11. M. Valdez, K. Prapakorn, A.W. Cramb, and S. Sridhar: *Ironmaking Steelmaking* 2002, vol. 29, pp. 47-52.
12. K.W. Yi, C. Tse, J.H. Park, M. Valdez, A.W. Cramb, and S. Sridhar: *Scand. J. Metall.* 2003, vol. 32, pp. 177-84.
13. A.B. Fox, J. Gisby, R.C. Atwood, P. D. Lee, and S. Sridhar: *ISIJ Inter.* 2004, vol. 44, pp. 836-45.
14. L. Chen B.J. Monaghan: *J. Non-Cryst. Solids* 2004, vol. 347, pp. 254-61.
15. B. J. Monaghan, L. Chen, and J. Sorbe: *Ironmaking steelmaking* 2005, vol. 32, pp. 258-64.
16. B.J. Monaghan and L. Chen: *Steel Res. Int.* 2005, vol. 76, pp. 348-54.
17. J. Liu, M. Guo, P.T. Jones, F. Verhaeghe, B. Blanpain, and P. Wollants: *J. Am. Ceram. Soc.* 2007, vol. 90, pp. 3818-24.
18. F. Verhaeghe, J. Liu, M. Guo, S. Arnout, B. Blanpain, and P. Wollants: *Appl. Phys. Lett.* 2007, vol. 91, p. 124104.
19. S. Michelic, J. Goriupp, S. Feichtinger, Y.B. Kang, C. Bernhard, and J. Schenk: *Steel Res. Int.* 2016, vol. 87, pp. 57-67.
20. C. Ren, L. Zhang, J. Zhang, S. Wu, P. Zhu, and Y. Ren: *Metall. Mater. Trans. B* 2021, vol. 52, pp. 3288-301.
21. C. Ren, C. Huang, L. Zhang, and Y. Ren: *Int. J. Miner., Metall. Mater.* 2023, vol. 30, pp. 345-53.
22. J. Liu, M. Guo, P.T. Jones, F. Verhaeghe, B. Blanpain, and P. Wollants: *J. Eur. Ceram. Soc.* 2007, vol. 27, pp. 1961-72.
23. X.L. Guo, Z.H.I. Sun, J. V.Dyck, M.X. Guo, and B. Blanpain: *Ind. Eng. Chem. Res.* 2014, vol. 53, pp. 6325-33.
24. X.L. Guo, J.V. Dyck, M.X. Guo, and B. Blanpain: *AIChE J.* 2013, vol. 59, pp. 2907-16.
25. T. Tian, Y. Zhang, H. Zhang, K. Zhang, J. Li, and H. Wang: *Int. J. Appl. Ceram. Technol.* 2019, vol. 16, pp. 1078-87.

26. Y. Ren, P. Zhu, C. Ren, N. Liu, and L. Zhang: *Metall.Mater.Trans. B* 2022, vol. 53, pp. 682-92.
27. B.J. Monaghan and L. Chen: *Ironmaking steelmaking* 2006, vol. 33, pp. 323-30.
28. M. Sharma, W. Mu, and N. Dogan: *JOM* 2018, vol. 70, pp. 1220-24.
29. H.A. Dabkowska M. Sharma, N. Dogan *Steel Res. Int.* 2019, vol. 90, p. 1800367.
30. M. Sharma and N. Dogan: *Metall. Mater.Trans. B* 2020, vol. 51, pp. 570-80.
31. K.H. Heo B.H. Yoon, J.S. Kim, H.S. Sohn: *Ironmaking steelmaking* 2002, vol. 29, pp. 214-17.
32. V.I. Ponomarev, D.M. Kheiker, and N.V. Belov: *Sovit Physics Crystallography* 1971, vol. 15, pp. 995-1002.
33. H. Shibata H. Chikama, T. Emi, M. Suzuki *Mater. Trans., JIM* 1996, vol. 37, pp. 620-26.
34. C.W. Bale, E. Bélisle, P. Chartrand, S.A. Decterov, G. Eriksson, A.E. Gheribi, K. Hack, I.H. Jung, Y.B. Kang, J. Melançon, A. D. Pelton, S. Petersen, C. Robelin, J. Sangster, P. Spencer, and M.A. Ende: *Calphad* 2016, vol. 55, pp. 1-19.
35. C.A. Schneider, W.S. Rasband, and K.W. Eliceiri: *Nat. Methods* 2012, vol. 9, pp. 671-75.
36. V.D. Eisenhüttenleute: *Slag Atlas*. Slag Atlas, 3rd ed., V.D. Eisenhüttenleute, ed., Slag Atlas, 2nd ed., Verlag Stahleisen GmbH, Dusseldorf, 1995.
37. C.J Xuan and W.Z Mu: *J. Am. Ceram. Soc.* 2019, vol. 102, pp. 6480-97.
38. R. Li, X. Wang, X. Gao, W. Wang, and Y. Zhou: *Ceram. Int.* 2024, vol. 50, pp. 8249-59.
39. D.R. Gaskell: *Metall. Treatises* 1981, vol. 6, pp. 59-78.
40. M. Ken: *Southern African Pyrometallurgy* 2011, vol. 7, pp. 35-42.
41. J.H. Park, I.H. Jung, and H.G. Lee: *ISIJ int.* 2006, vol. 46, pp. 1626-34.
42. K. H.Sandhage and G. J.Yurek: *J. Am. Ceram. Soc.* 1988, vol. 71, pp. 478-89.

Chapter 4

Impact of porosity and velocity on the dissolution behaviors of calcium aluminate inclusions in CaO-SiO₂-Al₂O₃ steelmaking slag: in-situ observations and model advancements

In Chapter 4, all experiments and data analysis were carried out by me. Mr. Moin Abid assisted with particle porosity characterization via X-ray Computational Tomography. Useful discussions on model development were provided by Dr. André B. Phillion. Useful discussions on the results were provided by Dr. André B. Phillion, Dr. Muhammad Nabeel, Dr. Neslihan Dogan and Dr. Wangzhong Mu.

The manuscript was initially drafted by me, edited, and revised to the final version by Dr. André B. Phillion, Dr. Muhammad Nabeel, Dr. Neslihan Dogan, and Dr. Wangzhong Mu. The final version has been reviewed by Mr. Moin Abid. This chapter has been published in *Journal of Materials and Metallurgical Transactions B*, 2025, DOI: <https://doi.org/10.1007/s11663-025-03556-1>. The following chapter is the pre-publication version of this article.

Impact of porosity and velocity on the dissolution behaviors of calcium aluminate inclusions in CaO-SiO₂-Al₂O₃ steelmaking slag: in-situ observations and model advancements

Guang Wang^{1*}, Muhammad Nabeel¹, Neslihan Dogan^{1,2*}, Moin Abid¹, Wangzhong Mu^{3,4}, A. B. Phillion¹

1 Department of Materials Science and Engineering, McMaster University, Hamilton L8S4L7, Ontario, Canada

2 Department of Materials Science and Engineering, Delft University of Technology, Mekelweg 2628CD, Delft, The Netherlands

3 Department of Materials Science and Engineering, KTH Royal Institute of Technology, Brinellvägen 23 10044, Stockholm, Sweden

4 Engineering Materials, Department of Engineering Science and Mathematics, Luleå University of Technology, Laboratorievägen 97187, Luleå, Sweden

* Contact email: wangg84@mcmaster.ca, n.d.dogan@tudelft.nl

Abstract:

The dissolution process of CaO·2Al₂O₃ (CA₂) particles in CaO-SiO₂-Al₂O₃ steelmaking slags was in-situ investigated at 1550°C. To better understand the role of particle porosity in dissolution kinetics, the particles with two different porosity levels, i.e., 0.08 and 0.20 were used in this study. The porosity (φ) and surface area of CA₂ particles were characterized through X-ray Computed Tomographic Imaging (XCT), and the surface area ratio ($f(\varphi)$) between the porous and full dense particles was expressed as $f(\varphi) = e^{5.3469\varphi}$. The obtained results indicated that an increase in the porosity from 0.08 to 0.20 led to an increase in the average dissolution rate from 0.35 to 0.59 $\mu\text{m/s}$. Moreover, the motion of CA₂ particles during the dissolution process was observed, suggesting its importance to include in the modeling approach. A novel mathematical model was developed to predict the dissolution time of inclusion particles by incorporating both the motion and porosity of particles. This model was validated against the existing literature data and aligned well with the current experimental findings. The model predictions demonstrated that the dissolution time of

CA2 particles was decreased with an increase in the velocity and porosity of particles and concentration difference of dissolving species between particle–slag interface and molten slag (ΔC), and a decrease in slag viscosity. Moreover, a parameter sensitivity analysis on the total dissolution time has been carried out to show the relative influence of concentration difference, particle porosity, particle velocity, and slag velocity on dissolution.

Keywords: dissolution mechanism models, calcium aluminate inclusion, particle velocity, particle porosity, in-situ observation

4.1 Introduction

Particle motion and dissolution behavior are widely investigated in both engineering and scientific applications. One of their vital applications in metallurgy is the control of steel cleanliness, where the dissolution process of non-metallic inclusions, referred to as “NMIs” herein, plays a critical role.[1] Once the NMIs enter the slag phase, they are expected to be dissolved in the molten slag as rapidly as possible. Any NMIs that remain as the undissolved particle may re-entrain into the molten steel, posing a significant industrial risk. They may agglomerate or coalesce, leading to clogging of the submerged entry nozzle, thus compromising product quality and production efficiency.

The dissolution mechanisms and kinetics of NMIs in slags have been well studied through experiments [2-4] and simulations [5-8] to support optimization of their removal efficiency from liquid steel during secondary refining of steelmaking. Over the past two decades, in-situ observation via High Temperature Confocal Laser Scanning Microscopy (HT-CLSM) [9-14], and Single Hot Thermocouple Technique (SHTT) [15, 16], have been the most common experimental methods used to investigate the dissolution process of NMIs. These techniques allow for real-time in-situ observation of the dissolution behavior of micron-size particles in molten slags. The main advantages of HT-CLSM over STHH are 1) image quality, 2) experimental temperature maintenance, and 3) reduced particle/slag mass ratio. [17] This third point is particularly important since a high particle/slag mass ratio (>1.0 wt.%) could cause a change in the slag composition and resulting properties (especially the species concentration difference and slag viscosity) during particle dissolution. [10, 18]. The STHH typically employs a particle/slag mass ratio at around 5 wt.% magnification, [16, 19, 20] significant exceeding the 1 wt.% limit identified by Lee and colleagues [10, 18]. In contrast, the particle/slag ratio used in HT-CLSM is less than 0.5 wt%. [11,

21]

The NMIs' size evolution with time, recorded by CCD camera (HT-CLSM), generates a dissolution profile that can be used to validate models of dissolution mechanisms. **Table 4.1** summarizes prior literature on the dissolution of NMIs in steelmaking slags via HT-CLSM. In these studies, however, it has been assumed that (1) the NMIs are non-porous particles, and (2) solute transfer related to NMI motion can be ignored. However, it is unlikely that NMIs are fully dense given the fact that, after they form within the liquid steel, they undergo growth by coalescence and agglomeration. Moreover, as listed in **Table 1**, the motion and rotation of NMIs have been observed in many studies but their impacts on the kinetics have not been adequately included within relevant dissolution mechanism models.

Previous investigations have primarily focused on the dissolution mechanisms and/or kinetics of Al_2O_3 [2, 4, 9, 12, 14-27], MgO [12, 15, 17, 18, 28], CaO [13, 29], SiO_2 [10, 30, 31], ZrO_2 [18, 20], MgAl_2O_4 [15, 18, 20, 32], $\text{TiO}_2 \cdot \text{Al}_2\text{O}_3$ [4, 33] and $\text{CaO} \cdot 2\text{Al}_2\text{O}_3$ (CA2) [11] in the ternary CaO - SiO_2 - Al_2O_3 based slag systems at temperatures ranging from 1250 to 1600°C, and for particle sizes that vary between 50 and 500 μm . The obtained findings indicate that the dissolution kinetics of NMIs are enhanced with increasing temperature and the concentration difference of dissolving species between the NMI-slag interface and bulk slag (i.e., the driving force (ΔC)). However, dissolution kinetics are diminished with an increasing slag viscosity [9, 16, 21, 22, 28, 29, 31]. It has also been reported that the dissolution rate of Al_2O_3 inclusions is increased using slags with high ratios of $\text{CaO}/\text{Al}_2\text{O}_3$ or CaO/SiO_2 [2, 16, 26].

A widely accepted approach for modeling the dissolution mechanism of NMIs in molten slag is the application of the so-called shrinking core model [34]. In this model, the limiting step for NMI dissolution is categorized as either chemical reaction (CR) control or boundary layer diffusion (BLD) control [34]. A separate approach, known as diffusion in a stagnant fluid model (DS), has also been used to interpret the dissolution mechanism of NMIs [35]. The dissolution profiles for CR, BLD, and DS, after dimensionless treatment, exhibit a unique profile shape: linear for CR, parabolic for BLD, and sigmoidal for DS. The actual dissolution mechanism of an NMI can be determined by comparing the models' prediction with the experimental dissolution curve. For instance, if the normalized experimental dissolution curve is parabolic, then the dissolution mechanism of NMI is believed to be BLD. As tabulated in **Table 4.1**, prior researchers have primarily identified either BLD or DS as the main mechanisms controlling particle dissolution.

Only a few studies[17, 18] have reported CR as the limiting step, and even fewer[16] reported mixed control as the limiting step (i.e. CR + BLD, indicating the formation of a solid product layer during dissolution). Nevertheless, it is not uncommon for different researchers to identify varying dissolution mechanisms for similar particle/slag systems. For example, Monaghan et al. reported that BLD was the limiting step for Al_2O_3 particles in the $\text{CaO-Al}_2\text{O}_3\text{-SiO}_2$ slag system, while DS was reported by Ren et al. [26, 27] in a similar slag system with slight compositional differences.

NMIs have been observed to not only dissolve but also to move, rotate, and dissociate within the molten slag during dissolution, as schematically illustrated in **Fig. 4.1**. Such phenomena could significantly impact dissolution mechanisms and kinetics by altering the fluid dynamics at the oxide-slag boundary, resulting in the shape change of the experimental dissolution curve [16, 28, 36]. Unfortunately, none of CR, BLD, and DS account for the motion of NMIs, which may explain the differences between the experimental and model prediction results [21, 28]. Pan et al. [36] incorporated the velocity of NMIs via the Péclet number to consider the convective mass transfer of the dissolving component. A better fit was obtained between model predictions and experimental results. However, the velocity was calculated based on the rotation of the NMIs, which normally only occurs for a specified duration and not over the entire dissolution process. As a result, the fixed angular velocity likely does not accurately represent the true velocity over time.

Another factor beyond NMI motion that must be considered is the porosity of NMIs. Since inclusion agglomeration occurs during industrial operations, the morphology of such agglomerated inclusions has been well studied, showing that they have porosity.[37, 38] For example, Yin et al. [39] observed that solid calcium aluminate inclusions were irregular in shape with coarse tips and pores.

The removal efficiency of NMIs from liquid steel during the refining process highly depends on their dissolution mechanisms and kinetics. Therefore, a better understanding of these processes requires investigating how the motion and porosity of NMIs affect their dissolution behaviors. Advancing conventional models to incorporate these factors will enable a more accurate determination of the dissolution mechanisms and prediction of the dissolution time of NMIs. In this study, the dissolution of $\text{CaO}\cdot 2\text{Al}_2\text{O}_3$ (CA2) particles was examined via HT-CLSM within synthesized $\text{CaO-Al}_2\text{O}_3\text{-SiO}_2$ metallurgical slag. Prior to experimentation, X-ray computed tomography (XCT) was used to quantify the porosity and surface area of the investigated CA2 particles. The results were used to develop a novel model that incorporates NMI motion and porosity on dissolution kinetics.

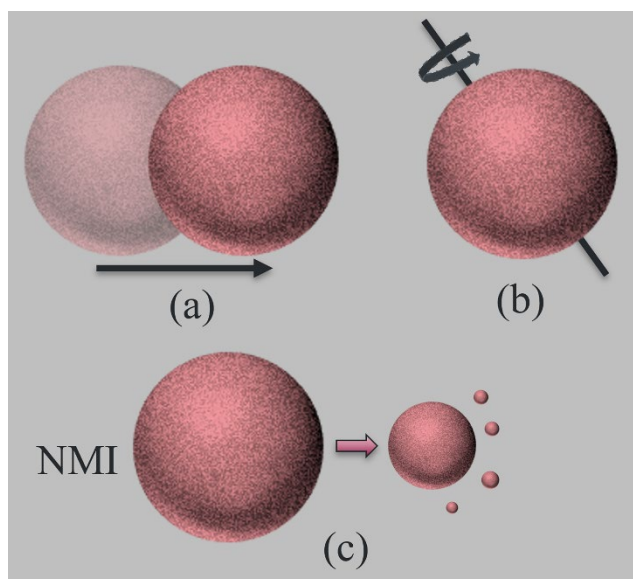


Figure 4.1. Potential NMI behavior during dissolution: (a) motion, (b) rotation, and (c) dissociation

Table 4.1 Summary of literature on the dissolution of NMIs in various slag systems using HT-CLSM

Authors	year	T (°C)	NMI	Slag system	Observed NMI behavior	Identified Rate limiting step	D*10 ⁻¹⁰ (m ² /s)
Sridhar et al.[1]	2000	1450-1550	Al ₂ O ₃	CASM	Rotation, dissociation	BLD	
Valdez et al.[2, 3]	2001	1470-1550	Al ₂ O ₃	CASM	Rotation, the interface became smooth	mixed BLD + CR	
			MgO	CASM	morphology change, the interface became smooth	BLD	
			MgAl ₂ O ₄	CASM	morphology change	mixed BLD + CR	
	2002	1470-1530	Al ₂ O ₃	CAS-(M)	Rotation (20-40s), product layer on particle surface in CASM slag. A smooth interface formed between CAS slag and particle	mixed CR + BLD	
Yi et al.[4]	2003	1450-1500	MgO	CAM	Motion, rotation	CR	
			Al ₂ O ₃	CAM		DS	
Fox et al.[5]	2004	1250-1500	Al ₂ O ₃	CASMNLB	Motion, rotation	CR	
			ZrO ₂	CASMNLB	Rotation, particle became transparent, smooth interface		
			MgO	CASMNLB	Motion, rotation		
Monaghan et al.[6-9]	2004	1477-1577	MgAl ₂ O ₄	CASMNLB	Motion, rotation		
			Al ₂ O ₃	CAS	Motion, rotation	BLD	0.15-3.09

	2005	1477-1577	Al ₂ O ₃	CAS	Motion, rotation		
			MgAl ₂ O ₄	CAS	Motion and motion		
			ZrO ₂	CAS	Gas bubbles generated around the particle		
Park et al.[10]	2005	1477-1577	Al ₂ O ₃	CAS	Motion, rotation	BLD	0.15-3.09
	2006	1504	MgAl ₂ O ₄	CAS	Rotation	BLD	0.67-2.20
	2006	1550	Al ₂ O ₃	CAS	Motion		
Liu et al.[11, 12]	2007	1500, 1600	MgO	CAS	Motion		
			MgO	CASM	Rotation (38-46s), detachment, particle became transparent, product layer	BLD	
			Al ₂ O ₃	CAS	Motion	DS	0.24-0.97
Verhaeghe et al.[13, 14]	2007	1470-1630	Al ₂ O ₃	CAS	Motion	DS	0.27-0.42
	2008	1600	Al ₂ O ₃	CAS	Motion, slight rotation	DS	0.22-0.28
Guo et al.[15, 16]	2008		Al ₂ O ₃	CAS	motion	DS	0.22-0.28
	2013	1480	CaO	CAS-(M)	Rotation, motion, and product layer on the particle surface	Mixed control (CR+BLD+PLD)	0.2-1.0
Feichtinger et al.[17]	2014	1450-1600	CaO	CAS-(M)	Rotation, generation of gas bubble from the particle	Formation of the IR layer	0.20-1.00
	2014	1450	SiO ₂	CAS	Rotation, motion	Revised DS	0.38-2.40
Michelic et al.[18]	2016	1600	Al ₂ O ₃	CASM	Rotation, motion	DS	0.04-33.80
Miao et al.[19]	2018	1500-1600	CaO·2Al ₂ O ₃	CAS	Rotation, motion	BLD	0.06-5.8

Ph.D. Thesis – G Wang; McMaster University – Materials Science & Engineering

Sharma et al.[20]	2018	1550	Al ₂ TiO ₅	CAS	Motion, rotation, color change from opaque to transparent	BLD	1-100
Tian et al.[21]	2018	1473-1573	SiO ₂	CAS/CASM	Interface becomes smooth	Revised DS	0.25-0.55
Sharma et al.[22]	2020	1500	Al ₂ TiO ₅	CAS	Slight motion, rotation	BLD	18-28 (Al ₂ O ₃), 25-38(TiO ₂)
Ren et al.[23-25]	2021	1450-1580	Al ₂ O ₃	CAS	Dissociation for some particles	DS	0.047-1.1
	2022	1520-1570	SiO ₂	CASM		DS	1.0-10.0
	2023	1500-1600	Al ₂ O ₃	CAS		DS	2.8-4.1
Li et al.[26]	2024	1500-1600	Al ₂ O ₃	CASM	Rotation	BLD	16.6-95.2
Deng et al.[27]	2024	1450-1550	Al ₂ O ₃	CASMT		BLD	2.18-4.18

A: Al₂O₃, B: B₂O₃, C: CaO, F: FeO, L: Li₂O, M: MgO, N: Na₂O, S: SiO₂, T: TiO₂.

BLD: boundary layer diffusion; CR: chemical reaction; DS: diffusion in the stagnant slag; PLD: product layer diffusion.

D: determined diffusion coefficient of dissolving species in slags.

4.2 Methodology

4.2.1 Experiments

4.2.1.1 Material

High-purity laboratory-grade powder of CaO, Al₂O₃, SiO₂, and CaCO₃ (Alfa Aesar, USA) was used to produce synthetic inclusion particles and slags. To remove moisture, the CaO was roasted in a Si-Mo rod box type resistance furnace (maximum temperature: 1200°C) at 1050°C for 12 h, while the Al₂O₃, SiO₂, and CaCO₃ were dried in a drying oven (maximum temperature: 400°C) at 150°C for 24 h before use.

To explore the effect of CA2 porosity on the dissolution process, two types of CA2 particles were prepared: porous (p-CA2) and dense (d-CA2). Porous CA2 particles, p-CA2, were prepared by sintering 100 g of CaCO₃ and Al₂O₃ powder in stoichiometric amounts at 1600°C for 24 h under an argon atmosphere. The details for powder mixing and sintering are available in one of our previous studies [1]. Dense CA2 particles, d-CA2, were obtained by melting approximately 5 g of the p-CA2 particles in a water-cooled copper mold using an arc melter. The slag composition used in this study, i.e. 33CaO-18Al₂O₃-49SiO₂ (wt.%), was the same as a previous study [2].

4.2.1.2 Experiments

An HT-CLSM (VL2000DX-SVF17SP, Yonekura) was used to carry out the CA2 dissolution experiments, providing continuous in-situ observation. Technical details and operation procedures for the HT-CLSM facility are available elsewhere [3, 4]. Each experiment was conducted as follows. First, approximately 0.15 g of slag was pre-melted in a platinum crucible (5 µm in diameter and 6 µm in height) within the HT-CLSM furnace. Second, a CA2 particle (either the p-type or the d-type) was placed on top of the pre-melted slag, and the assembly was heated to the experimental temperature according to a specified heating profile: rapid heating (1000 °C/min) to 50°C below the test temperature, slow heating (50°C/min) to the test temperature. The start time of dissolution, t_0 , was defined as the time (at the test temperature) when the CA2 particle became fully immersed within the molten slag. The entire dissolution process of the CA2 particle was recorded using a CCD camera at a frame rate of 5 frames per second. The captured images have a resolution of 1024×1024 pixels, with each pixel corresponding to a size of 0.9 µm when using a 5X objective lens and 2.3 µm when using a 2X objective lens. Note that the mass of the CA2 particle used in each dissolution experiment was less than 0.1 wt.% of that of slag. As a result, the slag composition and properties were not

affected by the dissolution of particle.

Data postprocessing was carried out using the ImageJ software [5] to determine the time-evolution of the dissolution process. Each CA2 particle was segmented from the slag in each frame based on image contrast, and the particle diameter was measured. The measurements were repeated three times to reduce manual error, and then averaged. From this data, the evolution in equivalent radius, assuming a spherical particle, was determined.

4.2.1.3 Characterization

X-ray diffraction (XRD) (Panalytical X'pert diffraction instrument, using a copper source with a wavelength of 1.540 56 Å) was employed to identify the phases present within the synthesized CA2 particles.

X-ray computed tomography (XCT) was conducted on two p-CA2 and two d-CA2 particles using a ZEISS Xradia 630 Versa system to characterize the surface area and internal porosity of the CA2 particles. In total, two XCT scans were performed, one for each type of particle, with the same scan parameters applied for both scans. The field of view for each scan was approximately 2.6 mm × 2.6 mm, with two particles in each XCT scan. This resulted in a volumetric dataset comprising approximately 2036×2036×2036 voxels, with a voxel size of 1.3 μm. For each scan, 2401 radiographs were acquired over a 360-degree rotation with an exposure time of 5.5 seconds per radiograph. An accelerating voltage of 90 kV was used during the imaging process. The CA2 particles were sandwiched between Kapton tape layers to ensure secure positioning on the sample holder and to prevent sample fluttering during image acquisition. Postprocessing was carried out using the Dragonfly software to determine the pore number density, apparent surface area, and pore volume of CA2 particles. Due to the irregular shape of CA2 particles, the volume of the surface-connected pores could not be measured directly and only the internal pores were counted using the Dragonfly analysis software as shown in **Fig. 4.2(a)**. To address this challenge, the 3D XCT images of all four particles were cropped into spheres with a fixed radius $r = 150 \mu\text{m}$. This value was chosen since it represents the radius of the maximum sphere that can be fit within the irregularly shaped CA2 particles. The total volume of internal and surface-connected pores was measured without distinction, as cropping could convert internal pores into surface-connected ones (**Fig. 4.2(b)**).

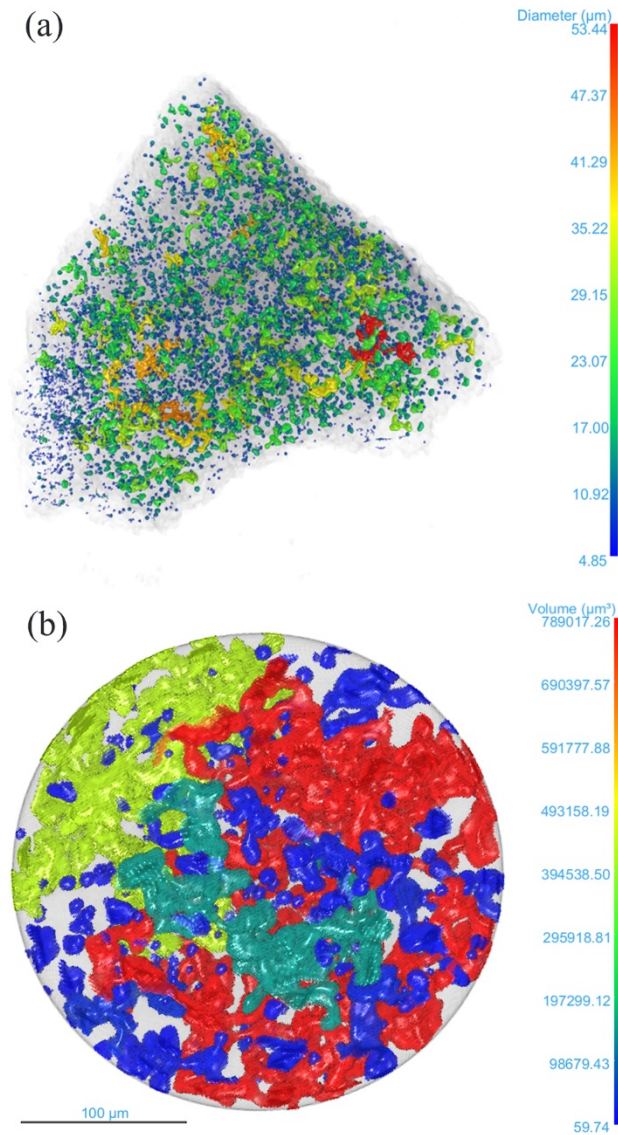


Figure 4.2 X-ray Computed Tomography images of one d-CA2 particle prepared by arc melting (a) presents the original CA2 particles, and (b) present corresponding cropped spheres (radius 150 μm). Color maps indicate equivalent spherical diameters (a) and pore volumes (b).

4.2.2 Model development

During a particle dissolution, a particle's time-dependent mass loss, J_1 (m/s), is formulated as:

$$J_1 = -\frac{1}{S_s} \frac{dM_P}{dt} \quad (1)$$

where M_P is the particle mass (kg) and S_s is the surface area of the particle (m²/s). By assuming that the particle is nonporous and spherical, M_P and S_s can be expressed as:

$$M_p = V_P \rho_P = \frac{4}{3} \pi r^3 \rho_P \quad (2)$$

$$S_s = 4\pi r^2 \quad (3)$$

where V_p is the particle volume (m^3), ρ_p is the particle density (kg/m^3), and r is the equivalent spherical radius (m). According to mass conservation, the loss rate of the particle J_1 must equal the mass flux, J_2 (m/s), across the boundary layer:

$$J_1 = J_2 \quad (4)$$

where J_2 can be determined from:

$$J_2 = -k_m(C_{sat} - C_0) \quad (5)$$

where k_m is the apparent rate constant, C_{sat} is the saturation concentration of the dissolving species, and C_0 is the concentration of the dissolving species in the bulk slag. Coupling equations from (1) to (5), the time-dependent radius gives:

$$\frac{dr}{dt} = -\frac{k_m(C_{sat}-C_0)}{\rho_p} \quad (6)$$

Chemical Reaction Control: In this approach, it is assumed that the apparent rate constant k_m is controlled by the chemical reaction rate, k_c , between the particle and molten slag, and further that k_c is a constant. Integrating both sides of equation (6), from r_0 to r and from 0 to τ , gives [6]:

$$\frac{r}{r_0} = 1 - \frac{t}{\tau} \quad (7)$$

$$\tau = \frac{\rho_p}{(C_{sat}-C_0)k_c} \quad (8)$$

where r_0 is the initial equivalent radius of the particle (m). τ is the total dissolution time of the particle (s).

The dissolution limiting step is considered CR if the normalized experimental dissolution curve matches the curve from equation (7).

Boundary Layer Diffusion Control: In this approach, it is assumed that the mass transfer rate is governed by mass transport of reactants and products to and from the slag-particle interface, and further that the thickness of the boundary layer and the concentration profile of the dissolving species can be assumed to be constant. Under conditions of “Stokes flow”, the influence of convection can also be ignored. As a result, the mass transfer coefficient can be expressed as the ratio of the diffusion coefficient to the particle radius, *i.e.*, $k_m = D/r$. Integrating both sides of equation (6) from r_0 to r and from 0 to τ , gives [6]:

$$\frac{r}{r_0} = \left(1 - \frac{t}{\tau}\right)^{1/2} \quad (9)$$

$$\tau = \frac{\rho_p r_0^2}{2(C_{sat}-C_0)D} \quad (10)$$

The dissolution limiting step is determined as BLD when the normalized experimental dissolution curve aligns with the curve predicted by equation (9).

As discussed in the introduction, several studies have reported the motion of particles during the dissolution process, suggesting its importance to include in the modeling. Moreover, the pores within the particle, affecting the dissolution kinetics by altering the contact area between the particle and bulk slag, should also be considered in the modeling.

4.2.2.1 Incorporation of particle porosity

To incorporate particle porosity, equations (2) and (3) can be rewritten as:

$$M_p = V_p \rho_p (1 - \varphi) = \frac{4}{3} \pi r^3 \rho_p (1 - \varphi) \quad (11)$$

$$S_s = f(\varphi) 4\pi r^2 \quad (12)$$

where φ represents the particle porosity as compared to a solid sphere of equivalent diameter, $f(\varphi)$ defines a function that represents the change in particle surface area due to surface porosity. Equation (6) then becomes:

$$\frac{dr}{dt} = - \frac{k_m (C_{sat} - C_0) f(\varphi)}{\rho_p (1 - \varphi)} \quad (13)$$

More details on the methodology for determining surface area and particle porosity are provided in section 3.1.

4.2.2.2 Incorporation of particle velocity

Convective flow resulting from particle motion enhances mass transport of the dissolving species thereby reducing the thickness of the boundary layer between slag and particle. The Péclet number, $Pe = 2rv/D$ [7] where v is the particle velocity, is a dimensionless quantity used to quantify the importance of convective transport as compared to diffusive transport. In this study, it can be assumed that convection fluxes are caused by natural convection because of the density gradient in the molten slag. This is because there are no external forces within the HT-CLSM to otherwise stir the molten slag or induce particle movement. As a result, particle velocity during dissolution is given by [8, 9]:

For $Re < 1$,

$$v = \frac{2r^2 * (\rho_p - \rho_s) * (1 - \varphi) * g}{9\mu_s} \quad (14)$$

For $1 < Re < 10^5$

$$v = \sqrt{\frac{8gr(\rho_p - \rho_s)(1 - \varphi)}{3\rho_s C_D}} \quad (15)$$

$$C_D = \frac{24}{Re} (1 + 0.15Re^{0.687}) + \frac{0.42}{1+42500Re^{-1.16}} \quad (16)$$

where $Re = \frac{2rv\rho_S}{\mu_S}$ is the Reynolds number with μ_S being the viscosity of the slag (Pa·s), C_D is the drag coefficient. ρ_S is the density of the slag (kg/m³) and g is the force of gravity (m/s²).

Assuming that the mass transfer rate is governed by both the diffusion of the dissolving species as well as convection due to the particle's motion [10]:

For $Pe \leq 10000$,

$$k_m = \frac{D(4+1.21*Pe^{\frac{2}{3}})^{\frac{1}{2}}}{2r} \quad (17-1)$$

For $Pe > 10000$,

$$k_m = \frac{1.1DPe^{1/3}}{2r} \quad (17-2)$$

Coupling equations (13), (17-1), and (17-2), the dissolution rate is given as:

For $Pe \leq 10000$,

$$\frac{dr}{dt} = - \frac{f(\varphi)(C_{sat}-C_0)D(4+1.21*Pe^{\frac{2}{3}})^{\frac{1}{2}}}{2r\rho_p(1-\varphi)} \quad (18-1)$$

For $Pe > 10000$,

$$\frac{dr}{dt} = - \frac{1.1f(\varphi)(C_{sat}-C_0)DPe^{\frac{1}{3}}}{2r\rho_p(1-\varphi)} \quad (18-2)$$

The above equations were numerically solved using MATLAB via the ode45 solver. This new model is named Modified Mass transfer-controlled Dissolution Model (MMDM).

4.3 Results and discussion

4.3.1 Characterization of calcium aluminates

Fig. 43 presents the XRD patterns of d-CA2 (blue line) and p-CA2 (red line), which align well with the standard reference CA2 (black line) [11]. The absence of additional phases confirms the successful synthesis of high-purity CA2 particles.

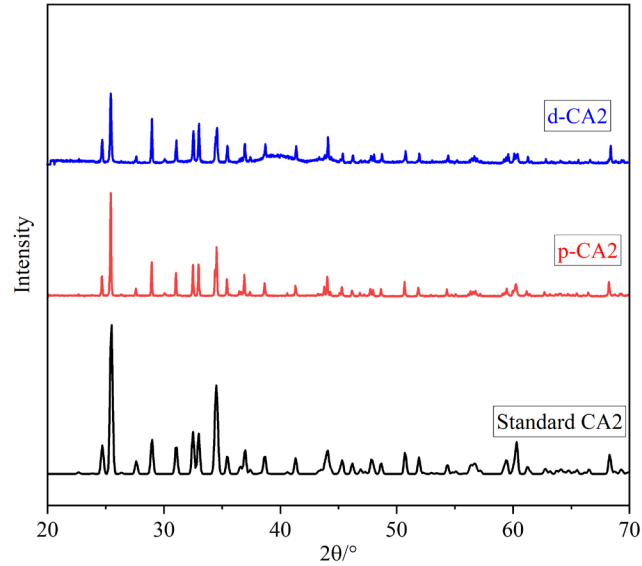


Figure 4.3 XRD patterns of d-CA2 (blue line), p-CA2 (red line), and standard CA2 (black line)

Table 4.2 provides the physical properties of the two p-CA2 and two d-CA2 particles analyzed via 3D XCT. As can be seen, the porosities of p-CA2 particles are higher than that of d-CA2 particles (0.20 and 0.29 vs. 0.08 and 0.12). This illustrates that the arc melting considerably reduced the porosity of the CA2 particles. In terms of surface area, the table also shows that the ratio of the effective surface area to the surface of an equivalent sphere varies from particle to particle but the values for p-CA2 is always much greater than ones for d-CA2, further indicating the complex geometry and porosity of CA2 particles.

Table 4.2 Summary of physical parameters of cropped CA2 particles

Particle	Pore Volume (*10 ⁶ μm ³)	$f(\varphi)$	Fraction Porosity
p1-CA2	2.8	3.3	0.20
p2-CA2	4.1	4.1	0.29
d1-CA2	1.2	1.2	0.08
d2-CA2	1.7	2.7	0.12

The values of ratio, $f(\varphi)$, can be plotted as a function of porosity φ , as shown in **Fig. 4.4**. It should be noted that the first data point in **Fig. 4.4** is a theoretical value, corresponding to $\varphi = 0$, where $f(\varphi) = 1$. An exponential relationship is observed between $f(\varphi)$ and φ ,

$$f(\varphi) = e^{5.3469\varphi} \quad (19)$$

Accordingly, equations (18-1) and (18-2) were rewritten to incorporate this relationship,

For $Pe \leq 10000$,

$$\frac{dr}{dt} = - \frac{e^{5.3469\varphi}(C_{sat}-C_0)D(4+1.21*Pe^{\frac{2}{3}})^{\frac{1}{2}}}{2r\rho_p(1-\varphi)} \quad (20-1)$$

For $Pe > 10000$,

$$\frac{dr}{dt} = - \frac{1.1*e^{5.3469\varphi}(C_{sat}-C_0)DPe^{\frac{1}{3}}}{2r\rho_p(1-\varphi)} \quad (20-2)$$

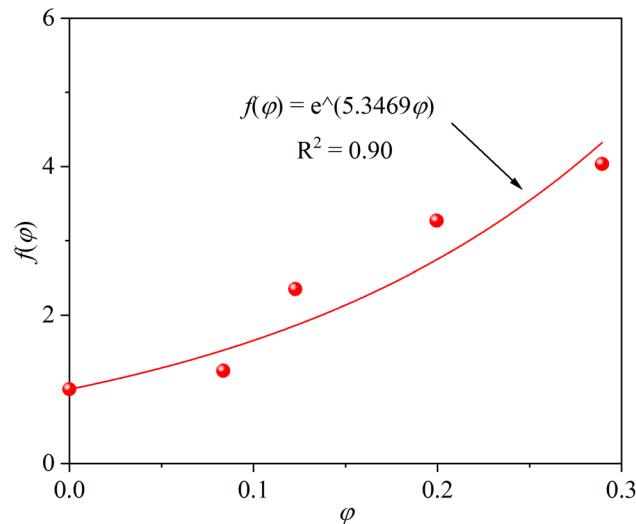


Figure 4.4 XCT-determined specific surface area $f(\varphi)$ as a function of porosity, φ , along with a best-fit exponential curve through the data points.

4.3.2 Effect of CA2 particle behaviors on the dissolution kinetics

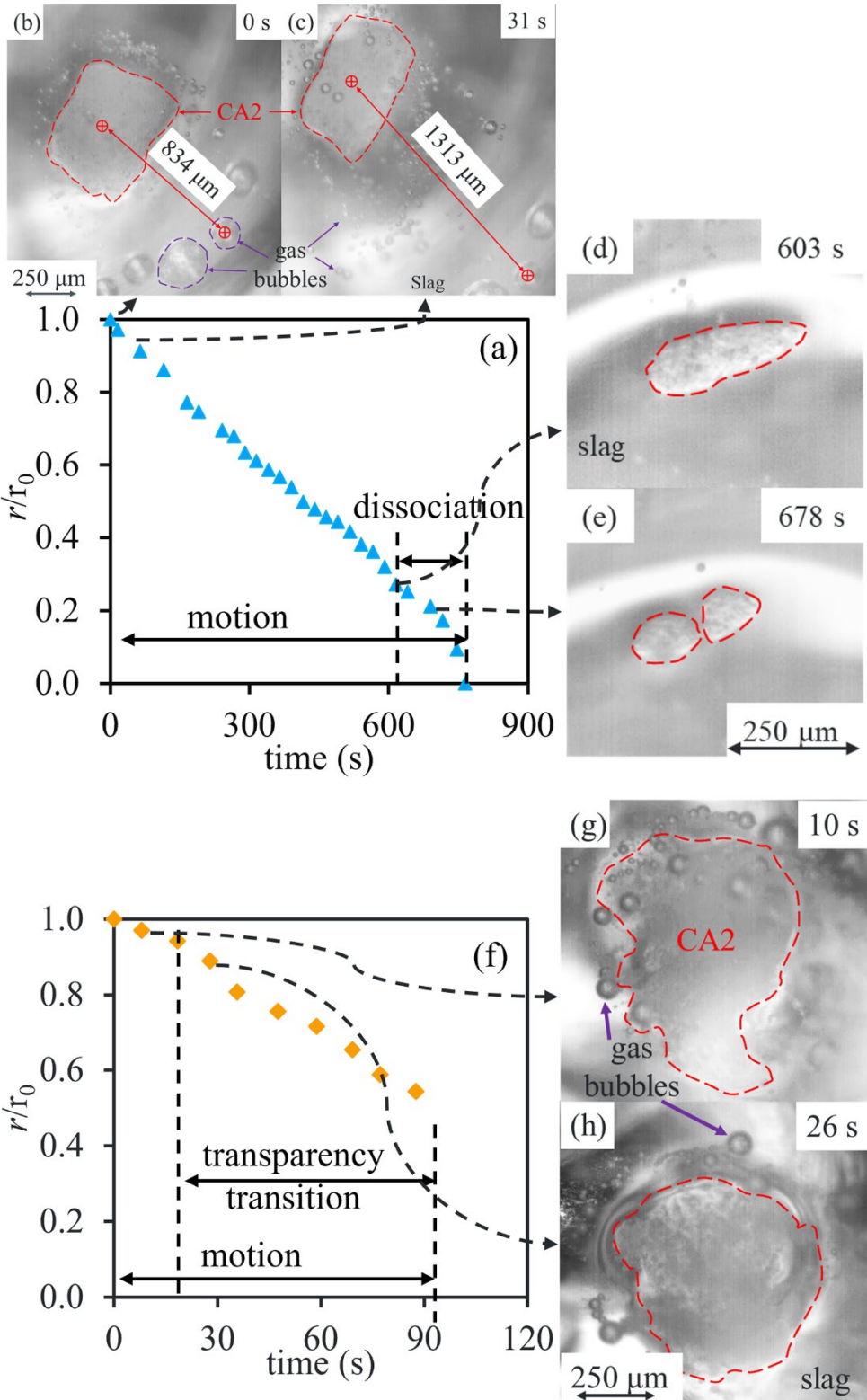
During the dissolution experiments of the CA2 particles at 1550°C in slag, various particle behaviors were observed including motion, dissociation, transparency transition and interaction with gas bubbles. Notably, particle motion was consistently observed, whereas the other behaviors were only observed in specific experiments. **Fig. 4.5** presents a sequence of images illustrating these behaviors. The solid red and purple boundaries denote projection areas of CA2 particle and gas bubbles, respectively, with the surrounding area comprised of transparent molten slag. The corresponding dissolution curves, normalized by initial radius and segmented by behavioral

sections, are also provided.

Fig. 4.5 (a-e) depict the dissolution of the d1-CA2 particle, which exhibited both motion throughout the test and dissociation after 603 s. The particle was observed to move a considerable distance, 479 μm over the first 31 s, resulting in an average velocity of 15.4 $\mu\text{m/s}$. The dissociation resulted in the formation of two smaller fragments. The dissolution curve shows approximately linear behavior until dissociation. The steepened slope during the dissociation phase indicates that dissociation enhanced dissolution by increasing the contact area between the particle and molten slag. This observation underscores the importance of considering the actual surface area of a porous particle in modeling. Note that the radius of the d1-CA2 particle after dissociation was determined from the combined projection area of both fragments.

Fig. 4.5 (f-h) show the dissolution of the p2-CA2 particle, which dissolved rather quickly and dissociated after 90 s. The main feature to highlight with this particle is the transition in transparency, changing from opaque to semi-transparent, from 20 s to 90 s. Changes in inclusion transparency were also reported by Fox et al. [12] for an Al_2O_3 particle, Liu et al. [13] for a MgO particle, and Sharma et al. [14] for an Al_2TiO_5 particle. After 90 s, the semi-transparent particle dissociated into numerous smaller fragments, which subsequently dissolved rapidly. Data collected after 90 s was excluded as measuring the projection area of these fragments became impractical. Moreover, the p2-CA2 particle exhibited movement throughout the dissolution process. [12-14]

Another phenomenon observed during the dissolution process was the interaction of the particle with a gas bubble, as illustrated in **Fig. 4.5 (i-k)**. This observation is for the dissolution of a p-CA2 whose porosity and surface area were not determined using XCT. The particle interacted with a gas bubble for ~ 118 s, between 230 s and 338 s. Initially, the particle dissolved relatively quickly, but dissolution was effectively paused during the period that the particle interacted with the gas bubble. After exiting the gas bubble, the dissolution rate returned to its initial value. As a result, it is clear that the gas bubble obstructed the interaction between the p-CA2 and molten slag, thereby hindering the mass transport of dissolved species from the p-CA2 - slag interface to bulk slag. Note that after the d1-CA2 particle dissociated into two fragments, the projection area for both fragments was measured separately via the ImageJ software [49]. The total projection area from both fragments was then added together to determine a total projection area and subsequently the equivalent radius of the dissociated d1-CA2 particle.



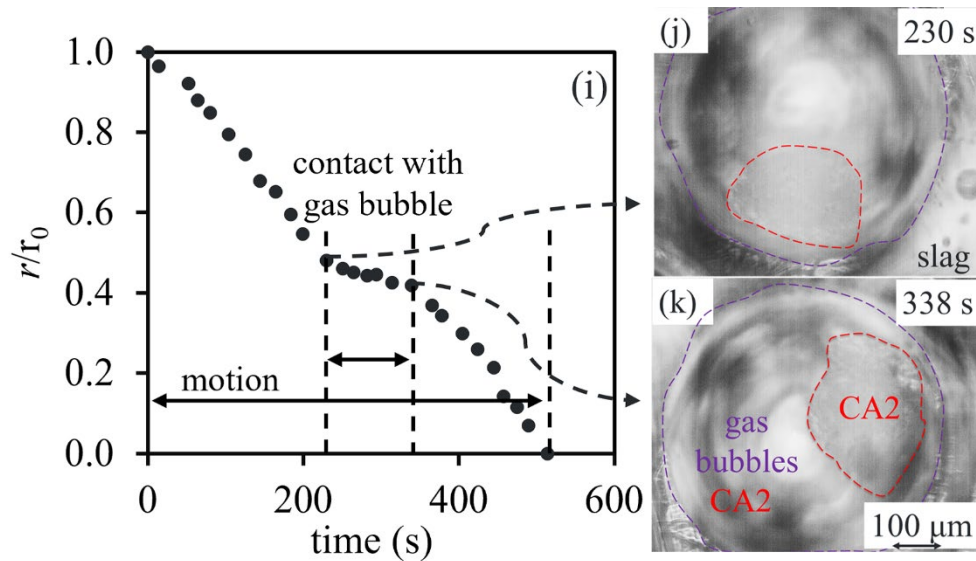


Figure 4.5 Evolution of normalized radius changes of CA2 particles as a function of time in slag at 1550°C, illustrating different CA2 particle behaviors observed during the dissolution process: (a-e) motion and dissociation in the slag of d1-CA2, (f-h) motion and transparency transition of p2-CA2, and (i-k) motion and interaction with a gas bubble of p-CA2.

4.3.3 Effect of CA2 particle porosity on the dissolution kinetics

The relationship between porosity and dissolution kinetics at 1550°C in slag can be examined by looking at the total dissolution time of three of the four CA2 particles characterized via XCT. However, dissociation occurred very early-on during the experiment for p2-CA2, and so it was excluded. **Table 4.3** summarizes the dissolution time and rate of CA2 particles with different porosities. For p1-CA2 (ϕ of 0.20, $r_0 = 346 \mu\text{m}$), τ was around 591 s. For d1-CA2 (ϕ of 0.08, $r_0 = 297 \mu\text{m}$), τ was around 603 s. However, that particle only partially dissolved, to 91 μm , prior to dissociation. Finally, for d2-CA2 (ϕ of 0.12, $r_0 = 105 \mu\text{m}$), τ was around 295 s. This data can be used to determine a total dissolution rate, which is seen to increase from approximately 0.34 $\mu\text{m/s}$ to 0.59 $\mu\text{m/s}$ as the porosity increased from 0.08 to 0.20, indicating that higher porosity enhances the dissolution rate. This is attributed to the larger surface area associated with higher porosity, which increases the reaction area between particle and molten slag.

Table 4.3 Summary of CA2 particle dissolution time and rate at 1550°C

particle	r_0 (μm)	r_τ (μm)	φ	τ (s)	$(r_0-r_\tau)/\tau$ ($\mu\text{m/s}$)
p2-CA2	346	0	0.20	591	0.59
d1-CA2	297	91	0.08	603	0.34
d2-CA2	105	0	0.12	295	0.35

4.4 Validation and application of MMDM

4.4.1 MMDM validation

Experimental data from the literature[15] were employed to validate the MMDM and compare its performance with other conventional models. The dissolution of a spherical Al_2O_3 particle into 29.7CaO-24.1 Al_2O_3 -46.2 SiO_2 (wt.%) slag observed using CLSM at 1550°C, as reported by Liu et al.[15], was selected for validation. They employed the DS model to determine the dissolution mechanism, which assumes the NMI-slag interface is invariant. This means that the diffusion field would have stayed once the NMI-slag interface had been fixed at the beginning of the dissolution. For a spherical particle dissolution, based on Fick's first and second laws, the dissolution rate of the particle is expressed as[16]:

$$\frac{dr}{dt} = -\frac{c_{sat}-c_0}{c_p-c_{sat}} \frac{D}{r} - \frac{c_{sat}-c_0}{c_p-c_{sat}} \sqrt{\frac{D}{\pi t}} \quad (21)$$

This study was chosen due to the spherical shape of Al_2O_3 particles, aligning with a critical assumption: the particle is spherical for all four models. Moreover, Liu et al. reported particle motion during the dissolution process, which they identified as a primary scatter source in their experimental data. Unfortunately, the porosity of the spherical alumina particle was not specified, so a value of $\varphi = 0$ was assumed in the current model for validation. Equations (7 and 8) for CR model, equations (9-11) for BLD model, equation (20-1) for MMDM, and equation (21) for DS model were solved using the parameters provided in **Table 4.4** from Liu's work[15]. The obtained normalized dissolution curves based on each model are presented in **Fig. 4.6**. The spherical markers represent Liu's experimental results, while the dashed-dotted, dotted, solid, and dashed lines correspond to predictions of the CR model, BLD model, MMDM, and DS model, respectively. The CR model and MMDM initially agreed with experimental data for $t/\tau < 0.20$. When t/τ is between 0.2 and 0.45, the predictions of both MMDM and DS models are close to the experimental data. Beyond 0.45, only the MMDM aligns well with experimental data. By

accounting for the motion of the spherical particle in the molten slag, the MMDM offers a more accurate representation of the dissolution mechanism under experimental conditions.

Table 4.4 Parameters used in the models

r_0 (μm)	ρ_{slag} (kg/m^3)	$\rho_{\text{Al}_2\text{O}_3}$ (kg/m^3)	μ ($\text{Pa}\cdot\text{s}$)	$\Delta C_{\text{Al}_2\text{O}_3}$ (kg/m^3)	D (m^2/s)	τ (s)
250	2622	3950	2.10	651	2.50E-11	1982

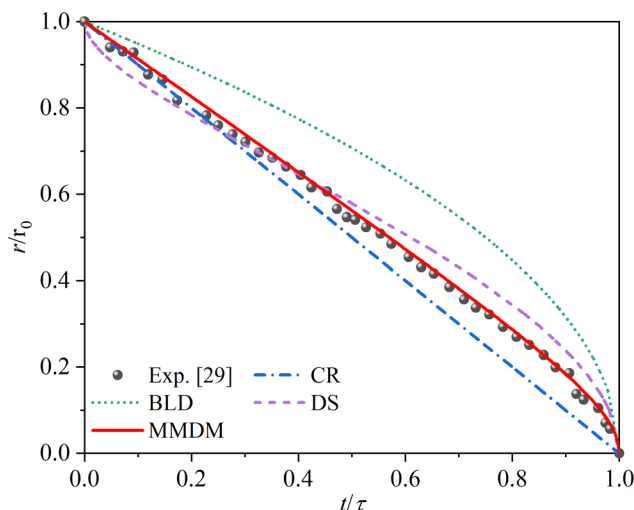


Figure 4.6 Normalized dissolution curves for spherical Al_2O_3 particle in molten slag at 1550°C compared with different dissolution rate-controlling models

To investigate the influence of particle motion on the shape of the dissolution curve, the k_m of Al_2O_3 particle in 29.7CaO-24.1 Al_2O_3 -46.2 SiO_2 (wt.%) slag was analyzed over time using the BLD, and MMDM, with parameters provided in **Table 4.4**. The CR and DS models were excluded due to their assumptions, which do not yield k_m . In contrast, the BLD and MMDM require D to determine k_m , with D values of $9.57 \times 10^{-11} \text{ m}^2/\text{s}$ and $2.75 \times 10^{-11} \text{ m}^2/\text{s}$, respectively. D is back-calculated according to the total dissolution time in both BLD and MMDM. For the same total dissolution time, different D values are obtained with different models.

Fig. 4.7(a) illustrates k_m as a function of t/τ . In both BLD and MMDM, k_m increases with t/τ . Initially ($t/\tau < 0.7$), the k_m in BLD is slightly lower than in MMDM. However, beyond this point, k_m in BLD surpasses MMDM, which is inconsistent with expectations. This discrepancy arises because BLD only accounts for diffusion, leading to an overestimated D . In contrast, MMDM

incorporates both natural convection and diffusion, resulting in a higher k_m compared to BLD. **Fig. 4.7(b)** shows the ratio of D/k_m , interpreted as the boundary layer thickness. The MMDM consistently predicts a thinner boundary layer than BLD throughout the dissolution process. Given that D remains constant for a specific particle-slag system at a fixed temperature, a thinner boundary layer corresponds to a higher k_m . Thus, particle motion effectively reduces the boundary layer thickness, enhances k_m , and leads to a steeper dissolution curve compared to the BLD model (**Fig. 4.6**).

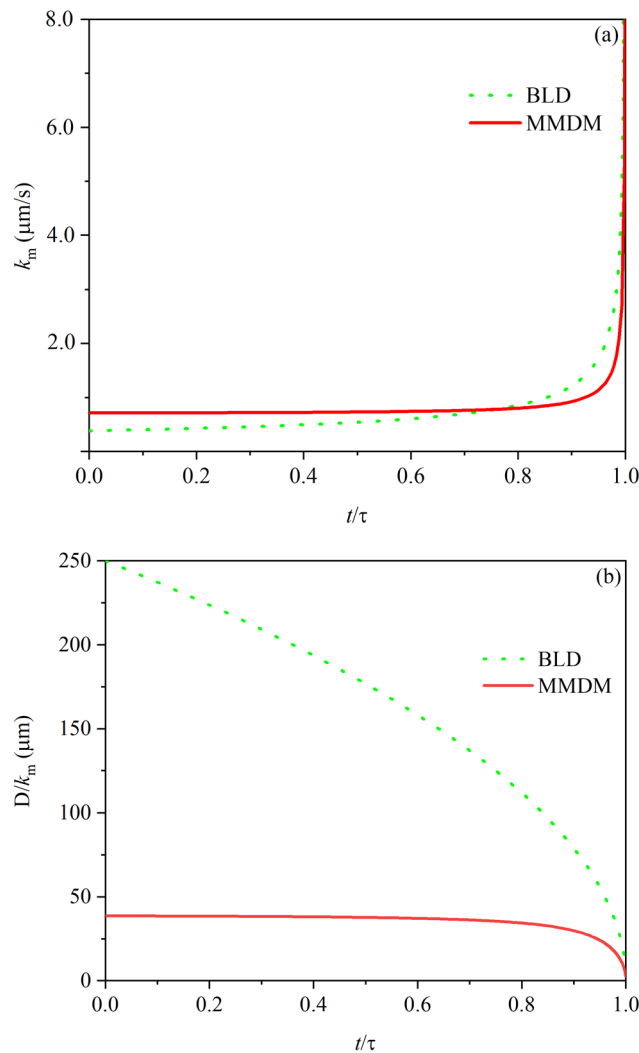


Figure 4.7 (a) variation of k_m as a function of t/τ for BLD and MMDM. (b) Variation of D/k_m as a function of t/τ for BLD and MMDM.

4.4.2 MMDM application

4.4.2.1 Determination of diffusion coefficient of CA2

The dissolution rate-limiting step of CA2 particles was first identified by comparing normalized dissolution curves with model predictions. The best fitted model was then applied to determine the diffusion coefficient of CA2 particle in slag at 1550°C. The $\Delta C_{Al_2O_3}$ and μ are 1481 kg/m³ and 1.36 Pa·s for slag at 1550°C, respectively, which were calculated by FactSage 8.0 with the FToxid databases [17]. The rest of the parameters required for the models' calculation can be found in **Table 4.2**.

Fig. 4.8(a) presents normalized experimental data and predictions of four models (diamonds: experimental data, dashed-dotted line: CR, dotted line: BLD, dashed line: DS, and solid line: MMDM). As can be seen, when the t/τ is less than 0.5, both CR and MMDM aligned well with experimental data. After that, DS and MMDM agreed with the experimental data. Therefore, the MMDM has a much better fitting with experimental data by incorporating the porosity and motion of CA2 particles, indicating that mass transfer, including natural convection and diffusion, is the primary rate-limiting step for CA2 particle dissolution in the slag. The diffusion coefficient, 1.25×10^{-11} m²/s, of CA2 in slag at 1550°C was determined using MMDM, which is in the range reported by the literature [1].

The determined diffusion coefficient, 1.25×10^{-11} m²/s, was applied to predict the dissolution time for the d1-CA2 and d2-CA2 particles using MMDM in slag at 1550°C. As shown in **Fig. 4.8(b)**, the total dissolution time (including the time after dissociation) for the d1-CA2 particle with radii of 297 μm is 764 s, 51 s shorter than the MMDM prediction of 815 s. This discrepancy is likely due to the particle dissociation observed after 603 s, as discussed in section 3.2. Additionally, the average velocity of CA2 particle, calculated using equation (14), is 14.2 μm/s, closely aligns with the experimentally measured average velocity of 15.4 μm/s, determined from the CA2 particle's displacement during the first 31 s of recorded dissolution images. For the d2-CA2 with a radius of 105 μm, the total dissolution time is 297 s, slightly exceeding the MMDM prediction of 284 s by 13 s. Despite slight variations, the MMDM predictions closely match the experimental dissolution times. The experimental dissolution curves for both types of CA2 particles align well with the MMDM predictions, confirming that mass transfer is the rate-limiting step for CA2 dissolution. The findings also indicate that particle porosity impacts dissolution time, underscoring its importance in predicting dissolution kinetics accurately.

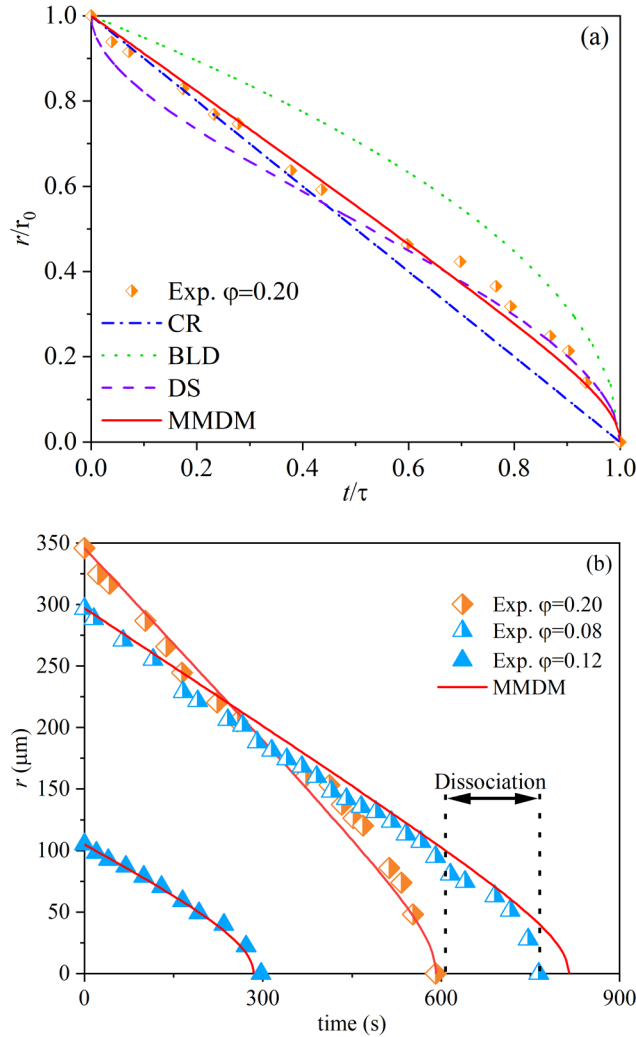


Figure 4.8 (a) Comparison of normalized dissolution curves for p1-CA2 particles and four models, (b) Comparison of CA2 particle's radius change as a function of time between experiments and MMDM prediction in slag at 1550°C.

4.4.2.2 Prediction of CA2 dissolution time

The MMDM model was applied to predict the total dissolution time of CA2 particles in CaO-Al₂O₃-SiO₂ slags at 1550°C. **Fig. 4.9** shows two heatmaps, showing τ with variations in ϕ and v , and with variations in μ and ΔC , for $r_0 = 200 \mu\text{m}$. Beginning with **Fig. 4.9(a)**, it can be seen that as v increases from 0 $\mu\text{m/s}$ to 10 $\mu\text{m/s}$, τ decreases significantly, particularly for ϕ is less than 0.2. Beyond $v = 10 \mu\text{m/s}$, τ decreases slightly with further increasing v to 40 $\mu\text{m/s}$. Similarly, increasing ϕ from 0 to 0.4 reduces τ , highlighting the role of porosity in enhancing dissolution by increasing the effective contact/surface area between molten slag and particle. The combined effects of v and ϕ demonstrate that higher v and ϕ lead to shorter dissolution times, emphasizing their importance

in accurately modeling particle dissolution in slags. In **Fig. 4.9(b)**, it can be seen that τ was decreased when decreasing μ and increasing ΔC . Moreover, the τ is more sensitive to the low ΔC region with the same μ . For example, when $\mu = 2 \text{ Pa}\cdot\text{s}$, increasing ΔC from 200 kg/m^3 to 800 kg/m^3 reduces τ from 2551 s to 637 s, but further increasing ΔC to 1600 kg/m^3 reduces τ only to 318 s. A similar trend was observed for the changes in μ . Note that in this figure, $\varphi = 0.2$ is assumed.

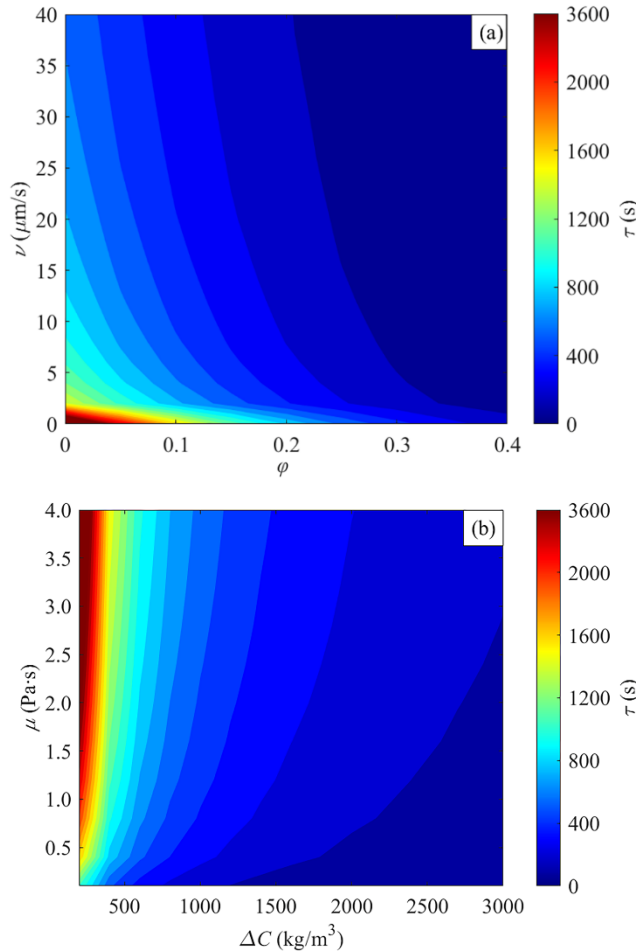


Figure 4.9 Prediction of the total dissolution time of CA2 particles in CaO-Al₂O₃-SiO₂ slag at 1550°C a) variation of ν and φ , b) variation of μ and ΔC . (the color bar is nonuniform)

A parameter sensitivity study was conducted to evaluate the relative influence of ν , ΔC , φ and μ on τ_1 predicted by the used the MMDM. The reference parameters ($X_{r(i)}$) were set as $\nu = 10 \text{ }\mu\text{m/s}$, $\varphi = 0.1$, $\mu = 1 \text{ Pa}\cdot\text{s}$ and $\Delta C = 1000 \text{ kg/m}^3$, yielding a baseline dissolution time of $\tau_r = 790 \text{ s}$. Each parameter (X_i) was varied independently by increasing or decreasing its value fourfold relative to the reference, with a step change of twofold, except ΔC , which was halved. **Fig. 4.10** presents the

percentage change of τ as a function of parameter variation. For $0.25 \leq X_i/X_{r(i)} \leq 2$, ΔC has the most significant effect on τ , while μ has the least impact. However, for $2 < X_i/X_{r(i)} \leq 4$, φ becomes the most influential parameter, and ν has the smallest impact on τ . Consequently, the order of parameter influence is for $0.25 \leq X_i/X_{r(i)} \leq 2$, $\Delta C > \varphi > \nu > \mu$, and for $2 < X_i/X_{r(i)} \leq 4$, $\varphi > \Delta C > \mu > \nu$. Moreover, the sensitivity of τ to parameter variations is more pronounced at lower values than at higher ones.

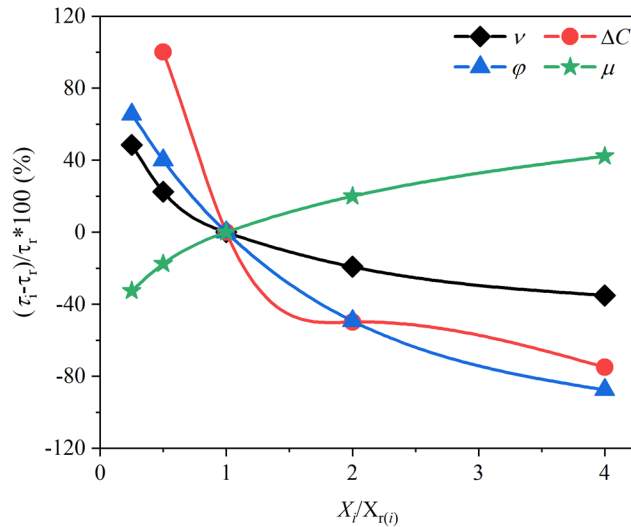


Figure 4.10 Effects of parameters variation (ν , ΔC , φ and μ) on the total dissolution time in percentage

4.5 Conclusions

In this study, two types of porosity level CA2 particles, p-CA2 and d-CA2, were prepared by sintering and arc melting, respectively, with their porosities and surface areas characterized using XCT. The dissolution process of these CA2 particles in CaO-Al₂O₃-SiO₂ type slag was investigated through in-situ observation. A dissolution model was then developed, incorporating the motion and porosity of CA2 particles. The key findings are as follows:

- 1) The dissolution behavior of CA2 particles, including motion, dissociation, and interaction with gas bubbles, has been observed and described during the experiments. The first two behaviors enhanced the dissolution of the CA2 particles while the interaction with the gas bubble slowed down dissolution.
- 2) Increasing the porosity of CA2 particles enhances dissolution kinetics, with the average dissolution rate rising from 0.35 $\mu\text{m/s}$ to 0.59 $\mu\text{m/s}$ as porosity increases from 0.08 to 0.20.
- 3) A mathematical model named “modified mass transfer-controlled dissolution model

(MMDM)” was developed by incorporating particle velocity and porosity assuming natural convection. This model can provide a better fit with experimental results as compared to the conventional models lacking these considerations. The MMDM prediction showed that the total dissolution kinetics of CA2 particles was enhanced by an increase in ϕ , v and ΔC , and a decrease in μ . The parameter sensitivity analysis found that the order of parameter influence is for $0.25 \leq X_i/X_{r(i)} \leq 2$, $\Delta C > \phi > v > \mu$, and for $2 < X_i/X_{r(i)} \leq 4$, $\phi > \Delta C > \mu > v$.

Nomenclatures

Nomenclatures	
J_1	the mass loss rate of the particle (m/s)
J_2	mass flux through boundary layer (m/s)
M_P	mass of the particle (kg)
S_S	the nonporous surface area of the particle (μm^2)
S_1	the porous surface area of the particle (μm^2)
P_P	density of the particle (kg/m^3)
ρ_s	density of slag (kg/m^3)
R	radius of the particle (μm)
r_0	initial radius of the particle (μm)
T	total dissolution time of particle (s)
T	dissolution time particle (s)
K	mass transfer coefficient of dissolving species (m/s)
D	diffusion coefficient of dissolving species (m^2/s)
C_{sat}	saturation concentration of dissolving species (kg/m^3)
C_0	concentration of dissolving species in bulk slag (kg/m^3)
C_P	the concentration of dissolving species in particles (kg/m^3)
ΔC	concentration of dissolving species between that at x and bulk slag (kg/m^3)
ϕ	porosity of the particle
Pe	Péclet number
Re	Reynolds number
N	velocity of particle (m/s)

μ_s	viscosity of slag (Pa·s)
C_D	drag coefficient
g	gravity (m/s^2)

Acknowledgments

The authors would like to thank the Natural Sciences and Engineering Research Council of Canada (NSERC) for funding this research. This research used a High Temperature Confocal Laser Scanning Microscopy-VL2000DX-SVF17SP funded by Canada Foundation for Innovation John Evans Leaders Fund (CFI JELF, Project Number: 32826), an X-ray Computed Tomography-Zeiss Xradia 630 Versa located at the Canadian Centre for Electron Microscopy at McMaster University.

Statements and Declarations

On behalf of all authors, the corresponding author states that there is no conflict of interest.

Reference

1. C.J. Xuan and W.Z. Mu: *J. Am. Ceram. Soc.* 2020, vol. 104, pp. 57-75.
2. R. Li, X. Wang, X. Gao, W. Wang, and Y. Zhou: *Ceram. Int.* 2024, vol. 50, pp. 8249-59.
3. A.J Deng, H.C Wang, and D.D Fan: *ISIJ Int.* 2021, vol. 61, pp. 2475-82.
4. M. Sharma, W. Mu, and N. Dogan: *Jom* 2018, vol. 70, pp. 1220-24.
5. C.J Xuan and W.Z Mu: *J. Am. Ceram. Soc.* 2019, vol. 102, pp. 6480-97.
6. J.J Liu, J. Zou, M.X. Guo, and N. Moelans: *Comput. Mater. Sci.* 2016, vol. 119, pp. 9-18.
7. J. Heulens, B. Blanpain, and N. Moelans: *Acta Mater.* 2011, vol. 59, pp. 2156-65.
8. F. Verhaeghe, S. Arnout, B. Blanpain, and P. Wollants: *Phys Rev E Stat Nonlin Soft Matter Phys* 2006, vol. 73, p. 036316.
9. A.W. Cramb S. Sridhar: *Metall. Mater. Trans. B* 2000, vol. 31, pp. 406-10.
10. S.K. Michelic S. Feichtinger, Y.B. Kang, C. Bernhard: *J. Am. Ceram. Soc.* 2014, vol. 97, pp. 316-25.
11. K. Y. Miao, A. Haas, M. Sharma, W. Z. Mu, and N. Dogan: *Metall. Mater. Trans. B* 2018, vol. 49, pp. 1612-23.
12. J.H. Park, I.H. Jung, and H.G. Lee: *ISIJ int.* 2006, vol. 46, pp. 1626-34.

13. X.L. Guo, J.V. Dyck, M.X. Guo, and B. Blanpain: *AIChE J.* 2013, vol. 59, pp. 2907-16.
14. Z. Deng, X. Zhang, G. Hao, C. Wei, and M. Zhu: *Int. J. Miner., Metall. Mater.* 2024, vol. 31, pp. 977-87.
15. M. Valdez, K. Prapakorn, A.W. Cramb, and S. Sridhar: *Steel Res. Int.* 2001, vol. 72, pp. 291-97.
16. M. Valdez, K. Prapakorn, A.W. Cramb, and S. Sridhar: *Ironmaking Steelmaking* 2002, vol. 29, pp. 47-52.
17. K.W. Yi, C. Tse, J.H. Park, M. Valdez, A.W. Cramb, and S. Sridhar: *Scand. J. Metall.* 2003, vol. 32, pp. 177-84.
18. A.B. Fox, J. Gisby, R.C. Atwood, P. D. Lee, and S. Sridhar: *ISIJ Inter.* 2004, vol. 44, pp. 836-45.
19. L. Chen B.J. Monaghan: *J. Non-Cryst. Solids* 2004, vol. 347, pp. 254-61.
20. L. Chen B. J. Monaghan, J. Sorbe: *Ironmaking steelmaking* 2005, vol. 32, pp. 258-64.
21. B.J. Monaghan and L. Chen: *Steel Res. Int.* 2005, vol. 76, pp. 348-54.
22. J. Liu, M. Guo, P.T. Jones, F. Verhaeghe, B. Blanpain, and P. Wollants: *J. Am. Ceram. Soc.* 2007, vol. 90, pp. 3818-24.
23. F. Verhaeghe, J. Liu, M. Guo, S. Arnout, B. Blanpain, and P. Wollants: *Appl. Phys. Lett.* 2007, vol. 91, p. 124104.
24. F. Verhaeghe, J. Liu, M. Guo, S. Arnout, B. Blanpain, and P. Wollants: *J. Appl. Phys.* 2008, vol. 103, p. 023506.
25. S. Michelic, J. Goriupp, S. Feichtinger, Y.B. Kang, C. Bernhard, and J. Schenk: *Steel Res. Int.* 2016, vol. 87, pp. 57-67.
26. C. Ren, L. Zhang, J. Zhang, S. Wu, P. Zhu, and Y. Ren: *Metall. Mater. Trans. B* 2021, vol. 52, pp. 3288-301.
27. C. Ren, C. Huang, L. Zhang, and Y. Ren: *Int. J. Miner., Metall. Mater.* 2023, vol. 30, pp. 345-53.
28. J. Liu, M. Guo, P.T. Jones, F. Verhaeghe, B. Blanpain, and P. Wollants: *J. Eur. Ceram. Soc.* 2007, vol. 27, pp. 1961-72.
29. X.L. Guo, Z.H.I. Sun, J. V.Dyck, M.X. Guo, and B. Blanpain: *Ind. Eng. Chem. Res.* 2014, vol. 53, pp. 6325-33.

30. T. Tian, Y. Zhang, H. Zhang, K. Zhang, J. Li, and H. Wang: *Int. J. Appl. Ceram. Technol.* 2019, vol. 16, pp. 1078-87.
31. Y. Ren, P. Zhu, C. Ren, N. Liu, and L. Zhang: *Metall.Mater.Trans. B* 2022, vol. 53, pp. 682-92.
32. B.J. Monaghan and L. Chen: *Ironmaking steelmaking* 2006, vol. 33, pp. 323-30.
33. M. Sharma and N. Dogan: *Metall. Mater.Trans. B* 2020, vol. 51, pp. 570-80.
34. O. Levenspiel: *Chemical reaction engineering*. John wiley & sons, 1998.
35. M.J. Whelan: *Met. Sci. J.* 1969, vol. 3, pp. 95-97.
36. P. Yan, B.A. Webler, P.C. Pistorius, and R.J. Fruehan: *Metall. Mater. Trans. B* 2015, vol. 46, pp. 2414-18.
37. L. C. Zheng, A. Malfliet, B. Q. Yan, Z. H. Jiang, B. Blanpain, and M. X. Guo: *ISIJ Int.* 2022, vol. 62, pp. 1573-85.
38. S. K.Michelic and C. Bernhard: *Steel Res. Int.* 2022, vol. 93.
39. H.B. Yin, H. Shibata, T. Emland, and M. Suzuk: *ISIJ Int.* 1997, vol. 37, p. 10.
40. G Wang, M. Nabeel, W.Z. Mu, A.B. Phillion, and N.Dogan: *J. Iron Steel Res. Int.* 2025, vol. 30, pp. 1-12.
41. H. Chikama, H. Shibata, T. Emland, and M. Suzuk: *Mater. Trans., JIM* 1996, vol. 37, pp. 620-26.
42. C. Orrling, Y. Fang, N. Phinichka, S. Sridhar, and A.W. Cramb: *JOM-e* 1999, vol. 51.
43. C.A. Schneider, W.S. Rasband, and K.W. Eliceiri: *Nat. Methods* 2012, vol. 9, pp. 671-75.
44. T.K. Sherwood, R.L. Pigford, and C.R. Wilke: *Mass transfer*. McGraw-Hill New York, 1975.
45. Y.X. Zhang and Z.J. Xu: *Earth Planet. Sci. Lett.* 2003, vol. 213, pp. 133-48.
46. D.L. Turcotte and G. Schubert: *Geodynamics applications of continuum physics to geological problems*. 1982.
47. T.K. Sherwood, R.L. Pigford, and C.R. Wilke: *Mass transfer*. McGraw-Hill New York, 1975.
48. V.I. Ponomarev, D.M. Kheiker, and N.V. Belov: *Sovit Physics Crystallography* 1971, vol. 15, pp. 995-1002.

49. C.W. Bale, E. Bélisle, P. Chartrand, S.A. Deckerov, G. Eriksson, A.E. Gheribi, K. Hack, I.H. Jung, Y.B. Kang, J. Melançon, A. D. Pelton, S. Petersen, C. Robelin, J. Sangster, P. Spencer, and M.A. Ende: *Calphad* 2016, vol. 55, pp. 1-19.

Chapter 5

Dissolution kinetics and mechanisms of calcium aluminates inclusions in CaO-Al₂O₃-SiO₂-(MgO) steelmaking slags

In Chapter 5, all experiments and data analysis were carried out by me. Useful discussions on the results were provided by Dr. Neslihan Dogan, Dr. Muhammad Nabeel, Dr. André B. Phillion, and Dr. Wangzhong Mu.

The manuscript was initially drafted by me, edited, and revised to the final version by Dr. Neslihan Dogan, Dr. André B. Phillion, Dr. Muhammad Nabeel, and Dr. Wangzhong Mu. This chapter has been submitted to *Ceramics International*, 2025, Manuscript Number: CERI-D-25-04226. The following chapter is the draft version of the manuscript.

Dissolution kinetics and mechanisms of calcium aluminates inclusions in CaO-Al₂O₃-SiO₂-(MgO) steelmaking slags

Guang Wang^{1*}, Muhammad Nabeel¹, Neslihan Dogan^{1,2*}, Wangzhong Mu^{3,4}, A. B. Phillion¹

1 Department of Materials Science and Engineering, McMaster University, Hamilton L8S4L7, Ontario, Canada

2 Department of Materials Science and Engineering, Delft University of Technology, Mekelweg 2628CD, Delft, The Netherlands

3 Department of Materials Science and Engineering, KTH Royal Institute of Technology, Brinellvägen 23 10044, Stockholm, Sweden

4 Engineering Materials, Department of Engineering Science and Mathematics, Luleå University of Technology, Laboratorievägen 12, 97187, Luleå, Sweden

* Contact email: wangg84@mcmaster.ca, n.d.dogan@tudelft.nl

Abstract:

The dissolution kinetics and mechanisms of solid calcium aluminate inclusions (CaO·2Al₂O₃ (CA2) and CaO·6Al₂O₃ (CA6)) in CaO-Al₂O₃-SiO₂-(MgO) metallurgical slags at 1550°C were investigated using high temperature confocal laser scanning microscopy (HT-CLSM). The effects of slag viscosity, CaO/Al₂O₃ (C/A) ratio, and MgO content on the dissolution time of CA6 and slag MgO content on that of CA2 particles were examined by tracking the time dependent changes of particle projection areas. The obtained results showed that the dissolution kinetics of CA2 and CA6 particles was enhanced by an increase in slag MgO content. Moreover, increasing C/A ratio of slag or decreasing slag viscosity improved the dissolution rate of CA6 particles. Post dissolution analysis using scanning electron microscopy equipped with energy dispersive X-ray spectroscopy (SEM-EDS) combined with thermodynamic calculations revealed the dissolution paths of CA6 particles in slag S3 with C/A ratio 3.8 and S6 with 8.0 wt.% MgO, where the dissolution time is out of expectation. It was found that an intermediate solid layer melilite formed around the undissolved CA6 particle in slag S3 with C/A ratio 3.8, reducing its dissolution rate. Conversely, the formation of randomly dispersed intermediate solid products around the undissolved CA6 particle in slag S6 with 8 wt.% MgO did not impend their dissolution rate. Finally, based on the

obtained findings, two distinct dissolution mechanisms were proposed advancing the understanding of solid inclusion dissolution in metallurgical slags. The findings obtained from this study aim to provide new insights to further improve steel cleanliness for the longevity of the product service life.

Keywords: dissolution mechanisms and kinetics, solid calcium aluminate inclusions, in-situ observation, clean steel.

5.1. Introduction

Steel cleanliness significantly affects the production efficiency and the properties of steels, where the size, number, shape, and composition of non-metallic inclusions (NMIs) are critical factors. [1] Unfortunately, NMIs inevitably form during the secondary steelmaking due to deoxidation and calcium treatment during the ladle furnace (LF) refining process, reoxidation between steel and slag, containers or atmosphere, and erosion and/or corrosion of refractory materials. [2] Inadequate calcium additions during calcium treatment – to modify irregularly shaped solid alumina-based NMIs to liquid or semi-liquid calcium aluminates with more spherical morphology – can lead to the formation of endogenous solid calcium aluminate NMIs. [1, 3] Erosion and corrosion of the refractory lining by the molten slag and steel can result in the formation of exogenous calcium aluminate NMIs, especially for those incorporated with solid calcium aluminates to improve their thermal shock resistance and extend their service life. [4-6] Both endogenous and exogenous NMIs detrimentally affect steel cleanliness and can also hinder steel castability by causing submerge entry nozzle clogging.

During secondary steelmaking, most NMIs are removed by dissolution into the molten slag after floating to the liquid steel – slag interface. [7, 8] Rapid dissolution kinetics are crucial to prevent re-entrainment into molten steel and/or clustering within the submerged entry nozzle. [9, 10] Conversely, slow dissolution kinetics is desirable to ensure their longevity and maintain service life as refractory materials. Over the past two decades, high-temperature confocal laser scanning microscopy (HT-CLSM) has been developed and extensively used to investigate the dissolution behaviors of solid NMIs under conditions relevant to steelmaking, providing in-situ real-time observation. Studies have investigated the dissolution mechanisms and kinetics of NMIs in various steelmaking slag systems as summarized in [11]. However, only a few studies have examined the effect of slag composition and temperature on dissolution kinetics of complex calcium aluminates,

particularly $\text{CaO}\cdot 2\text{Al}_2\text{O}_3$ (CA2). Miao et al. [12] reported that higher temperature and lower SiO_2 content in the slag increased the dissolution rate of CA2 particles. Wang et al. [13] reported that the dissolution kinetics of CA2 particles was enhanced with increasing temperature and slag $\text{CaO}/\text{Al}_2\text{O}_3$ ratio, as well as decreasing slag viscosity. However, the formation of a melilite layer around CA2 particle hindered its dissolution in slag with $\text{CaO}/\text{Al}_2\text{O}_3$ ratio of 3.8 at 1550°C . [13] Guo et al. [14] observed that an increase in MgO content in slag decreased the dissolution time of CA2 particles. Despite those findings, to the best of the current authors' knowledge, no studies have reported the dissolution kinetics and mechanisms of CA6 particles in $\text{CaO}-\text{Al}_2\text{O}_3-\text{SiO}_2-(\text{MgO})$ slag system in the open literature.

Previous studies have shown that intermediate solid products can either accelerate or hinder dissolution. For instance, Park et al. [15] found that CA2 and CA6 formation in the $\text{CaO}-\text{Al}_2\text{O}_3-\text{SiO}_2$ type slags did not retard Al_2O_3 particles' dissolution rate, whereas the formation of a ring-like layer of $\text{MgO}\cdot\text{Al}_2\text{O}_3$ and $2\text{CaO}\cdot\text{SiO}_2$ slowed MgO particles dissolution. Similarly, Guo et al. [16] reported that the formation of a $(2\text{CaO}\cdot\text{SiO}_2)$ layer impeded CaO particles dissolution in $\text{CaO}-\text{Al}_2\text{O}_3-\text{SiO}_2-(\text{MgO})$ slags. Despite these observations of intermediate solid products formation during particles' dissolution, studies on their formation mechanisms and impact – even their common industrial occurrence – remain limited.

A deeper understanding of the dissolution kinetics and mechanisms of CA2 and CA6 NMIs in $\text{CaO}-\text{Al}_2\text{O}_3-\text{SiO}_2-(\text{MgO})$ metallurgical slags is essential, particularly the role of intermediate solid products. In this research, a comprehensive study of the dissolution behavior of CA2 and CA6 particles in eight different $\text{CaO}-\text{Al}_2\text{O}_3-\text{SiO}_2-(\text{MgO})$ metallurgical slags has been investigated at 1550°C using HT-CLSM. The effects of slag chemistry on the dissolution kinetics of CA2 and CA6 particles were examined by varying the C/A ratio, viscosity, and MgO content of slags. Interrupted dissolution experiments of CA6 particles in two slags were conducted separately, supplemented by post-experiment analyses using SEM-EDS and thermodynamic calculations to reveal the dissolution reactions at the particle – slag interface, paths and mechanisms. The results of this study aim to clarify the dissolution kinetics, reactions, paths, and mechanisms of CA2 and CA6 particles in $\text{CaO}-\text{Al}_2\text{O}_3-\text{SiO}_2-(\text{MgO})$ metallurgical slags and to understand how underlying factors influence their dissolution behaviors. The obtained knowledge will help improve steel cleanliness, production efficiency and the service life of refractories by enabling the design or selection of optimal slag compositions during refining.

5.2. Methodology

5.2.1 Material

Reagent-grade powder of CaCO_3 , CaO , Al_2O_3 , SiO_2 , and MgO (Alfa Aesar, USA) was used to synthesize calcium aluminates inclusions (CA2 and CA6) and slags. To avoid the effect of moisture, CaO and MgO were roasted in a muffle furnace for 12 h at 1050°C , while the CaCO_3 , Al_2O_3 , and SiO_2 were dried in an oven for 24 h at 150°C before use.

Both CA2 and CA6 pellets were prepared by sintering a 100 g mixture of CaCO_3 and Al_2O_3 powder in stoichiometric amounts at 1600°C for 24 h under an argon atmosphere, respectively. CA2 particles were obtained from our previous study [13] and detailed descriptions of the powder mixing and sintering are available elsewhere [12]. The same method was employed to produce CA6 particles.

Three regions of sintered CA6 pellet, i.e. the center layer (purple line), middle layer (blue line), and outer layer (black line), were characterized using X-ray diffraction with a Panalytical X'pert diffraction instrument equipped with a cobalt source (wavelength: 1.789 \AA). As shown in **Fig. 5.1**, the X-ray diffraction peaks of all three layers align well with the standard CA6 peaks [17] (ICSD 202316, red line), with no other phases detected. These results confirm the successful synthesis of high-purity CA6 particles by sintering. Similar findings were made for CA2 particles. [13]

Additionally, the porosity of CA2 and CA6 were measured by X-ray computed tomography (XCT) with a ZEISS Xradia 630 Versa system. The average volume fraction of porosity in CA2 and CA6 particles was found to be 0.25 and 0.39, respectively. The procedure for carrying out X-ray tomography, and then determining the volume fraction of voids, can be found in [11].

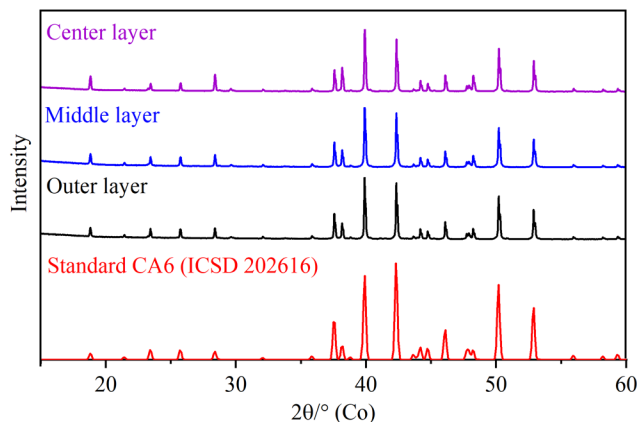


Figure 5.1 XRD patterns of the CA6 pellets sintered at 1600°C under argon atmosphere for 24 h

Slag samples were prepared by mixing powders of CaO, Al₂O₃, SiO₂, and MgO in stoichiometric amounts based on the designed composition. The mixtures were heated to 1550°C, at least 50°C higher than the theoretical liquidus temperature of each slag, in a platinum crucible (70 ml volume) and placed in a Si-Mo rod resistance furnace. After fully melted, the slag was held isothermally for 4 h to ensure homogenization. The platinum crucible was then removed from the furnace, and molten slag was poured into a steel plate for cooling.

Eight different slags were prepared, with the composition presented in **Table 5.1**. S1, S2, and S3, which have similar SiO₂ contents but different C/A ratios, were used to study the effect of the C/A ratio on the dissolution kinetics of CA6 particles. S4, S5, and S6, with similar SiO₂ content and C/A ratios but varying MgO contents, were used to investigate the influence of MgO content on the dissolution kinetics of CA2 and CA6 particles. Additionally, S8 was designed to further explore the effect of MgO content on the CA2 dissolution kinetics with similar $\Delta C_{Al_2O_3}$ as S4. S1, S4, and S7 were employed to explore the effect of viscosity on the dissolution kinetics of CA6 particles.

The composition of cooled bulk slags except slag S7 was measured using inductively coupled plasma optical emission spectroscopy (ICP-OES). Slag S7 was prepared by melting 0.0063 g MgO powder in 0.1500 g slag S1 at 1600°C within a platinum crucible (5 μ m in diameter and 6 μ m in height) using HT-CLSM for 30 min under an argon atmosphere. Its composition was measured via SEM-EDS. The viscosities of all eight slags were calculated using Urbain model [18], which has been widely employed to determine the viscosity of steelmaking slags based on the function of each oxide component on the slag structures.

Table 5.1 List of slag composition used in the experiments

Slag	slag composition wt.%				C/A ratio	μ (Pa.s)	Particle	$\Delta C_{Al_2O_3}$ (kg/m ³)
	CaO	Al ₂ O ₃	SiO ₂	MgO				
S1	28.9	31.8	39.3	0.0	0.9	4.4	CA6	606
S2	38.3	20.7	41.1	0.0	1.8	2.8	CA6	887
S3	49.1	13.0	37.9	0.0	3.8	1.2	CA6	372
S4	48.0	36.0	16.0	0.0	1.3	0.9	CA2	694
							CA6	227
S5	45.4	34.4	16.3	4.0	1.3	0.8	CA2	819
							CA6	707
S6	43.3	32.7	16.1	8.0	1.3	0.7	CA2	959
							CA6	114
S7	27.6	30.8	37.6	4.0	0.9	3.3	CA6	521
S8	39.5	44.1	8.5	8.0	0.9	0.7	CA2	688

5.2.2 Experimental Procedure

An HT-CLSM (VL2000DX-SVF17SP, Yonekura) was used to carry out the CA2 and CA6 particles dissolution and interrupted experiments, enabling continuous in-situ observation. Technical details and operation procedures for the HT-CLSM facility are available elsewhere [19, 20]. The CA2 and/or CA6 particle dissolution experiments were conducted as follows: approximately 0.15 g of slag was pre-melted in a platinum crucible (5 μ m in diameter and 6 μ m in height) within the HT-CLSM furnace. A CA2 or CA6 particle was then placed on top of the pre-melted slag, and the assembly was heated to the experimental temperature according to a specified heating profile. The entire dissolution process of the CA2 and CA6 particles was recorded in real-time using a CCD camera at a frame rate of 5 Hz. It should be noted that the mass of the CA2 or CA6 particle used in each dissolution experiment is less than 0.1% of that of slag to avoid changing slag composition and properties. Post-experimentation, the ImageJ [21] software was used to measure the changes in the projection area (A) of the dissolving CA2 and CA6 particles. A was measured manually based on the contrast difference between the particle and molten slag. Each image was measured three times, and the average values were reported.

Fig. 5.2 illustrates the schematization of the sample setup and the heating profile. The CA2 or CA6 particle and platinum crucible containing pre-melted slag were placed in an alumina crucible positioned on a sample holder. A B-type thermocouple at the base monitored the temperature (**Fig. 5.2(a)**). Each dissolution experiment followed the same heating profile (**Fig. 5.2(b)**), including a rapid heating rate of 1000°C/min to 1500°C, followed by 50°C/min until reaching the test temperature of 1550°C. The start time of dissolution, t_0 , was defined as when the CA2 or CA6 particle was seen to be fully immersed into the molten slag at the test temperature. The experiment continued until the particle had fully dissolved.

Interrupted dissolution experiments were performed on three CA6 particles in slag: S3 after 60 s and 600 s, and S6 after 10 s, respectively. The system was then quenched using helium (**Fig. 5.2(b)**). The samples obtained from the interrupted experiments were grounded and polished for electron microscopy. SEM-EDS analysis (with carbon coating, 15 nm thickness) was performed using a JEOL 6610 LV to characterize the CA6 particle – slag interface.

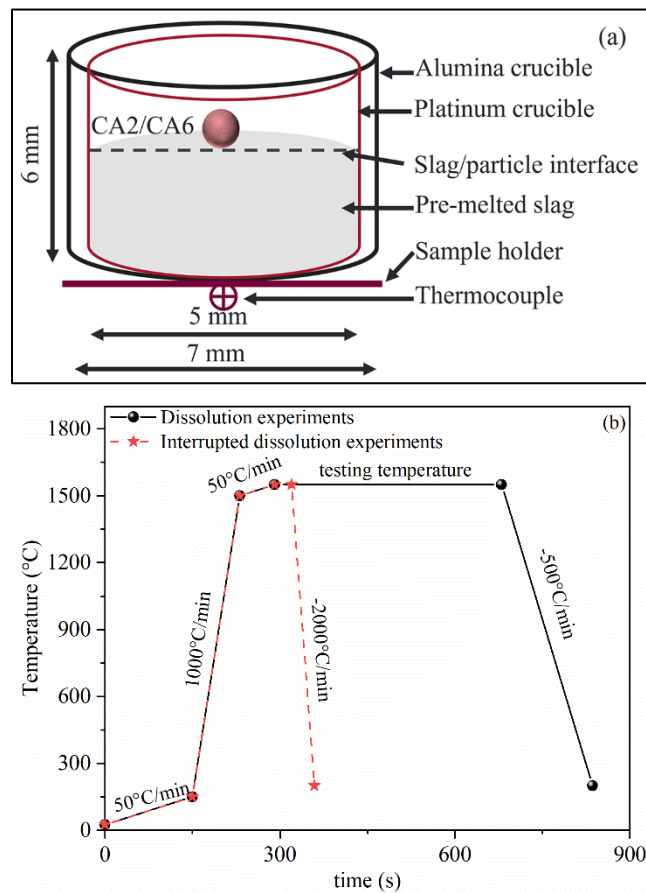


Figure 5.2 Schematic illustration of a) sample setup and b) the heating profiles used in dissolution and interrupted experiments

5.3. Results and Discussions

This section begins with the thermodynamical analysis of CA2 and CA6 particles dissolution in slags at 1550°C using the Phase Diagram module of FactSage 8.0 with FToxid database [22]. The objective of Section 5.3.1 is to better understand the influence of slag composition on the dissolution paths of CA2 and CA6 particles and predict potential stable phases. Section 5.3.2 provides experimental results on the impacts of slag viscosity, C/A ratio, and MgO content on the dissolution kinetics of CA2 and CA6 particles. The underlying mechanisms of these effects are analyzed and discussed. In Section 5.3.3, the dissolution paths of CA6 in slag S3 and S6 are determined. A comparison of the dissolution paths between the thermodynamic predictions (calculations) and the experimental observations incorporating SEM-EDS analysis of particle – slag interface is presented, providing the formation mechanisms of the intermediate solid products. Building on both thermodynamic predictions and experimental results, Section 5.3.4 proposes two different dissolution mechanisms of solid particles and evaluates their impact on the dissolution kinetics. Finally, Section 5.3.5 provides a brief discussion on slag selection considerations for optimizing NMIs removal while balancing refractory service life.

5.3.1 Thermodynamics analysis

Fig. 5.3 compares the phase changes with respect to MgO content in slag phase, including the ternary phase diagram for CaO-Al₂O₃-SiO₂ (**Fig. 5.3(a)**), the pseudo-quaternary phase diagram 4 wt.% MgO-CaO-Al₂O₃-SiO₂ (**Fig. 5.3(b)**) and 8 wt.% MgO-CaO-Al₂O₃-SiO₂ (**Fig. 5.3(c)**). These diagrams highlight the compositions of CA2 and CA6 particles, the initial compositions of the eight slag groups, and potential phase zones. Additionally, black solid lines represent two-phase tie lines, while red dashed and solid arrows denote the expected dissolution paths of CA2 and CA6 particles in the eight slags.

Although the particle dissolution is inherently a non-equilibrium process and the dissolution path may not follow a straight trajectory, the phase diagrams provide valuable insights into the phases that may precipitate near the CA2 and CA6 particles during dissolution. Notably, the initial compositions of all eight slags are located within the fully liquid region of the phase diagrams, as shown in **Fig. 5.3**.

Fig. 5.3(a) presents the expected dissolution paths of CA6 particles in slag S1 - S4 and CA2 particles in slag S4. The expected dissolution paths of CA6 particles in slag S1 and S2 do not intersect phase zones a₂ or a₃, suggesting that no intermediate solid products are likely to form.

Conversely, the dissolution paths of CA2 and CA6 particles in slags S3 and S4 traverse the phase zone containing melilite, suggesting potential precipitation on the particle surface.

Fig. 5.3(b) depicts the expected dissolution paths for CA6 particles in slag S5 and S7, and the dissolution path of CA2 particles in slag S5. For the dissolution of CA2 particles in slag S5, the dissolution path crosses phase zones b_2 and b_3 , predicting the formation of intermediate product like spinel (MA). Similarly, for CA6 particles in slag S5 and S7, the intermediate solid products like $2\text{CaO}\cdot 2\text{MgO}\cdot 14\text{Al}_2\text{O}_3$ (C2M2A14), $\text{CaO}\cdot 2\text{MgO}\cdot 8\text{Al}_2\text{O}_3$ (CM2A8), and MA are expected to form.

Fig. 5.3(c) illustrates the dissolution path of CA6 particles in slag S6 and CA2 particles in slag S6 and S8. For CA6 particles in slag S6, similar intermediate solid products (CA2, CM2A8, and MA) are expected as in slag S7. For CA2 particles, MA is the only predicted intermediate solid product in slag S6 and S8.

Generally, the formation of an intermediate solid product layer on the surface of a solid particle can impede the dissolution of particles by retarding the transport of products from and reactants to the particle surface [23]. Moreover, the formation of an intermediate solid layer around the undissolved particle would decrease the concentration difference (ΔC) of the dissolving species by changing the bulk slag and the particle – slag interface to solid product layer – slag interface, thereby reducing the ΔC for dissolution compared to systems without intermediate solid layer formation. [16] In the present study, the ΔC for CA2 and CA6 particles dissolution is assumed to be the concentration difference between the bulk slag and the saturation content for Al_2O_3 ($\Delta C_{\text{Al}_2\text{O}_3}$). This assumption is supported by the significantly small size and higher diffusion coefficient of Ca^{2+} cation compared to AlO_x^{y-} anion. [24]

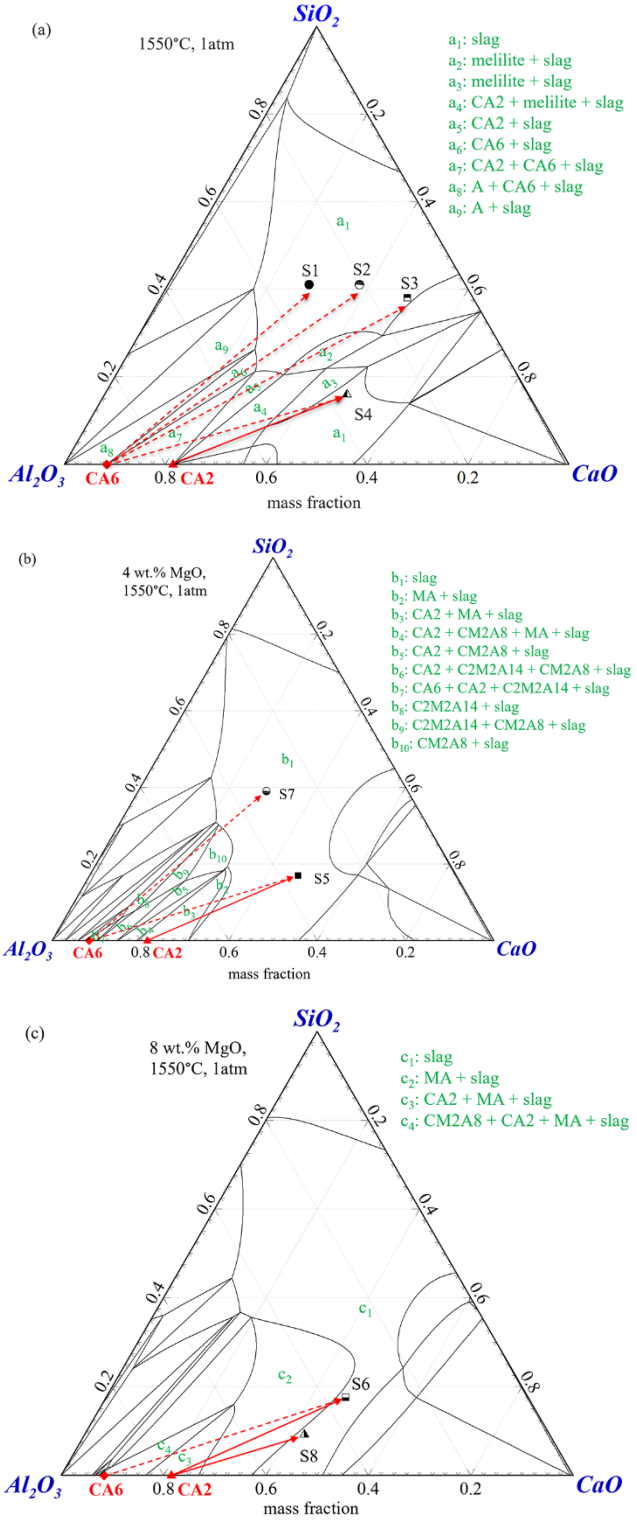


Figure 5.3 Prediction of phase stability of the CA2 and CA6 particles – CaO-Al₂O₃-SiO₂ based slag systems at 1550°C, (a) slag without MgO, (b) slag with 4wt.%MgO, and (c) slag with 8

wt.% MgO. Dash and solid arrows represent the dissolution path of CA6 and CA2 particles, respectively. (C: CaO, A: Al₂O₃, S: SiO₂, M: MgO)

5.3.2 Dissolution kinetics parametric study

5.3.2.1 Effect of slag viscosity on the dissolution kinetics of CA6 particles

The influence of slag viscosity on the dissolution kinetics of CA6 was examined using slags, S1, S7, and S5, with similar $\Delta C_{Al_2O_3}$ and slag C/A ratio but varying slag viscosities. In slag S1 and S7, CA6 particles exhibited slow motion during the dissolution process, while in slag S5, the particle moved rapidly.

It is well known that the slag viscosity strongly relates to its structure at molten status. Polymer- and structure-based theories [25] suggest that the types and quantities of oxides influence the structure of slag, as these can function as either network formers or breakers. Slag oxides are typically classified into three categories. The first category, “acid oxides,” such as SiO₂, forms complex three-dimensional networks of anionic complexes. The second category, “basic oxides,” including CaO and MgO, disrupt these networks. The third category, “amphoteric oxides,” exemplified by Al₂O₃, exhibits behavior that varies depending on the slag composition and lacks a distinct categorization. [25, 26]

To quantitatively describe the slag structure, the parameter Q , i.e. the degree of slag polymerization, was developed. [24] A higher Q value denotes that the structural unit within the slag is larger, leading to higher resistance for dissolving species transport in this molten slag. Decreasing the Q value from 4 to 0 is known to modify the slag structural unit from a 3D tetrahedra to a monomer. [24] For the CaO-Al₂O₃-SiO₂-MgO slag system, Q can be calculated using the following equations [24]:

$$Q = 4 - NBO/X_T \quad (1)$$

$$NBO = 2(X_{CaO} + X_{MgO} - 2X_{Al_2O_3}) \quad (2)$$

$$X_T = X_{SiO_2} + 2X_{Al_2O_3} \quad (3)$$

where NBO is the number of non-bridge oxygen atoms, X_T is the number of tetragonally-coordinated atoms, and X_i is the molar ratio of component i in the slag. The Q values for slag S1, S7, and S5 are 3.7, 3.5, and 2.6, respectively.

Fig. 5.4 presents the normalized area change of CA6 particles over time. The total dissolution time of CA6 particles decreased from 819 s to 432 s by decreasing the slag viscosity from 4.4 to

3.3 Pa·s, coupled with an increase in $\Delta C_{\text{Al}_2\text{O}_3}$ from 506 kg/m³ (15.5 wt.%) to 521 kg/m³ (16.1 wt.%). With a further decrease in the viscosity to 0.8 Pa·s, coupled with an increase in $\Delta C_{\text{Al}_2\text{O}_3}$ to 707 kg/m³ (20.5 wt.%), the total dissolution time dropped to around 36 s. Moreover, the reduction in Q values from 3.7 to 2.6 suggests a transformation in the slag structure from a sheet-like to a chain-like configuration. [24] This transformation decreased the transportation resistance for dissolving species in the molten slag and enhanced particles dissolution, consistent with previous studies. [13]

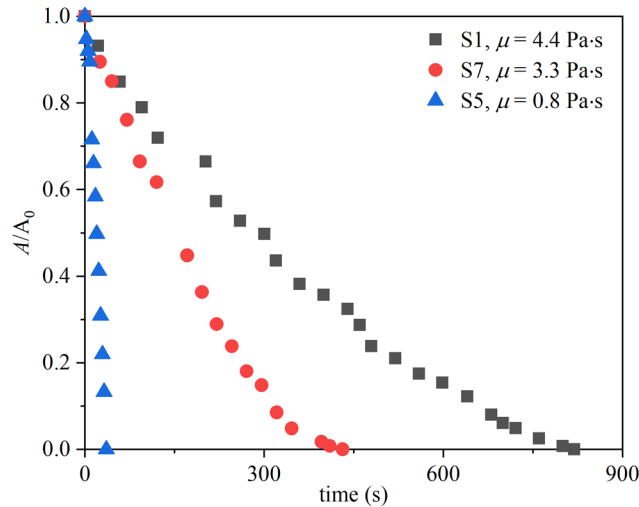


Figure 5.4 Normalized area changes of CA6 particles as a function dissolution time at 1550°C in slags with different viscosities

5.3.2.2 Effect of C/A ratio on the dissolution kinetics of CA6 particles

The influence of slag C/A ratio on the dissolution kinetics of CA6 particles was investigated in three slags with C/A ratios 0.9, 1.8, and 3.8, each possessing approximately 40 wt.% SiO₂ at 1550°C. Throughout the dissolution process, CA6 particles exhibited slow motion in all three slags.

Fig. 5.5 shows the normalized area change of CA6 particles with time. The total dissolution time of CA6 particles was initially dropped from 819 s to 174 s by increasing the C/A ratio from 0.9 to 1.8. This decrease can be attributed to a reduction in slag viscosity from 4.4 to 2.8 Pa·s, coupled with an increase in $\Delta C_{\text{Al}_2\text{O}_3}$ from 506 kg/m³ (15.5 wt.%) to 912 kg/m³ (28.7 wt.%). However, with a further increase in the C/A ratio to 3.8, the total dissolution time unexpectedly increased to 1001 s despite a further reduction in slag viscosity to 1.2 Pa·s. Even though there is a drop in $\Delta C_{\text{Al}_2\text{O}_3}$ to 793 kg/m³ (26.5%), this increase is likely due to the potential formation of intermediate solid product melilite, as predicted by the phase diagram in Section 3.1. Similar

dissolution behaviors have been reported by the current authors [13] for the dissolution of CA2 particles in those three slags at 1550°C.

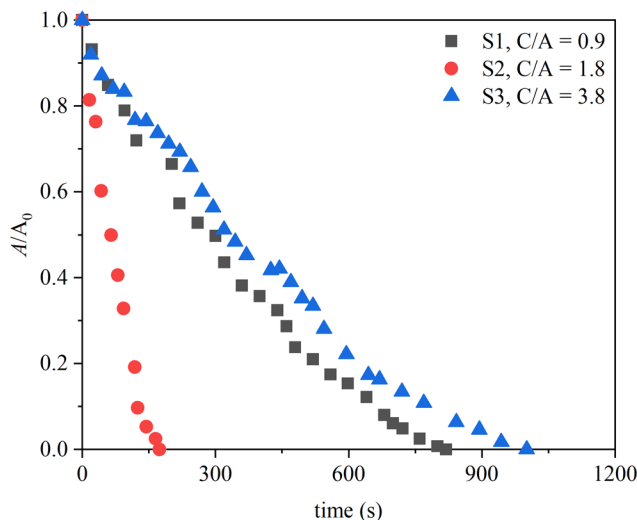


Figure 5.5 Normalized area changes of CA6 particles as a function of time at 1550°C in slags with different C/A ratios

5.3.2.3 Effect of MgO content on dissolution kinetics of CA2 and CA6 particles

The influence of MgO content on the dissolution kinetics of CA2 and CA6 particles was analyzed at 1550°C in three slags with MgO content of 0, 4, and 8 wt.%. Those slags had a similar C/A ratio of 1.32 and a similar SiO₂ content of 16%.

Fig. 5.6 illustrates the normalized area change of CA2 particles as a function of time. The total dissolution time of CA2 particles decreased from 47 s to 17 s with an increase of MgO content from 0 (slag S4) to 8 wt.% (slag S6). This trend is attributed to the combined effects of an increase in $\Delta C_{Al_2O_3}$ from 694 kg/m³ (19.7 wt.%) to 959 kg/m³ (27.0 wt.%), a reduction in slag viscosity from 0.9 to 0.7 Pa·s, and a decrease in Q from 2.97 to 2.56.

Slag S8 with 8 wt.% MgO (red circle in **Fig. 5.6**) and slag S4 without MgO (solid red circle in **Fig. 5.6**), had similar $\Delta C_{Al_2O_3}$ (690 kg/m³), were compared to examine the specific influence of MgO content on the dissolution kinetics of CA2 particles. Additionally, the Q values are comparable for S4 (3.0) and S8 (3.1). The total dissolution time of CA2 particles decreased from 47 s to 22 s by increasing the MgO content from 0 to 8 wt.%. The slight reduction in slag viscosity from 0.9 to 0.7 Pa·s is unlikely to contribute this improvement. By comparing the dissolution paths of CA2 particles in slags S4 and S8, shown in **Fig. 5.3(a)** and **(c)**, it is seen that the intermediate solid product MA only forms during CA2 particle dissolution in slag S8. The current authors claim

that the formation of MA phase positively impact the dissolution kinetics, contrasting the role of melilite in slag S3 for CA2 dissolution reported in [13]. This comparison suggests the formation of intermediate solid products might have different impacts on the dissolution kinetics of particles. More discussions were given in Section 5.3.4.

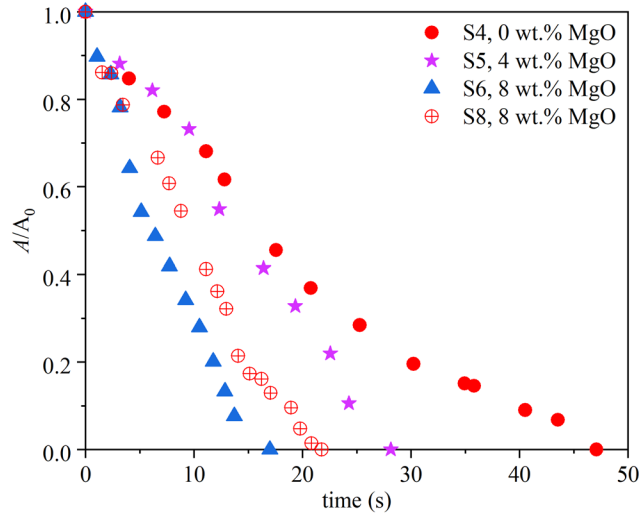


Figure 5.6 The normalized area changes of CA2 particles as a function dissolution time at 1550°C in slags S4-S6 with different MgO contents but same C/A ratio, slags S4 and S8 with different MgO contents but similar $\Delta C_{Al_2O_3}$

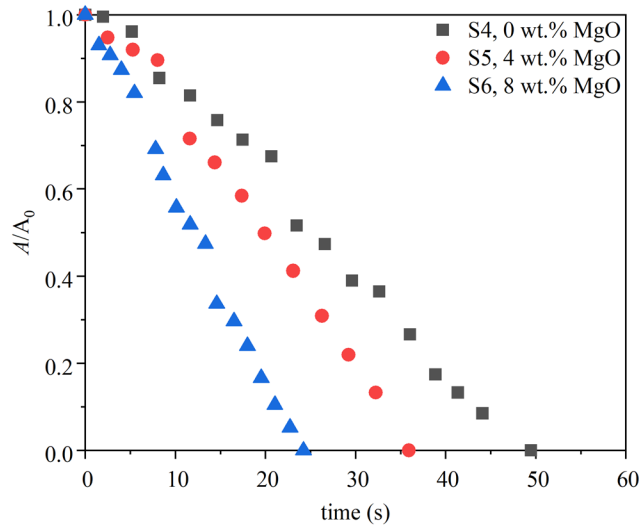


Figure 5.7 The normalized area changes of CA6 particles as a function dissolution time at 1550°C in slags with different MgO contents

CA6 particles moved and rotated in all three molten slags during the dissolution process. **Fig. 5.7** shows the normalized area change of CA6 as a function of time for slags with varying MgO

contents. The total dissolution time of CA6 decreased from ~49 s to ~36 s as the MgO content increased from 0 to 4 wt.%, due to the increase of $\Delta C_{\text{Al}_2\text{O}_3}$ (229 kg/m³ (6.8 wt.%) to 707 kg/m³ (20.5 wt.%)), combined with a slight decrease in slag viscosity from 0.9 to 0.8 Pa·s. Further increase in the MgO content to 8 wt.%, the dissolution time further decreased to 24 s. At this MgO content, the slag viscosity was slightly decreased to 0.7 Pa·s, while the $\Delta C_{\text{Al}_2\text{O}_3}$ dropped to 114 kg/m³ (3.6 wt.%). Moreover, an examination of the dissolution pathways indicated that the intermediate solid products were expected to form during CA6 dissolution in all three slags, as detailed in Section 5.3.1. This behavior suggests that factors, such as the formation of intermediate solid products, beyond $\Delta C_{\text{Al}_2\text{O}_3}$ and slag viscosity may influence the dissolution kinetics of the CA6 particles at high MgO content, or the formation of intermediate solid products might affect the prediction of $\Delta C_{\text{Al}_2\text{O}_3}$ using FactSage 8.0 [22]. More discussions were given in the following sub-section.

5.3.3 Determination of dissolution path

To gain deeper insights into the impact of the dissolution path of CA2 and CA6 particles on the dissolution kinetics, the interrupted dissolution experiments for CA6 particles were performed in slag S3 after 60 s and 600 s, and in slag S6 after 10 s dissolution, respectively. SEM-EDS analysis was conducted along the CA6 particle – slag interface, and the results were analyzed in conjunction with thermodynamic calculations using FactSage 8.0 [22]. The results are presented in **Figs. 5.8 – 5.11**. Moreover, the potential chemical reactions forming the intermediate solid products, indicated by phase diagrams and SEM-EDS results, during those dissolution processes were obtained using Reaction module of FactSage 8.0 with FToxid database [22], as listed in **Table 5.2**. From the thermodynamic point view, the free Gibbs energy of each reaction at 1550°C is negative, indicating all those reactions can happen at experimental conditions. It also can be found that the reaction constant, K_{eq} , at equilibrium condition for Reactions (2), (4 – 6), and (8 – 10) is much greater than that of Reactions (1), (3) and (7), showing Reactions (2), (4 – 6), and (8 – 10) are much faster compared to that of Reactions 1, 3 and 7 under the same experimental conditions.

Fig. 5.8(a) shows the in-situ image of the CA6 particle dissolving in slag S3 at 1550°C after 600 s. The undissolved particle is outlined by a red dash boundary. A surrounding layer, visible between the solid black line and red dash line, exhibits a semi-transparent appearance distinct from the opaque undissolved particle. This indicates the formation of a new product layer during the

dissolution process. A similar phenomenon has been reported by Liu et al. [10] for the dissolution of MgO particle in 29.9CaO-23.5Al₂O₃-39.3SiO₂-7.3MgO (wt.%) slag at 1600°C. Additionally, gas bubbles are visible on the surface of the undissolved particle, likely resulting from air trapped within the pores of the CA6 particle.

Table 5.2 A list of potential chemical reactions for the formation of intermediate solid products during CA2 and CA6 particles' dissolution process in molten slags. These reactions are calculated using Reaction module of FactSage 8.0 with FToxid database [22]

Reactions	$\Delta G = a + bT$ (1573 \sim T = 1823 K	
	2273K)	ΔG (J) K_{eq}
1 (CA6) _s + (C) _l = 2(CA2) _s + 2(A) _l	97,340-90.65T	-432056 17.29
2 (CA6) _s + 2(C) _l = 3(CA2) _s	-212,831+11.39T	-195375 3.96E5
3 (CA6) _s + (C) _l + (S) _l = (C2AS) _s + 5(A) _l	328,603-213.14T	-1529 1.11
4 (CA2) _s + (C) _l + (S) _l = (C2AS) _s + (A) _l	-78,909-20449.01T	-110494 1.46E3
5 (CA6) _s + (C) _l + 2(M) _l + 8(A) _l = (C2M2A14) _s	-1E6+499.49T	-495875 1.61E14
6 2(CA6) _s + 2(M) _l + 2(A) _l = (C2M2A14) _s	-551,979+204.75T	-234741 5.31E6
7 (A) _l + (M) _l = (MA) _s	-115,132+26.59T	-542956 35.94
8 (C2M2A14) _s + 2 (M) _l + 2(A) _l = 2(CM2A8) _s	-442,000+144.61T	-105900 1.08E3
9 (CA6) _s + 2(M) _l + 2(A) _l = (CM2A8) _s	-496,990+174.68T	-226376 3.06E6
10 (CM2A8) _s + 6(M) _l = 8(MA) _s + (C) _l	-306,316+37.71T	-276388 8.29E7

C: CaO, A: Al₂O₃, S: SiO₂, M: MgO. The subscript s and l denote the solid and liquid state of the phases, respectively.

Figure 5.8(b) illustrates the SEM backscattered electron image of the CA6 particle – slag S3 interface after 600 s dissolution, highlighting three distinct regions based on variations in contrast and line scan results (as described above). The white region beyond the solid black line corresponds to slag S3, the gray region between the solid black line and the red dashed line represents the intermediate solid product melilite, and the dark gray region within the red dashed boundary contains a mixture of undissolved CA6 particle, melilite, CA2 and slag. These features align well with the morphology observed in the in-situ image (**Fig. 5.8(a)**). The apparent shape difference between the particle in the in-situ image and the SEM image arises from the projection

area captured in the in-situ image, while the SEM image reflects the actual cross-sectional shape after polishing. Note that in some circumstances, over-polishing can lead to shape alterations in the sample.

To provide a clearer view of the interface, a localized area spanning the three regions, marked by a white dashed boundary in **Fig. 5.8(b)**, was magnified to 1000X (**Fig. 5.8(c)**). The magnified image distinctly highlights the color differences between the regions, revealing gray areas within the black region. The SEM-EDS point analysis, presented in **Table 5.3**, indicates that spectra 1 and 3 in the white region match the elemental composition of slag S3, confirming it as the bulk slag. The gray regions (spectra 2, 4 – 6, and 10) align with the composition of melilite, while spectra 8 and 11 in the black region correspond to the CA2 phase. Moreover, spectra 7 and 9 in the light black region indicate a mixture of these phases. The results suggested that molten slag, penetrated through the pores of CA6, formed new phases of melilite and CA2 through Reactions 1 – 4.

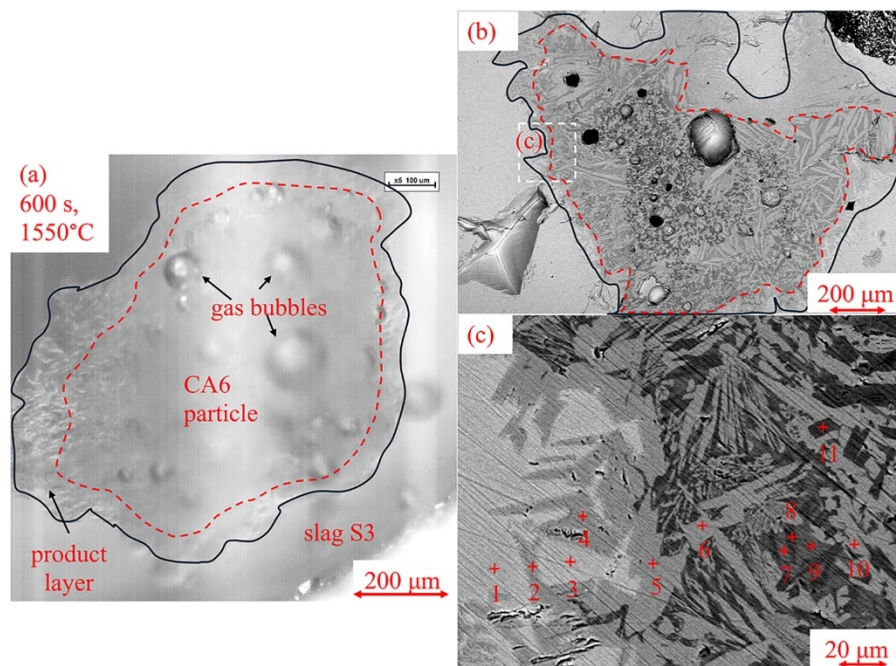


Figure 5.8 Images showing the formation of distinct phases during CA6 particle dissolution in slag S3 at 1550°C after 600 s. (a) in-situ image, and (b-c) SEM back scattered electron images

To accurately interpret the line scan results and with respect to the dissolution path, a systematic approach was employed to distinguish between the CA6 particle, slags (S3, S6), and intermediate solid products (C2AS (melilite), CA2, MA, and CM2A8). Each of these compounds has a distinct elemental composition, as summarized in **Table 5.4**. Thus, the SEM-EDS line scan data along the

particle – slag interface were compared with the theoretical compositions of those potential compounds. Regions along the scanned line were identified as particle, slag, intermediate solid products or mixture based on their elemental composition. For example, in the CA6 particle – slag S3 system, the non-Si regions, with Al and Ca constituting ~48 and ~6 wt.% at the particle – slag interface, can be classified as CA6, while regions where Ca, Al, and Si coexist, with Ca, Al and Si constituting ~30, ~20 and ~10 wt.%, can be identified as melilite. Boundary layers are regions having a decreasing Ca and Si composition while the Al content steadily increases. The regions where Ca, Al, and Si coexist, with Ca and Si constituting ~34 and ~17 wt.% can be classified as slag S3. The other regions can be considered as mixtures.

Table 5.3 SEM-EDS point scan results along CA6 – slag S3 interface in **Fig. 5.8(c)**

Spectrum	Elemental Composition (wt.%)			Phases
	Ca	Al	Si	
1	32	11	17	slag S3
2	29	19	12	melilite
3	31	10	17	slag S3
4	29	17	13	melilite
5	28	20	11	melilite
6	29	20	11	melilite
7	4	38	16	mixture
8	16	41	1	CA2
9	14	24	18	mixture
10	28	20	11	melilite
11	15	40	2	CA2

Fig. 5.9 presents the SEM backscattered electron image, and the elements Ca, Al, and Si distribution obtained from the EDS line scan of the CA6 particle – slag S3 interface after 60 s (**Fig. 5.9(a)** and **(b)**) and 600 s (**Fig. 5.9(b)**) of dissolution at 1550°C, respectively. Following the defined criteria, different regions were identified. In **Fig. 5.9(a)**, the dark-gray region in the center of SEM image presented undissolved particle whereas light gray outer region was slag S3. New phases, such as CA2 and melilite, were identified between these two regions. This finding is in good agreement with the thermodynamic predictions shown in **Fig. 3(a)**. Due to relatively high porosity of the CA6 particle, slag S3 was able to penetrate towards the core of particle through the pores. No boundary layer observed between the intermediate solid products and the undissolved particle,

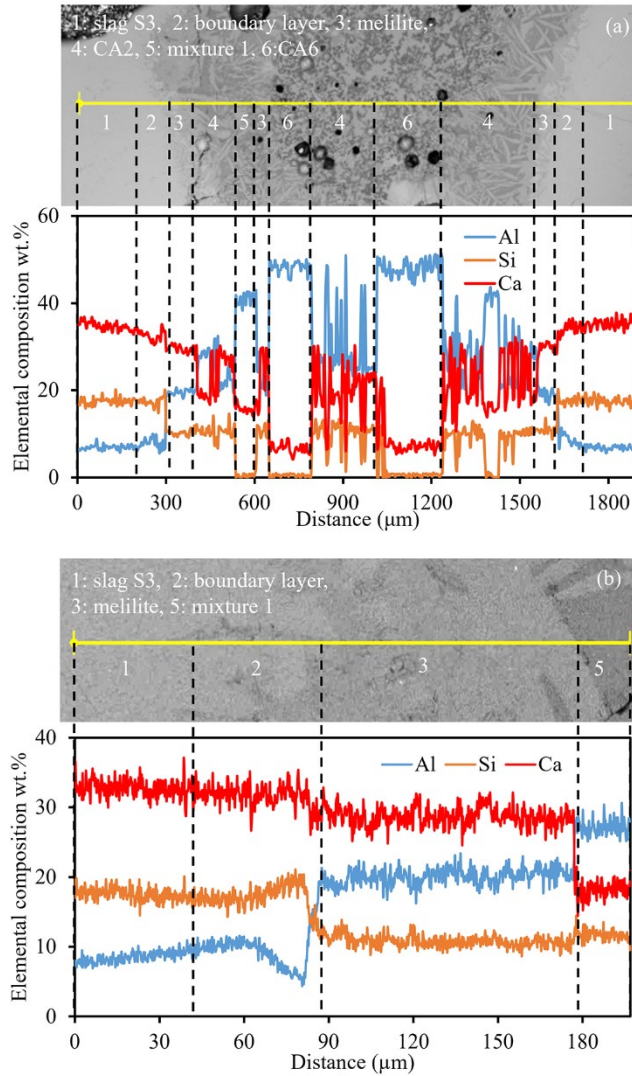
indicating the mass transfer of the dissolving species through the intermediate solid layer was not the rate-limiting step for CA6 particle dissolution. However, a boundary layer between slag S3 and the melilite was identified in **Fig. 9(a)**, though not clearly visible due to the long scan distance. To clarify this, a localized short line scan along the slag S3 – melilite layer was conducted (**Fig. 9(b)**), revealing a distinct boundary layer based on the Al and Si contents distribution. Interestingly, the Al content initially increased, then dropped to a content lower than that in the bulk slag before rising to match that of melilite, while the Si content increased before decreasing to a content similar as that in the melilite. This differs from the continuous elements distribution trend observed for CA2 particle dissolution in 30.5CaO-23.2Al₂O₃-46.3SiO₂ (wt.%) slag [12], and Al₂O₃ particle dissolution in CaO-MgO-SiO₂-Al₂O₃-TiO₂ slags [27]. The observed Al drop at the melilite – boundary layer interface is likely due to the growth of melilite on this side by consuming Al, which results in Si enrichment.

Table 5.4 Elemental composition of CA6 particle, slags, and relevant intermediate solid products

	Elemental composition (wt.%)			
	Ca	Al	Si	Mg
CA6	6	48	0	0
Slag S3	34	7	17	0
Slag S6	30	18	7	5
CA2	15	42	0	0
MA	0	38	0	17
C2AS	29	20	10	0
CM2A8	4	45	0	5
C2M2A14	5	47	0	3

A similar trend was observed for CA6 particle in slag 3 after 600 s dissolution, as shown in **Fig. 5.9(b)**. However, the melilite layer is noticeably thicker compared to that observed after 60 s dissolution, suggesting its accumulation over time during the dissolution process. It is important to note that the CA2 and CA6 regions primarily consist of CA2 and CA6, respectively, but also contain minor amounts of other phases due to the penetration of molten slag through the pores.

In summary, SEM-EDS analysis confirmed that the formation of a new intermediate solid phase as predicted by the thermodynamic calculations is melilite, presented in the form of solid layer. This solid layer around the undissolved particle reduced the dissolution rate of CA6 particle in slag S3 by inhibiting the transport of species and reducing $\Delta C_{Al_2O_3}$ by altering the interface from slag – particle to slag – intermediate solid layer, significantly slowing dissolution kinetics.



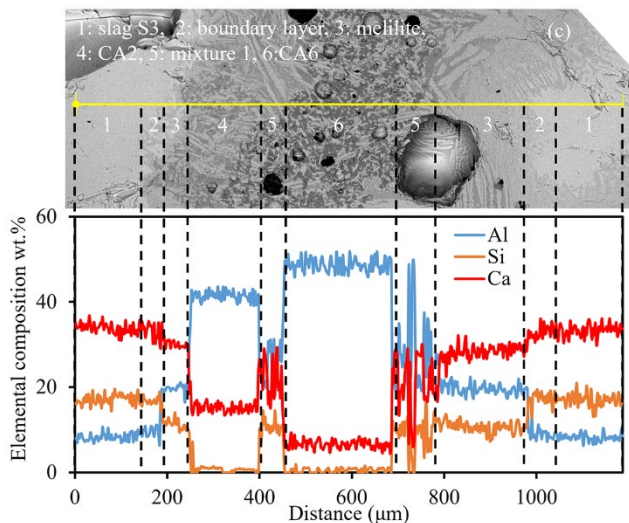


Figure 5.9 Figure 9 SEM backscattered electron image and EDS line scan analysis of CA6 particle – S3 slag interface (a) through the entire undissolved particle and (b) at the slag – product layer interface after 60 s dissolution, respectively, and (c) through the entire undissolved particle after 600 s dissolution at 1550°C. Mixture 1 contains CA6 + CA2 + melilite + slag S3

Fig. 5.10(a) shows the in-situ image of CA6 particle dissolved in slag S6 at 1550°C after 10 s. The region enclosed by the red dash boundary represents the undissolved particle. Surrounding this, a distinct layer can be observed between the solid black line, which is suggested to be the boundary layer by the line scan results in **Fig. 5.11**. In addition, gas bubbles were observed on the surface of the undissolved particle, likely resulting from air trapped in the particle pores.

As shown in **Fig. 5.10(b)**, the interface between the CA6 particle and slag S6 after 10 s of dissolution at 1550°C can be divided into three distinct regions based on SEM backscattered imaging and EDS analysis: the white region outside the solid black line corresponds to slag S6, the gray region between the solid black line and red dashed line represents the boundary layer, and the light black region enclosed by the red dashed line denotes the undissolved particle.

SEM-EDS points and map scans were conducted on magnified areas crossing these regions (**Figs. 5.10(c)** and **(d)**). The point scan results (**Fig. 5.11(c)**, **Table 5.5**) show that spectra 2, 8, 10, and 11 align with the elemental composition of CA6, confirming that the dark regions are undissolved CA6 phase. Adjacent spectra, such as points 1, 7, and 9, match the CA2 phase composition, indicating the formation of CA2 as a reaction product of CA6 with slag S6 (via Reactions (1) and (2)). In addition, spectra 3 and 4 identify MA in the deep black regions near the CA2 phase, formed through Reactions (8) and (10). Further analysis reveals that spectra 5, 6, and

12 correspond to a mixture of molten slag and potential solid products, while spectra 13 and 14 in the outermost region confirm the presence of slag S6. Notably, CM2A8 phase was not detected, possibly due to (a) its content being below the detection limit or (b) its rapid consumption through subsequent Reaction (10). The SEM-EDS map scan of another region (**Figs. 5.11(e)**) further corroborates these findings. The elemental distributions observed in the map scan confirm the compositions and spatial arrangements of CA6, CA2, MA, and slag S6, consistent with the results of point and line scans.

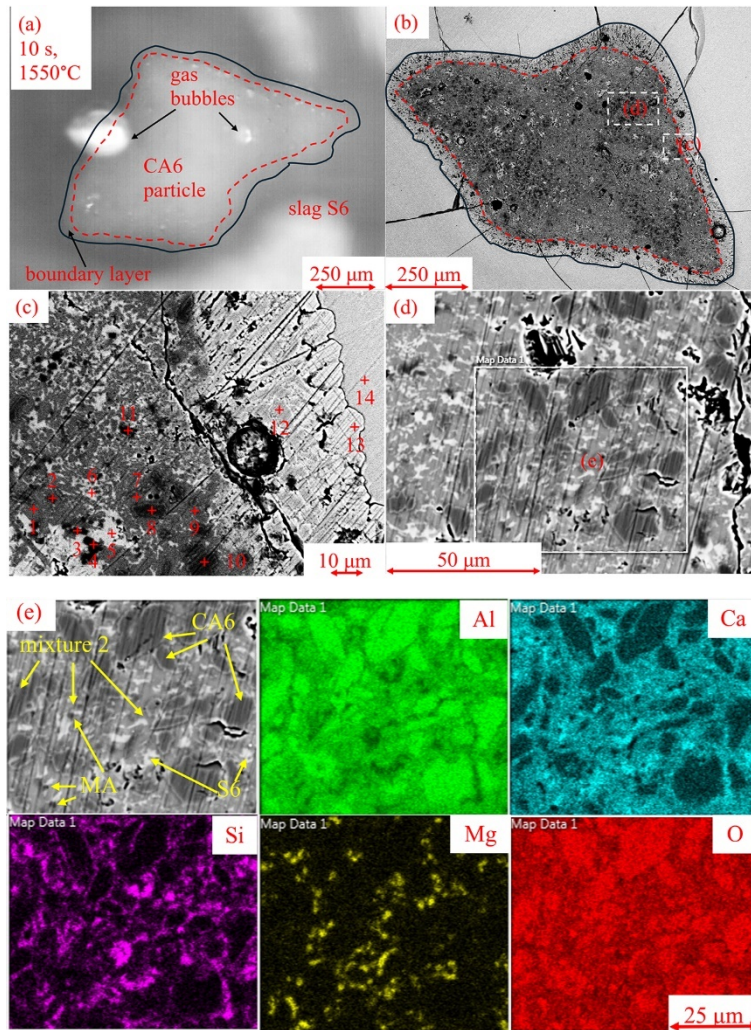


Figure 5.10 SEM back scattered electron image and EDS line scan analysis of CA6 particle – slag S6 interface after 10 s dissolution at 1550°C. Mixture 2 contains CA6 + CA2 + MA + slag

S6

To gain deeper insight into the dissolution mechanism, the SEM-EDS line scan was done along the CA6 particle – slag S6 interface after 10 s of dissolution at 1550°C. **Fig. 5.11** presents the SEM backscattered electron image, and the elements Ca, Al, Si, and Mg distribution obtained from the line scan, revealing distinct regions along the interface. On the left side of the scanned line, slag S6, followed by a boundary layer of about 80 μm. Beyond this layer, a mixed region is observed, characterized by fluctuations in elemental concentrations and comprising CA6, CA2, MA, and slag S6. This finding aligns well with the points scan results at other regions of this interface.

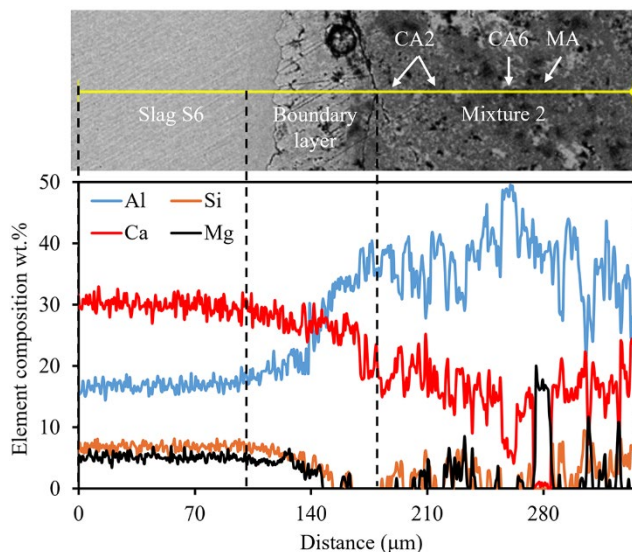


Figure 5.11 SEM back scattered electron image and EDS line scan analysis of CA6 particle – slag S6 interface after 10 s dissolution at 1550°C. Mixture 2 contains CA6 + CA2 + MA + slag S6

Based on the above analysis, the dissolution behavior of CA6 particles in slag S6 can be summarized as follows. Initially, a distinct boundary layer formed between the particle and the bulk slag. As slag penetrates through porous CA6 particle, they reacted and produced intermediate solid products of MA, and CA2. These products occurred in small amounts, had a small size, and were randomly dispersed. Due to their small size, the particles didn't obstruct the transport of reactants to the CA6 particle – slag S6 interface, maintaining the slag – particle interface rather than forming a new intermediate solid product – slag interface, unlike the dissolution behavior of CA6 particle determined in slag S3, where the intermediate solid product layer (melilite) formed around the particle. They were considered not to hinder the dissolution of CA6 particles. As a

result, the $\Delta C_{\text{Al}_2\text{O}_3}$ was not affected by the precipitation of these products on the particle surface. This finding highlights the importance of where the solid products form and clarifies the differences between dissolution experimental results. It also confirmed that the limitation of thermodynamic model prediction on $\Delta C_{\text{Al}_2\text{O}_3}$, especially for the presence of intermediate solid products.

Table 5.3 SEM-EDS point scan results along CA6 particle – slag S6 interface in **Fig. 5.10(c)**

Spectrum	Elemental Composition (wt.%)				Phases
	Ca	Al	Si	Mg	
1	14	40	1	2	CA2
2	6	48	0	0	CA6
3	0	38	0	17	spinel
4	1	38	0	17	spinel
5	26	26	6	1	mixture
6	27	25	7	1	mixture
7	17	41	0	0	CA2
8	6	48	0	0	CA6
9	16	42	0	0	CA2
10	6	49	0	0	CA6
11	6	49	0	0	CA6
12	26	34	0	0	CA
13	29	21	6	4	slag S6
14	29	19	7	5	slag S6

5.3.4 Dissolution mechanisms of particles in molten slags

Based on the detailed analysis of CA2 and CA6 particles dissolution in different slags, two distinct dissolution mechanisms have been identified for the dissolution of solid particles, corresponding to three types of behavior schematically illustrated in **Fig. 12(a)-(c)**, as well as the concentration profile of the dissolving species in **Fig. 12 (a1)-(c1)**. The dissolution process can generally be categorized into two types: (1) direct dissolution and (2) indirect dissolution.

Direct dissolution

As shown in **Fig. 12(a)**, the particle dissolves directly into the molten slag, with its size gradually decreasing until it is fully dissolved. A boundary layer forms at the interface once the particle is immersed in the molten slag. Reactants and products are transported across this boundary layer, making mass transport through the layer the rate-limiting step. Additionally, the driving force (ΔC) (concentration difference of the dissolving species between the particle – slag interface (C_s) and the bulk slag (C_b)) is constant ($\Delta C = C_s - C_b$) during the dissolution process (**Fig. 12(a1)**). CA6 particles dissolving in slags S1, S2, and S4 followed this mechanism.

Fig. 12(b) presented the second case of direct dissolution, where intermediate solid products formed during the dissolution process, presented as randomly dispersed and tiny particles around and within the undissolved particle, due to the chemical reactions between the slag and the solid particle, as depicted from t_0 to t_2 . Then they dissolved within the slag together with the undissolved particle, as shown from t_1 to t_4 . The formation of these types of products has no impact on the ΔC ($C_s - C_b$), as their amount is too small to change the C_b and the interface between solid particle – slag, as shown in **Fig. 12(b1)**. The dissolution of CA2 and CA6 in MgO-containing slags (S5, S6, S7, S8) is expected to result in the formation of intermediate products. Given that the dissolution occurred more rapidly in the presence of MgO, it can be inferred that the precipitation of these particles may further consume CA2 and CA6 through additional reactions alongside the dissolution process in the slag. While it would be premature to conclude that dissolution is accelerated by precipitation of the intermediate particles, they do not impede the dissolution process.

Indirect dissolution

Under this mechanism illustrated in **Fig. 12(c)**, once the particle is fully immersed into the slag, the formation rate of intermediate solid products exceeds their dissolution rate. As a result, these products grow and form a continuous solid layer around the particle, as indicated from t_0 to t_2 . This layer inhibits the transport of reactants and products, causing no boundary layer formed between the undissolved particle and intermediate solid layer. However, a boundary layer formed between the bulk slag and the intermediate solid layer. Additionally, as shown in **Fig. 12(c1)**, the formation of the intermediate solid layer significantly decreased the ΔC ($C_{s1} - C_b$) by altering the interface from slag – particle to slag – intermediate solid layer, significantly slowing the dissolution kinetics. CA2 particles [13] and CA6 particles dissolving in slag S3 followed this mechanism.

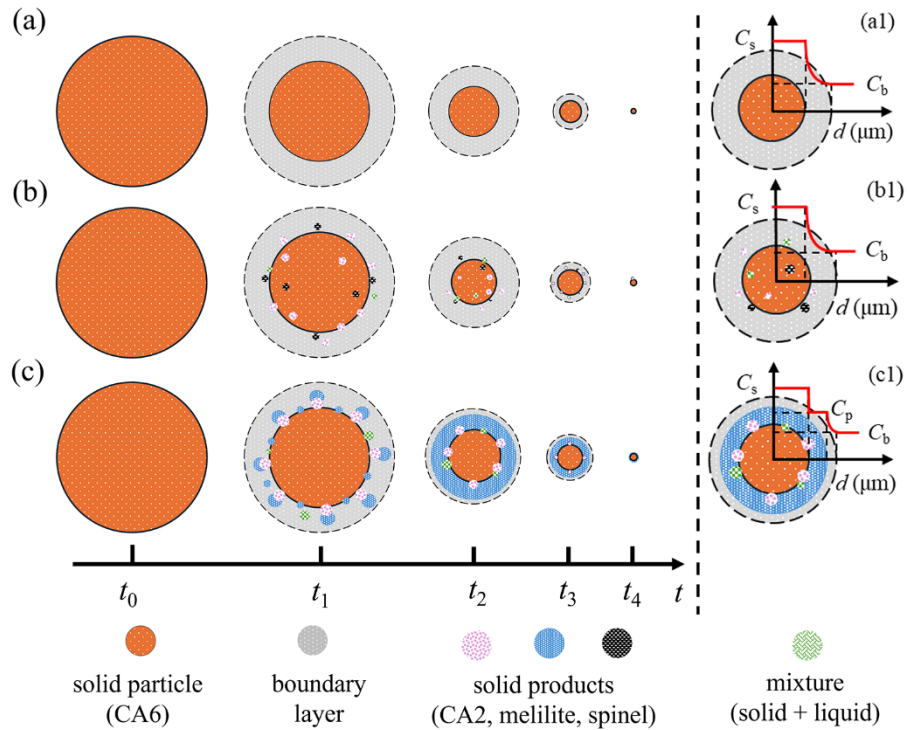


Figure 12 Schematic diagram for dissolution mechanism of solid particles in molten slag (a) Direct dissolution without intermediate solid products formation, (b) Direct dissolution with formation of intermediate solid products, and (c) Indirect dissolution. (a1)-(c1) present the concentration profile of the dissolving species corresponding to these dissolution mechanisms (C_s , C_p , and C_b donate the concentration of the dissolving species at particle – slag interface, in the solid product, and in bulk slag, respectively.)

5.3.5 Practical viewpoint for the steelmaking process

In steelmaking, a comprehensive understanding of the dissolution behavior of particles in steelmaking slags, particularly those formed as solid inclusions and used in refractories (e.g., CA2 and CA6), is crucial for enhancing steel cleanliness and extending refractory service life. To improve steel cleanliness, this study suggests that slags with a C/A ratio between 1 and 2, low SiO₂ content, and approximately 5 wt.% MgO are preferred. This composition promotes particle dissolution via the direct dissolution mechanisms, enhancing refining efficiency. Conversely, to extend refractory longevity, the indirect dissolution mechanism is desirable for interactions between molten slag and refractories. For instance, high C/A ratio slags promote the formation of a continuous solid product layer, which acts as a diffusion barrier. This slows the dissolution process, and prevents contamination, thereby preserving refractory performance.

5.4. Conclusions

This study systematically investigated the impacts of slag C/A ratio and slag viscosity on the dissolution kinetics of CA6 and CA2 particles at 1550°C in CaO-Al₂O₃-SiO₂-(MgO) metallurgical slags, utilizing HT-CLSM. Post-dissolution analysis through SEM-EDS and thermodynamic calculations provided insights into the dissolution path and mechanisms. Three distinct dissolution mechanisms were proposed based on these findings. The key conclusions are as follows:

(1) There are two distinct dissolution mechanisms of solid particles,

(a) *Direct dissolution*: 1) No intermediate solid products form, and the dissolution kinetics is controlled by the mass transport of species through the boundary layer. The driving force ($\Delta C_{\text{Al}_2\text{O}_3}$) is constant. 2) Irregular dispersed intermediate solid products formed during the dissolution process due to the chemical reactions between the molten slag and the particle. However, they do not have an impact on the ΔC and do not retard the dissolution kinetics of the particle.

(b) *Indirect dissolution with solid layer formation*: An intermediate solid layer forms around the particle, inhibiting the transport of species and reducing $\Delta C_{\text{Al}_2\text{O}_3}$ by altering the interface from slag – particle to slag – intermediate solid layer, significantly slowing dissolution kinetics.

(2) The impact of intermediate solid products on dissolution kinetics was strongly influenced by their morphology, whether they formed a solid layer or randomly dispersed intermediate solid particles. This morphological effect significantly influenced ΔC but was not fully captured in the thermodynamic modelling.

(3) An increase in the C/A ratio and a decrease in the viscosity of slag enhanced the dissolution rate of CA6 particles. However, it was observed the formation of a solid product layer (melilite) around the CA6 particle in slag with a C/A ratio of 3.8 acted as a hindrance, impeding its dissolution.

(4) The dissolution kinetics of CA2 and CA6 particles were improved with increased MgO content in slag.

Acknowledgments

The authors would like to thank the Natural Sciences and Engineering Research Council of Canada (NSERC) for funding this research. This research used a High Temperature Confocal Laser Scanning Microscopy-VL2000DX-SVF17SP funded by Canada Foundation for Innovation John Evans Leaders Fund (CFI JELF, Project Number: 32826), a scanning electron microscope JEOL 6610 located at the Canadian Centre for Electron Microscopy at McMaster University, and

a PANalytical X'Pert diffraction instrument located at the Centre for crystal growth, Brockhouse Institute for Materials Research.

Statements and Declarations

The authors declare that they have no known competing financial interests or personal relationships that could have appeared to influence the work reported in this paper.

Reference

- [1] Z.Y. Deng, M.Y. Zhu, Evolution Mechanism of Non-metallic Inclusions in Al-Killed Alloyed Steel during Secondary Refining Process, *ISIJ Int.*, 53 (2013) 450-458.
- [2] L. Holappa, O. Wijk, Inclusion Engineering, *Treatise on Process Metallurgy* 2014, pp. 347-372.
- [3] S. K. Michelic, C. Bernhard, Significance of Nonmetallic Inclusions for the Clogging Phenomenon in Continuous Casting of Steel—A Review, *Steel Res. Int.*, 93 (2022).
- [4] R. Salomão, V.L. Ferreira, L.R. Oliveira, A.D. Souza, W.R. Correr, Mechanism of pore generation in calcium hexaluminate (CA6) ceramics formed in situ from calcined alumina and calcium carbonate aggregates, *J. Eur. Ceram. Soc.*, 36 (2016) 4225-4235.
- [5] L.P. Pan, Y.W. Li, F.G. Tan, Q. Wang, Y.C. Chen, Q.H. Wang, T.B. Zhu, N. Liao, Y.B. Xu, Influence of calcium hexaluminate gradation on interfacial microstructure and fracture behavior of cement-bonded alumina castables, *Ceram. Int.*, 49 (2023) 16137-16148.
- [6] M.A. Braulio, G.G. Morbioli, D. H. Milanez, V. C. Pandolfelli, Calcium aluminate cement source evaluation for Al₂O₃–MgO refractory castables, *Ceram. Int.*, 37 (2011) 215-221.
- [7] H. Zhang, Y.B. Peng, S. Zhang, C.S. Liu, R.J. Cheng, H.W. Ni, Effects of Refining Slag on Transformation and Removal of Inclusions in Type 430 Stainless Steel, *Metall. Mater. Trans. B*, 53 (2022) 702-715.
- [8] J.S. Li, Y. Sun, S.F. Yang, W. Liu, Research Status of Numerical Simulation of Nonmetallic Inclusions Interfacial Removal, *steel res. int.*, 94 (2023).
- [9] M. Valdez, K. Prapakorn, A.W. Cramb, S. Sridhar, A study of the dissolution of Al₂O₃, MgO and MgAl₂O₄ particles in a CaO–Al₂O₃–SiO₂ slag, *Steel Res. Int.*, 72 (2001) 291-297.
- [10] J. Liu, M. Guo, P.T. Jones, F. Verhaeghe, B. Blanpain, P. Wollants, In situ observation of the direct and indirect dissolution of MgO particles in CaO–Al₂O₃–SiO₂-based slags, *J. Eur. Ceram. Soc.*, 27 (2007) 1961-1972.

- [11] G Wang, M. Nabeel, N.Dogan, M. Abid, W.Z. Mu, A.B. Phillion, Impact of porosity and velocity on the dissolution behaviors of calcium aluminate inclusions in CaO-SiO₂-Al₂O₃ steelmaking slag: in-situ observations and model advancements, in: M. University (Ed.)Metall.Mater.Trans. B, 2025.
- [12] K. Y. Miao, A. Haas, M. Sharma, W. Z. Mu, N. Dogan, In situ observation of calcium aluminate inclusions dissolution into steelmaking slag, Metall. Mater. Trans. B, 49 (2018) 1612-1623.
- [13] G. Wang, M. Nabeel, W.Z. Mu, A.B. Phillion, N.Dogan, In-situ confocal microscopy study on dissolution kinetics of calcium aluminate inclusions in CaO-Al₂O₃-SiO₂ type steelmaking slags, J. Iron Steel Res. Int., 32 (2025) 364-375.
- [14] B. Guo, J.J. Wang, L.F. Zhang, Dissolution Kinetics of Al₂O₃, CaAl₄O₇, and MgAl₂O₄ Inclusions Into CaO–Al₂O₃–SiO₂ Slags with Varying MgO Content, Metall. and Mater. Trans. B, (2024).
- [15] J.H. Park, I.H. Jung, H.G. Lee, Dissolution behavior of Al₂O₃ and MgO inclusions in the CaO–Al₂O₃–SiO₂ slags: Formation of ring-like structure of MgAl₂O₄ and Ca₂SiO₄ around MgO inclusions, ISIJ int., 46 (2006) 1626-1634.
- [16] X.L. Guo, J.V. Dyck, M.X. Guo, B. Blanpain, Phase evolution and nature of oxide dissolution in metallurgical slags, AIChE J., 59 (2013) 2907-2916.
- [17] J. Li, E.A Medina, J.K. Stalick, A.W. Sleight, M.A Subramanian, Structural studies of CaAl₁₂O₁₉, SrAl₁₂O₁₉, La_{2/3+δ} Al₁₂–δO₁₉, and CaAl₁₀NiTiO₁₉ with the hibonite structure; indications of an unusual type of ferroelectricity, Zeitschrift für Naturforschung B, 71 (2016) 475-484.
- [18] G. Urbain, Viscosité et structure de silicoalumineux liquides, Rev. Int. Hautes Temp. Refract., 2 (1974) 133-145.
- [19] H. Chikama, H. Shibata, T. Emland, M. Suzuk, “In-situ” real time observation of planar to cellular and cellular to dendritic transition of crystals growing in Fe–C alloy melts, Mater. Trans., JIM, 37 (1996) 620-626.
- [20] C. Orrling, Y. Fang, N. Phinichka, S. Sridhar, A.W. Cramb, Observing and measuring solidification phenomena at high temperatures, JOM-e, 51 (1999).
- [21] C.A Schneider, W.S. Rasband, K.W Eliceiri, NIH Image to ImageJ: 25 years of image analysis, Nat. Methods, 9 (2012) 671-675.

- [22] C.W. Bale, E. Bélisle, P. Chartrand, S.A. Deckerov, G. Eriksson, A.E. Gheribi, K. Hack, I.H. Jung, Y.B. Kang, J. Melançon, A. D. Pelton, S. Petersen, C. Robelin, J. Sangster, P. Spencer, M.A. Ende, Reprint of: FactSage thermochemical software and databases, 2010–2016, *Calphad*, 55 (2016) 1-19.
- [23] X.L. Guo, Z.H.I. Sun, J. V.Dyck, M.X. Guo, B. Blanpain, In situ observation on lime dissolution in molten metallurgical slags–Kinetic aspects, *Ind. Eng. Chem. Res.*, 53 (2014) 6325-6333.
- [24] V.D. Eisenhüttenleute, *Slag Atlas*, Slag Atlas, 3rd ed., V.D. Eisenhüttenleute, ed., Slag Atlas, 2nd ed., Verlag Stahleisen GmbH, Dusseldorf 1995.
- [25] D.R. Gaskell, The thermodynamic properties and structures of slags, *Metall. Treatises*, 6 (1981) 59-78.
- [26] M. Sajid, C.G. Bai, M. Aamir, Z.X. You, Z.M. Yan, X. X.M. Lv, Understanding the structure and structural effects on the properties of blast furnace slag (BFS), *ISIJ Int.*, 59 (2019) 1153-1166.

Chapter 6

Concluding remarks

This thesis focused on the understanding of the dissolution mechanisms and kinetics of solid calcium aluminate inclusions (CA2 and CA6) in metallurgical slags. To achieve this, a systematic study was conducted, including thermodynamic simulation using FactSage 8.0, in-situ dissolution experiments, as well as interrupted dissolution experiments via HT-CLSM. Post analysis was performed using SEM-EDS and ImageJ to examine the effects of temperature, slag composition, and porosity and velocity of the particles on the dissolution kinetics and mechanisms and dissolution paths of CA2 and CA6 particles. Additionally, the influence of intermediate solid product formation during the dissolution process on dissolution kinetics and mechanisms was explored. Moreover, a kinetic model incorporating the porosity and velocity of the particle was developed and validated by experimental data from the literature and this work.

6.1 Key Findings and Contributions

6.1.1 General Overview

Chapter 1 introduced the background and motivation behind the current thesis of studying the dissolution mechanisms and kinetics of CA2 and CA6 particles in metallurgical slags at steelmaking temperatures. Chapter 2 briefly introduced the secondary steelmaking, formation, and modification of non-metallic inclusions (NMIs), their flotation and separation to slag, and their impacts on production efficiency and product quality. The literature review specifically focused on the NMIs' dissolution via different experimental techniques, and numerical modeling. It also presented a brief description of slag structure and properties. The gaps in existing literature and key aspects in modeling of NMIs dissolution were also discussed.

Chapter 3 investigated the dissolution kinetics of CA2 particles in a synthetic CaO-Al₂O₃-SiO₂ steelmaking slag system using HT-CLSM. The effects of temperature (i.e., 1500, 1550, and 1600°C) and slag composition on the dissolution time of CA2 particles were studied, along with the time dependency of the projection area of the particle during dissolution. It was found that the

dissolution rate was enhanced by either an increase in temperature or a decrease in slag viscosity. Moreover, a higher CaO/Al₂O₃ (C/A) ratio led to an increased dissolution rate of CA2 particles at 1600°C. SEM-EDS analysis of as-quenched samples confirmed the dissolution path of CA2 particles in slags with C/A ratio at 1.8 and 3.8 and found the presence of solid product melilite on the surface of the CA2 particle which formed during dissolution in slag with C/A ratio at 3.8 at 1550°C. The formation of a melilite layer during the dissolution process was identified as a hindrance, impeding the dissolution of CA2 particles.

Chapter 4 investigated the dissolution behavior of CA2 particles in CaO-SiO₂-Al₂O₃ steelmaking slag at 1550°C, focusing on the less explored effects of particle porosity and motion. Laboratory-produced CA2 particles with two different porosity levels (0.08 and 0.20) were characterized using X-ray Computed Tomographic Imaging. A correlation between the porosity (ϕ) and the surface area ratio ($f(\phi)$) was proposed and expressed as $f(\phi) = e^{5.3469\phi}$. Moreover, in-situ observations highlighted the importance of particle motion during dissolution, prompting the development of a novel mathematical model incorporating both porosity and motion. The model predictions, validated against experimental data and literature, demonstrated that dissolution time decreased with an increase in particle velocity and porosity of particles and concentration difference of dissolving species between particle – slag interface and molten slag (ΔC) and a decrease in slag viscosity. Additionally, a sensitivity analysis of parameters influencing the total dissolution time was conducted.

Chapter 5, the kinetics and mechanisms of dissolution of CA2 and CA6 particles in CaO-Al₂O₃-SiO₂-(MgO) metallurgical slags at 1550°C were investigated using HT-CLSM. The effects of slag viscosity, CaO/Al₂O₃ (C/A) ratio, and MgO content on the dissolution time of CA2 and or CA6 particles were examined by tracking the time dependent changes of particle projection areas. Results showed that the dissolution kinetics of CA6 particles was enhanced by either an increase in slag MgO content and C/A ratio of slag or a decrease in slag viscosity, while the dissolution kinetics of CA2 particles was improved by increasing slag MgO content.

Chapter 5 also contributed to understanding the impacts of the dissolution paths and the formation of intermediate solid products on the dissolution kinetics and mechanisms of CA6 particles. It was found that a continuous intermediate solid melilite layer formed around the CA6 particle in slag

S3 with a CaO/Al₂O₃ ratio of 3.8, reducing its dissolution rate. Conversely, the formation of randomly dispersed intermediate solid fine products in the vicinity of the undissolved CA6 particle in slag S6 with 8 wt.% MgO did not impede their dissolution rate. Moreover, based on these findings, two distinct dissolution mechanisms were proposed, advancing the understanding of solid inclusion dissolution in metallurgical slags.

6.1.2 Specific Findings

The research objectives presented in Chapter 1 have now been achieved. The specific findings of the current study are as follows:

1. The CA2 particle behaviors, including motion, dissociation, and interaction with gas bubbles, have been observed during the experiments. The first two behaviors enhanced the dissolution of the CA2 particles while the interaction with the gas bubble slowed down dissolution. Similar motion behavior has been observed during the dissolution process of CA6 particles.
2. Increasing temperature from 1500 to 1600°C accelerated the average dissolution of CA2 particles by approximately 8 times in slag with a C/A ratio of 1. A similar trend was observed across different CaO-Al₂O₃-SiO₂ slags.
3. The dissolution rate of CA2 particles significantly decreased when the SiO₂ content increased from 10 wt.% to 40 wt.%. However, a further increase to 50 wt.% SiO₂ did not significantly influence the dissolution rate. The significant decrease in total dissolution time from the slag with 40 wt.% SiO₂ to the slag with 10 wt.% SiO₂ is primarily affected by the change in slag structure.
4. At 1550°C, the dissolution rates of CA2 and CA6 particles increased with an increase in slag C/A ratio from 0.9 to 1.8 but declined when C/A ratio further increased to 3.8, caused by the formation of an intermediate solid layer around the CA2 and CA6 particles in slag with a C/A ratio at 3.8, acting as a hindrance and impeding their dissolution at 1550°C. This layer was identified as a melilite phase, aligning well with the thermodynamic predictions, validating the accuracy of the experimental and analytical methodologies employed.
5. By combining porosity and surface area measurements made using X-ray Computed Tomographic Imaging and HT-CLM experiments, it was determined that increasing the

porosity of CA2 particles enhances dissolution kinetics, with the average dissolution rate rising from 0.35 $\mu\text{m/s}$ to 0.59 $\mu\text{m/s}$ as porosity increases from 0.08 to 0.20.

6. The modified mass transfer-controlled dissolution mode (MMDM) prediction showed that the total dissolution kinetics of CA2 particles was enhanced by an increase in φ , v , and ΔC , and a decrease in μ . The parameter sensitivity analysis found that the order of parameter influence is for $0.25 \leq X_i/X_{r(i)} \leq 2$, $\Delta C > \varphi > v > \mu$, and for $2 < X_i/X_{r(i)} \leq 4$, $\varphi > \Delta C > \mu > v$.
7. Adding MgO (from 0 to 8 wt.%) in slag enhanced the dissolution kinetics of CA2 and CA6 particles by decreasing the polymerization degree of slag. However, thermodynamic calculations predicted the formation of intermediate solid products (MA, CM2A8, CA2 and C2M2A14), which would reduce $\Delta C_{\text{Al}_2\text{O}_3}$ and hinder the dissolution.
8. Two types of intermediate solid products were observed to form during CA6 particles dissolution: 1) the products presented in a solid layer around the particle, retarding the dissolution kinetics and affecting the dissolution mechanisms; 2) the products occurred in small amounts, had a small size, and were irregularly dispersed, which did not affect, rather than hinder, the dissolution kinetics and mechanisms of CA6 particles. This morphological effect significantly influenced $\Delta C_{\text{Al}_2\text{O}_3}$ but was not fully captured in the thermodynamic modeling.
9. Two distinct dissolution behaviors for CA2 and CA6 particles in molten slag were observed:
Direct dissolution: 1) No intermediate solid products form, and the dissolution kinetics is controlled by the mass transport of species through the boundary layer. The driving force ($\Delta C_{\text{Al}_2\text{O}_3}$) is constant. 2) Irregular dispersed intermediate solid products formed during the dissolution process due to the chemical reactions between the molten slag and the particle. However, they do not have an impact on the ΔC and do not retard the dissolution kinetics of the particle.

(b) *Indirect dissolution with solid layer formation:* An intermediate solid layer forms around the particle, inhibiting the transport of species and reducing $\Delta C_{\text{Al}_2\text{O}_3}$ by altering the interface from slag – particle to slag – intermediate solid layer, significantly slowing dissolution kinetics.

6.2 Future Works

1. Further studies on industrially relevant compositions, such as $1.2 < \text{CaO}/\text{Al}_2\text{O}_3 \text{ ratio} < 1.8$, $5 \text{ wt.\%} < \text{SiO}_2 < 15 \text{ wt.\%}$, $\text{MgO} < 12 \text{ wt.\%}$, would provide deeper insights on the design or selection of optimal slag compositions during refining.
2. In this work, the modified mass transfer-controlled dissolution model (MMDM) has been developed by considering the particle's porosity and velocity based on the dissolution of CA2 particles. However, its generic framework enables the application to other types of oxides such as Al_2O_3 , MgO , $\text{MgO}\cdot\text{Al}_2\text{O}_3$, and CA_6 . In the future, this could be explored further.
3. Fluid flow (e.g., gas stirring, Marangoni flow) in industrial practice influences the velocity of the particle, while the formation and dissolution of the intermediate solid layers under indirect dissolution—both factors were not considered in the MMDM. Further model development could integrate these effects for improved accuracy and applicability.
4. More time-sequenced experiments could clarify formation sequences and evolution pathways of intermediate solid products, improving dissolution modeling and understanding their effects on dissolution kinetics and mechanisms.
5. This study has studied two CA2 particle porosity levels, showing a significant impact on the dissolution kinetics. Additional experiments with varying porosity levels would further refine the understanding of porosity effects on their dissolution behaviors.
6. Successful removal of NMIs involves flotation to the steel – slag interface, separation across this interface, and dissolution in the molten slag. Most studies account for the removal rate of NMIs only by considering the floatation to the interface and assuming the separation and dissolution occur automatically once the NMIs reach the interface. However, experiments revealed ineffective separation, with agglomerated NMIs remaining at the steel – slag interface. Therefore, developing methods to incorporate separation and dissolution into NMI removal assessments would improve accuracy.
7. While CFD models have been developed for NMI flotation and separation in the steel – slag system, limited studies focus on NMI dissolution. Developing a CFD model for the dissolution process, potentially integrating flotation and separation CFD models, would provide a comprehensive understanding of the entire NMI removal process and improve removal rate predictions.